Inscription of fiber Bragg gratings in non-photosensitive and rare-earth doped fibers applying ultrafast lasers

DISSERTATION

Zur Erlangung des akademischen Grades
doctor rerum naturalium (Dr. rer. nat.)

FRIEDRICH-SCHILLER-UNIVERSITÄT JENA

vorgelegt dem Rat der Physikalisch-Astronomischen Fakultät
der Friedrich-Schiller-Universität Jena

von M.Sc. Elodie Wikszak

geboren den 12.06.80 in Roubaix (Frankreich)

1. Gutachter: Prof. Dr. Andreas Tünnermann

2. Gutachter: Prof. Dr. Hartmut Bartelt

3. Gutachter: Prof. Michael Withford, Sydney (Australien)

Tag der letzten Rigorosumsprüfung: 12.05.2009

Tag der öffentlichen Verteidigung: 28.05.2009

Contents

1. Introduction

The last thirty years have seen the advent of the optical fiber and fiber telecommunications. The discovery of the Fiber Bragg Grating (FBG) [1], which is composed of a periodical refractive index change in the fiber core, enabled the realization of fiber integrated reflectors or transmission filters with narrow bandwidths. Thus, new applications like Wavelength Division Multiplexing (WDM) and the realization of monolithic fiber lasers was made possible. Furthermore, as the fiber grating response is dependent on strain and temperature, compact fiber sensors could be realized. Up to now, FBGs were mainly written by absorption of an UV interference pattern. A prerequisite is, however, a photosensitive fiber. The fiber photosensitivity is linked to the presence of defects increasing the UV absorption coefficient of the fiber and is typically achieved by co-doping the fiber core with germanium or other ions. Another possibility to increase the photosensitivity is to load the fiber with hydrogen. Those methods are currently used for standard telecommunication fibers but are difficult to apply to rare-earth-doped fibers. The FBGs are thus generally written into a standard photosensitive fiber and then spliced to the rare-earth-doped fiber. However, this method cannot be used for the implementation of high power fiber lasers, because additional losses are introduced in the manufacturing process, limiting the laser performance around 1 µm. Therefore, an alternative technique allowing the flexible inscription of FBGs in fibers almost independently of their chemical composition had to be developed.

In the past ten years, permanent refractive index changes have been induced inside transparent glass materials using femtosecond laser pulses. As high energy densities are required for the non-linear absorption, the energy deposition and the resulting refractive index change is localized to the focal region of the laser beam. Waveguides can be simply written by translating the glass under the laser beam. Thus, waveguides as well as three dimensional structures such as beam splitters [2] and waveguide arrays [3] could be realized in different glasses like fused silica as well as in non-linear crystals [4]. Due to its high flexibility in the choice of the transparent material, the femtosecond writing technique opens new possibilities for the realization of all-integrated and dense optical circuits including lasers, waveguides, filters as well as optical switches in a single chip.

The aim of this work is to establish the use of ultrashort laser pulses as a new flexible method for the inscription of FBGs into different non-photosensitive fibers without any pre-

or post-treatment. FBGs should be written in standard telecommunication fibers, rare-earth-doped fibers as well as polarization maintaining fibers using the same inscription technique based on the non-linear absorption of femtosecond pulses.

This thesis is divided into four chapters. The first chapter captures the fundamentals of fiber Bragg grating theory. After a short introduction to light propagation in step index fibers and to fiber gratings, the coupled-wave theory is reviewed. The parameters influencing the grating reflectivity are studied for the case of a uniform FBG using the analytical solution derived from the coupled-wave equations.

The second chapter gives some insight into the techniques used for the FBG inscription in photosensitive fibers using UV radiation as well as in non-photosensitive fibers using IR femtosecond pulses. The photosensitization techniques and the characteristics of UV written gratings are studied in detail with an emphasis on the limitations of the UV writing technique. After a short introduction to the mechanisms responsible for the non-linear absorption of femtosecond pulses and the refractive index change, the different writing techniques as well as specific issues like the focusing and the positioning of the modifications are considered. The inscription techniques are compared with respect to the required positioning accuracy and the feasibility in an industrial environment. Special focus is set on the phase mask technique which has been used within this thesis. The inscription setup as well as the equipment used are also described.

In the third chapter, the characteristics of the written FBGs are studied. The size of the modifications as well as its impact on the grating response is discussed. The influence of the writing parameters on the grating efficiency is studied by evaluating the coupling constant of the written gratings. We also demonstrate that particular grating designs can be realized by choosing properly the inscription parameters such as pulse energy, translation velocity and grating length. The thermal stability of the written FBGs is also studied.

The last chapter explores the possibilities of the femtosecond writing technique to inscribe highly reflective FBGs into rare-earth doped fibers. The FBG inscription in erbium and in ytterbium doped fibers is demonstrated as well as its application for the realization of fiber lasers using the intracore FBGs as resonator mirrors. Furthermore, the inscription of FBGs in Polarization Maintaining (PM) as well as in Large Mode Area (LMA) fibers demonstrates the flexibility of our method, which opens new opportunities for the realization of monolithic and robust high power fiber lasers.

2. Fiber gratings theory

Fiber gratings are composed of a periodical refractive index change localized in the fiber core. For small grating pitches (of the order of the light wavelength) the fiber grating behaves like a dielectric mirror and is called a Fiber Bragg Grating (FBG). Light is partially reflected at each plane of refractive index change, resulting in a strong reflection for the wavelengths interfering constructively. In that case, fiber Bragg gratings can be seen as volume gratings integrated into an optical fiber. The interaction between the guided modes and the grating can be described using the coupled-mode theory first introduced by Kogelnik, who modeled the reflection and transmission properties of thick holograms [5]. In the last fifteen years, fiber gratings have become essential compact and low-cost components extensively used in filtering, sensing and telecommunication applications.

The aim of this chapter is to introduce the fundamentals of fiber Bragg grating theory. In the first section, light guidance in an optical fiber will be described in terms of bounded modes, propagation constants and effective refractive index. In the second section, the notion of fiber gratings will be introduced with particular emphasis on fiber Bragg gratings. Using the coupled-mode analysis, an analytical expression for the FBG reflectivity for uniform grating profiles will be developed, and the parameters influencing the grating characteristics will be discussed.

2.1. Light guiding in an optical fiber

An optical fiber is a cylindrical dielectric waveguide composed of a core of refractive index $n_{\mathrm{co}}(r)$ (where light is guided) and a cladding with a lower refractive index $n_{\mathrm{cl}}(r)$. For simplification purposes, we consider here the case of a step index fiber where n_{co} and n_{cl} are constant. The fiber geometry is shown in Fig. 2.1. In order to protect the cladding from mechanical constraints, a coating of refractive index n_{coat} surrounds the cladding.

Light is guided within the fiber core due to total internal reflection at the boundary between the fiber core and the cladding. Thus, light waves having an angle θ greater than the critical angle $\theta_c = \arcsin(n_{\mathrm{cl}}/n_{\mathrm{co}})$ will be reflected and bounded to the fiber core. For angles θ smaller than θ_c, light will be refracted through the cladding.
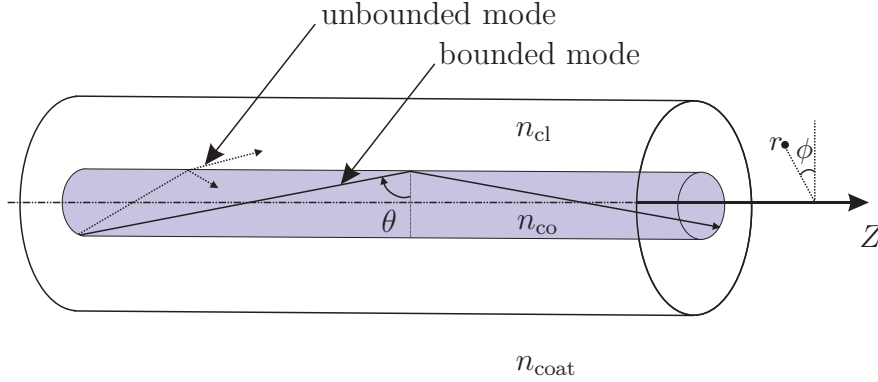
Figure 2.1: Schematic light guidance in a step index optical fiber.

2.1.1. Bounded modes

Another necessary condition for light guiding is that waves having the same angle with respect to the fiber axis must remain in phase after several reflections at the core-cladding boundary. The solutions are therefore limited to a discrete number of angles and each angle corresponds to a bounded mode which is characterized by its propagation constant along the fiber axis $\beta = \frac{2\pi}{\lambda}\, n_{\mathrm{co}} \sin\theta = \frac{2\pi}{\lambda}\, n_{\mathrm{eff}}$ (where n_{eff} is the effective refractive index of the mode.) The transverse spatial distribution of the electric field and the polarization direction are maintained during the propagation of the bounded mode.

Depending on the value of the propagation constant, different types of modes can exist:

- *the core modes* for $\frac{2\pi}{\lambda}\, n_{\mathrm{cl}} < \beta < \frac{2\pi}{\lambda}\, n_{\mathrm{co}}$: Light is guided in the core through total internal reflection at the core-cladding boundary.

- *the cladding modes* for $\frac{2\pi}{\lambda}\, n_{\mathrm{coat}} < \beta < \frac{2\pi}{\lambda}\, n_{\mathrm{cl}}$ (if $n_{\mathrm{coat}} < n_{\mathrm{cl}}$) : Light is guided in the cladding due to total internal reflection at the cladding-coating boundary. As the density of the cladding modes is much higher than the core modes, they almost form a continuum of modes.

- *the continuum of radiation modes* for $\beta < \frac{2\pi}{\lambda}\, n_{\mathrm{coat}}$: Light is not guided and radiates out of the fiber.

2.1.2. Analytical expressions of the core bounded modes

Considering the propagation of monochromatic light in a step-index fiber, we will derive the expressions of the electric field satisfying Maxwell's equations and the boundary conditions imposed by the cylindrical dielectric core and cladding as described in [6].

Considering a linear, non-dispersive, homogeneous and isotropic medium in the absence of free electric charges or current, Maxwell's equations for the electric field $\mathcal{E}$ and the magnetic field $\mathcal{H}$ reduce to

$$\nabla \times \mathcal{H} = \epsilon \frac{\partial \mathcal{E}}{\partial t} \tag{2.1a}$$

$$\nabla \times \mathcal{E} = -\mu_0 \frac{\partial \mathcal{H}}{\partial t} \tag{2.1b}$$

$$\nabla \cdot \mathcal{E} = 0 \tag{2.1c}$$

$$\nabla \cdot \mathcal{H} = 0, \tag{2.1d}$$

where ϵ is the electric permittivity and μ_0 the magnetic permeability for a non-magnetic medium. These constants define the response of the medium to the external electric and magnetic fields, respectively. Using the nabla operator ∇, $\nabla \times$ stands for the curl operator and $\nabla \cdot$ for the divergence operator. In a simplified manner, the electric and magnetic fields propagating in the medium must satisfy the wave equation

$$\nabla^2 \mathcal{U} - \frac{1}{c^2} \frac{\partial^2 \mathcal{U}}{\partial t^2} = 0, \tag{2.2}$$

where $c^2 = 1/(\epsilon \mu_0)^2$ is the velocity in the medium; $\mathcal{U}$ represents either the electric field $\mathcal{E}$ or the magnetic field $\mathcal{H}$. This equation is obtained from Eq. (2.1b) using the vector identity $\nabla \times (\nabla \times \mathcal{E}) = \nabla(\nabla \cdot \mathcal{E}) - \nabla^2 \mathcal{E}$ and the other Maxwell's equations.

Considering monochromatic electromagnetic waves, the time dependence of the electromagnetic field is described by e^{jwt}, with the angular frequency $w = 2\pi f$. Eq. (2.2) simplifies to the Helmholtz equation as follows:

$$\nabla^2 \mathbf{U} - n^2 k_0^2 \mathbf{U} = 0, \tag{2.3}$$

$\mathbf{U}$ being the complex amplitude of the electric or magnetic field, k_0 the propagation constant in vacuum defined by $k_0 = w/c_0 = 2\pi/\lambda$ and n the refractive index defined by $n = c_0/c$. This equation must be satisfied by each component of the electric and magnetic field vectors.

Spatial distribution

The spatial distribution of the core bounded modes is determined by solving the Helmholtz equation (2.3) in the core ($r < a$) for $n = n_{\mathrm{co}}$ and in the cladding ($r > a$) for $n = n_{\mathrm{cl}}$. We consider now only the axial components of the electric and magnetic fields E_Z and H_Z in the cylindrical coordinate system as defined in Fig. 2.1. The transversal components of

the electric field, E_R and E_Φ, and of the magnetic field, H_R and H_Φ, can then be easily deduced from E_Z and H_Z using Maxwell's equations. Considering that the core bounded modes are mainly localized within the fiber core, the cladding can be considered infinite in a first approximation. Thus, the Helmholtz equation in the cylindrical coordinate system reads as

$$\frac{\partial^2 U}{\partial r^2} + \frac{1}{r}\frac{\partial U}{\partial r} + \frac{1}{r^2}\frac{\partial^2 U}{\partial \phi^2} + \frac{\partial^2 U}{\partial z^2} + n^2 k_0^2 U = 0, \tag{2.4}$$

where $U = U(r, \phi, z)$ is the complex amplitude of the axial components of the electric field E_Z or magnetic field H_Z.

The solutions are bounded waves propagating in the z direction with a propagation constant β. Since U must be a periodic function of the angle ϕ with a period of 2π, we assume that the dependence on ϕ is harmonic giving $e^{-il\phi}$, where $l \in \mathbb{Z}$. Thus, the solutions are of the form

$$U(r, \phi, z) = \Re(u(r)\ e^{-il\phi}\ e^{-i\beta z}), \quad l \in \mathbb{Z}. \tag{2.5}$$

For simplification purposes, only the complex amplitude will be considered in the following. By substituting Eq. (2.5) into Eq. (2.4), we get

$$\frac{\partial^2 u}{\partial r^2} + \frac{1}{r}\frac{\partial u}{\partial r} + \left(n^2 k_0^2 - \beta^2 - \frac{l^2}{r^2}\right) u = 0. \tag{2.6}$$

which is the differential equation for Bessel functions.

As the propagation constant for core-bounded modes fulfills $n_{cl}k_0 < \beta < n_{co}k_0$,

$$k_T^2 = n_{co}^2 k_0^2 - \beta^2 \tag{2.7a}$$

and

$$\gamma^2 = \beta^2 - n_{cl}^2 k_0^2 \tag{2.7b}$$

are positive, which allows us to define the real transverse wavenumber k_T and the decay parameter γ.

Equation (2.6) can then be written separately for the cladding and for the core as

$$\frac{\partial^2 u}{\partial r^2} + \frac{1}{r}\frac{\partial u}{\partial r} + (k_T^2 - \frac{l^2}{r^2})\, u = 0, \qquad r < a \text{ (core)}, \tag{2.8a}$$

$$\frac{\partial^2 u}{\partial r^2} + \frac{1}{r}\frac{\partial u}{\partial r} - (\gamma^2 + \frac{l^2}{r^2})\, u = 0, \qquad r > a \text{ (cladding)}, \tag{2.8b}$$

and can be solved using the Bessel functions. The solutions are a combination of the first and second order Bessel functions $J_l(k_T r)$ and $Y_l(k_T r)$ in the core, and of the modified Bessel

functions of first and second order $I_l(\gamma r)$ and $K_l(\gamma r)$ in the cladding. The variable l defines the order of the Bessel function. As the energy density is limited for a physical system, we have to exclude functions that approach infinity at $r \to 0$ in the core or at $r \to \infty$ in the cladding. The expression of the core bounded modes becomes

$$u(r) \propto \begin{cases} J_l(k_T r), & r < a \text{ (core)}, \\ K_l(\gamma r), & r > a \text{ (cladding)}. \end{cases} \tag{2.9}$$

The function $J_l(x)$ oscillates like sine or cosine functions but with a decaying amplitude. For $x \gg 1$, $K_l(x)$ decays with increasing r at an exponential rate.

Using the continuity of the tangential components of the electric and magnetic fields at $r = a$ allows us to find the values of the proportionality constants in Eq. (2.9) for E_Z and H_Z. E_Φ and H_Φ can be determined in function of E_Z and H_Z using Maxwell's equations. The first continuity condition at $r = a$ applied on E_Z and H_Z yields a relation between the proportionality constants of Eq. (2.9). The continuity condition on E_Φ and H_Φ provides two more equations. One equation relates the two unknown coefficients of proportionality in E_Z and H_Z. The other gives an equation that the propagation constant β must satisfy.

Dispersion relation for a weakly guiding fiber

Usually, optical fibers are weakly guiding ($n_{\text{co}} - n_{\text{cl}} \ll 1$). Thus, the longitudinal components of the electric and magnetic fields can be neglected and only the transversal components are taken into account. The bounded modes are then composed of two sets of orthogonally polarized modes called Linearly Polarized (LP) modes. For each allowed propagation constant β, two orthogonally polarized modes with identical spatial field distributions exist. One of the continuity conditions on E_Φ or H_Φ at $r = a$ leads to a characteristic equation, known as the dispersion relation, that the propagation constant β must satisfy. Using the normalized parameters $X = k_T a$ and $Y = \gamma a$, this characteristic equation can be written as

$$X \frac{J_{l\pm1}(X)}{J_l(X)} = \pm Y \frac{K_{l\pm1}(Y)}{K_l(Y)}. \tag{2.10}$$

Using $X^2 + Y^2 = 2\left(n_{\text{co}}^2 - n_{\text{cl}}^2\right) a^2 k_0^2$, the dispersion relation (Eq. (2.10)) can be written as a function of X and can be solved numerically considering the intersection of the functions on the left- and right-hand sides of Eq. (2.10). For a given value of l, different values of X corresponding to the LP_{lm} modes can be found. The corresponding transverse propagation constant k_{Tlm} is determined using $X = k_T a$. Using Eq. (2.7) and Eq. (2.9) allows us to

determine the decay parameter γ_{lm}, the propagation constant β_{lm} and the radial distribution function $u_{lm}(r)$. Thus, the expression of the LP_{lm} modes becomes

$$LP_{lm} = \begin{cases} u_{lm}(r) \; e^{-il\phi} \; e^{-i\beta_{lm}z}, & \text{in cylindrical coordinates} \\ \mathbf{e}_{lm}^{\mathrm{T}}(x,y) \; e^{-i\beta_{lm}z}, & \text{in cartesian coordinates.} \end{cases} \quad (2.11)$$

For a more detailed description of the LP modes please refer to [7, 8].

In this section we described the propagation of bounded modes and defined their propagation constant as well as their effective refractive index. These notions will be used in the next section for the description of the mode coupling in fiber gratings.

2.2. Fiber gratings

Fiber gratings consist of a periodical refractive index inscribed into the fiber core. The periodical perturbation of the effective refractive index allows the coupling of a core mode into forward- or backward- propagating modes, depending on the grating period.

2.2.1. Long-period and short-period gratings

The nature of the mode coupling depends on the period of the grating. It can be quite well understood using a ray optical approach [9]. Let us consider the grating as a typical diffraction grating of period Λ. A light wave incident on the grating with an angle θ_1 will be diffracted out of the grating with an angle θ_2 according to the grating equation [10]

$$n \sin \theta_2 = n \sin \theta_1 + m \frac{\lambda}{\Lambda}, \quad (2.12)$$

m being the diffraction order of the grating. For fiber gratings, the diffraction is predominant in the -1st order (as this is usually the case for standard volume gratings).

Considering now that the incident and refracted rays correspond to the bounded modes of the optical fiber, the propagation constant β can be defined as $\beta = 2\pi \, n_{\mathrm{eff}}/\lambda$ with $n_{\mathrm{eff}} = n_{\mathrm{co}} \sin \theta$. Thus Eq. (2.12) can be rewritten for bounded modes as

$$\beta_2 = \beta_1 - \frac{2\pi}{\Lambda}. \quad (2.13)$$

This equation allows us to predict for which period the coupling between two modes with the propagation constants β_1 and β_2 occurs at the wavelength λ.

The fiber gratings are classified into two categories depending on the type of mode coupling:

- *Bragg gratings* - also called reflection or short period gratings - where the coupling takes place between two modes traveling in opposite directions.

- *Long period gratings* - also called transmission gratings - where the coupling takes place between a core and a cladding mode traveling in the same direction.

Bragg gratings are usually used, for example, as narrow bandwidth filters in transmission for telecommunication applications or as narrow bandwidth reflectors in fiber laser cavities. Long period gratings can be used to filter out a particular mode at a given wavelength. Furthermore, both grating types are also currently used as high sensibility strain or temperature sensors, since the grating period (i.e. response) is sensitive to small changes in temperature or tension.

Bragg gratings

Fig. 2.2 illustrates the coupling between a forward- and a backward- propagating mode. The incoming beam arrives on the grating with an angle θ_1 and is diffracted into the -1st diffraction order with a negative angle θ_2. As θ_2 is bigger than the critical angle for total reflection at the core-cladding boundary θ_c the light is still guided along the fiber core. Using Eq. (2.13) with the corresponding propagation constants β_1 and $\beta_2 < 0$, the reflected wavelength is

$$\lambda = \left(n_{\text{eff}_1} + n_{\text{eff}_2} \right) \Lambda \tag{2.14}$$

where n_{eff_1} and n_{eff_2} are the effective indices of both modes. Considering the coupling between two identical modes ($n_{\text{eff}_2} = n_{\text{eff}_1}$), one arrives at the well-known Bragg reflection condition

$$\lambda_B = 2 \, n_{\text{eff}} \, \Lambda. \tag{2.15}$$

The coupling of the core mode into its identical counter-propagating mode is the dominant interaction considered in a Bragg grating.

Long period gratings

We consider now the coupling between two bounded waves traveling in the same direction. Figure 2.3 shows the coupling between a core mode and a cladding mode. This time, the incoming beam is diffracted into a smaller positive angle θ_2. As θ_2 is smaller than θ_c, light
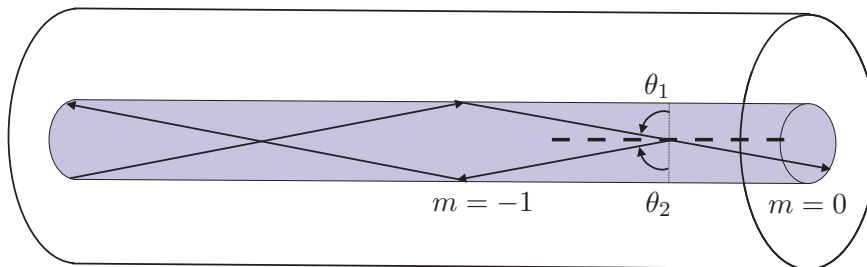
Figure 2.2: Ray optical illustration of core-mode reflection by a short period grating (from [9], modified).
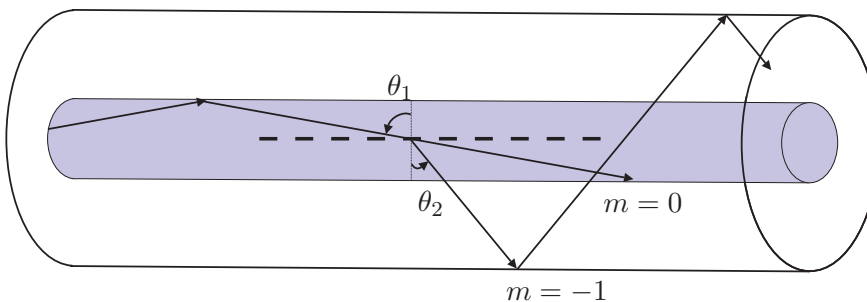
Figure 2.3: Ray optical illustration of the coupling between a core mode and a cladding mode by a long period grating (from [9], modified).

radiates out of the core and can be guided into the cladding if $\frac{2\pi}{\lambda} n_{\text{coat}} < \beta_2 < \frac{2\pi}{\lambda} n_{\text{cl}}$. Using Eq. (2.13) for $\beta_2 > 0$ the wavelength of the resonance is

$$\lambda_{LPG} = \left(n_{\text{eff}_1} - n_{\text{eff}_2} \right) \Lambda. \tag{2.16}$$

Thus, for co-propagating coupling at a given wavelength, a much longer grating period ($\Lambda > 100$ µm) is required than for counter-propagating coupling (Eq. (2.14)).

2.2.2. Coupled-mode theory

The coupled-mode formalism can provide analytical solutions for uniform sinusoidal periodic perturbations such as, for example, a refractive index change. In our case, it is an effective method to gain quantitative information about the coupling efficiency and the spectral dependence of the gratings. It will furthermore help to define and understand important parameters like phase matching and overlap integral, which will be introduced in the following section. However, for more complex grating shapes, numerical methods must be applied to evaluate the reflectivity of the inscribed gratings.

Coupled-mode equations

The waveguide modes satisfy the wave equation derived from Maxwell's equations (2.1). Using the electric flux density $\mathcal{D} = \epsilon \mathcal{E} = \epsilon_0 \mathcal{E} + \mathcal{P}$, the wave equation (2.2) becomes:

$$\nabla^2 \mathbf{E} = \mu_0 \varepsilon_0 \frac{\partial^2 \mathbf{E}}{\partial t^2} + \mu_0 \frac{\partial^2 \boldsymbol{P}}{\partial t^2}, \tag{2.17}$$

where ε_0 is the dielectric constant, $\mathbf{E}$ the vector of the applied electric field and $\mathbf{P}$ the vector of the induced polarization.

Assuming that wave propagation takes place in a system perturbed by a dielectric grating, the total polarization can be separated into two terms, unperturbed and perturbed polarization, as

$$\mathbf{P} = \mathbf{P}_{\text{unpert}} + \mathbf{P}_{\text{grating}}, \tag{2.18}$$

where

$$\mathbf{P}_{\text{unpert}} = \varepsilon_0 [\varepsilon_r - 1] \mathbf{E}. \tag{2.19}$$

Equation (2.17) becomes

$$\nabla^2 \mathbf{E} = \mu_0 \varepsilon_0 \varepsilon_r \frac{\partial^2}{\partial t^2} \mathbf{E} + \mu_0 \frac{\partial^2}{\partial t^2} \mathbf{P}_{\text{grating}}. \tag{2.20}$$

In the generalized coupled-mode wave formalism, the electric field propagating along the fiber is described as a summation of l transverse guided modes (core modes as well as cladding modes). In the following, we consider only the interaction between the core modes. We thus decompose the electric field as a sum of transversely linearly polarized modes

$$E_t = \Re\left(\sum_{\mu=0}^{\mu=l} A_\mu(z) \ \mathbf{e}_\mu^{\text{T}}(x, y) \ e^{i(\omega t - \beta_\mu z)} \right), \tag{2.21}$$

where $A_\mu(z)$ is the amplitude of the mode propagating with the propagation constant β_μ and the radial transverse field distributions $\mathbf{e}_\mu^{\text{T}}(x, y)$ of the linearly polarized modes as defined in Eq. (2.11). They correspond to the x or y components of the electric and magnetic fields and can be deduced from the expressions of the bounded core modes developed in Sec. 2.1. In the following, the exponential definition of the electric field, also known as complex amplitude, will be used to simplify the calculations. By inserting Eq. (2.21) into Eq. (2.20) and applying

the slowly varying envelope approximation for the case of weak coupling

$$\left| \frac{\partial^2 A_\mu}{\partial z^2} \right| << \left| \beta_\mu \frac{\partial A_\mu}{\partial z} \right| , \tag{2.22}$$

the wave equation simplifies to

$$\sum_{\mu=1}^{\mu=l} \left[-2i\beta_\mu \frac{\partial A_\mu}{\partial z} \mathbf{e}_\mu^{\mathrm{T}}(x,y) \, e^{i(\omega t - \beta_\mu z)} + cc \right] = \mu_0 \frac{\partial^2}{\partial t^2} P_{\mathrm{grating}} , \tag{2.23}$$

using $\omega^2 \mu_0 \varepsilon_0 \varepsilon_r = \beta_\mu{}^2$ and remembering that $\mathbf{e}_\mu^{\mathrm{T}}(x,y) \, e^{i(\omega t - \beta_\mu z)}$ is a solution of the wave equation Eq. (2.17) in absence of the perturbation. Multiplying both sides of Eq. (2.23) by the complex conjugate of the transverse field distribution $\mathbf{e}_\mu^{\mathrm{T}}(x,y)^*$ and integrating over the entire cross-section leads to

$$\sum_{\mu=1}^{\mu=l} \int\!\!\!\int_{-\infty}^{+\infty} -2i\beta_\mu \frac{\partial A_\mu}{\partial z} \mathbf{e}_\mu^{\mathrm{T}}(x,y) \, \mathbf{e}_\mu^{\mathrm{T}}(x,y)^* \, e^{i(\omega t - \beta_\mu z)} \, dx \, dy =$$

$$\int\!\!\!\int_{-\infty}^{+\infty} \mu_0 \frac{\partial^2}{\partial t^2} P_{\mathrm{grating}} \mathbf{e}_\mu^{\mathrm{T}}(x,y)^* \, dx \, dy. \tag{2.24}$$

At this point, it is important to note that the perturbation induced by the grating also has a transverse profile which depends on the inscription conditions and must be taken into account for the integration over the cross section. Applying the orthogonality relation and ensuring that the power carried in the μth mode is $|A_\mu|^2 = 1$ [11]

$$1/2 \left[\frac{\beta_\mu}{\omega\mu_0} \right] \int\!\!\!\int_{-\infty}^{+\infty} \mathbf{e}_\mu^{\mathrm{T}}(x,y) \cdot \mathbf{e}_\nu^{\mathrm{T}}(x,y)^* \, dx \, dy = \delta_{\mu\nu} \tag{2.25}$$

results in

$$\sum_{\mu=1}^{\mu=l} -4i\omega\mu_0 \frac{\partial A_\mu}{\partial z} \, e^{i(\omega t - \beta_\mu z)} =$$

$$\int\!\!\!\int_{-\infty}^{+\infty} \mu_0 \frac{\partial^2}{\partial t^2} P_{\mathrm{grating}} \mathbf{e}_\mu^{\mathrm{T}}(x,y)^* \, dx \, dy. \tag{2.26}$$

Equation (2.26) is a fundamental equation describing the exchange of power between different orthogonal guided modes.

Counterpropagating modes

Considering only the mode coupling between two different forward- and backward-propagating modes denoted by the indices ν and μ and replacing Eq. (2.21) by

$$E_t = A_\nu(z)\, \mathbf{e}_\nu^{\mathrm{T}}(x,y)\, e^{i(\omega t - \beta_\nu z)} + B_\mu(z)\, \mathbf{e}_\mu^{\mathrm{T}}(x,y)\, e^{i(\omega t + \beta_\mu z)}, \qquad (2.27)$$

in Eq. (2.23) and after simplifications (see [11]), we finally obtain:

$$\frac{\partial A_\nu}{\partial z}\, e^{i(\omega t - \beta_\nu z)}\delta_{k\nu} - \frac{\partial B_\mu}{\partial z}\, e^{i(\omega t + \beta_\mu z)}\delta_{k\mu} =$$
$$+\frac{i}{4\omega} \int\!\!\!\int\limits_{-\infty}^{+\infty} \frac{\partial^2}{\partial t^2} P_{\mathrm{grating}}\, \mathbf{e}_k^{\mathrm{T}}(x,y)^*\, dx\; dy, \qquad (2.28)$$

with $\mathbf{e}_k^{\mathrm{T}}(x,y)^*$ being the conjugate of the transverse electric field of the mode under consideration with $k = \mu$ or ν. This expression defines the possible interaction between a forward- and a backward-propagating mode due to the polarization perturbation caused by the grating. In the next paragraph, we will describe how the refractive index modification induced by the grating can cause that polarization perturbation.

Spatially periodic refractive index modulation

Let us consider now a grating inscribed into the fiber core. It can be considered as a perturbation $\Delta n(z)$ of the refractive index in the fiber core n. In the most general case we consider an arbitrary periodic refractive index profile described by

$$\Delta n(z) = \Delta n_0 +\; \Delta n_1 \cos\left(\frac{2\pi z}{\Lambda} + \Phi(z)\right) +\; \Delta n_2 \cos\left(\frac{4\pi z}{\Lambda} + \Phi(z)\right)$$
$$+\cdots+\; \Delta n_m \cos\left(\frac{2m\pi z}{\Lambda} + \Phi(z)\right), \qquad (2.29)$$

which is the expansion of the refractive index profile into a Fourier series. Δn_0 is the average index modulation of the grating within the fiber core responsible for a change of the effective refractive indices of the propagating modes. Δn_1 is the amplitude of the cosine function having the period Λ used for the inscription of the grating. Usually only those two leading terms are considered for the description of a fiber grating. However, further terms can appear if the grating profile has sharper edges due to the saturation of the refractive index modulation during the inscription process [12]. These additional terms lead to higher diffraction orders

m having an effective period Λ/m and a contribution proportional to Δn_m. $\Phi(z)$ describes a change in the grating phase along the grating length. A change of the grating period along z, also known as chirp, can be represented this way.

Perturbed polarization

As the refractive index n can be defined with the relative permittivity ε_r as $n^2 = \varepsilon_r$, we get a modification of the relative permittivity $\Delta\varepsilon(z)$ defined by

$$[n + \Delta n(z)]^2 = \varepsilon_r + \Delta\varepsilon(z), \tag{2.30}$$

taking into account the modification of the refractive index $\Delta n(z)$. Considering the perturbation $\Delta n(z)$ as small compared to the refractive index, we have

$$\Delta\varepsilon(z) \approx 2n\Delta n(z). \tag{2.31}$$

This leads to the expression of the total permittivity

$$\mathbf{P} = \varepsilon_0[\epsilon_r + \Delta\epsilon - 1]\mathbf{E}. \tag{2.32}$$

Combining Eq. (2.32) with Eq. (2.18) and Eq. (2.19), the expression of the polarization induced by the grating $\mathbf{P}_{\mathrm{grating}}$ is

$$\mathbf{P}_{\mathrm{grating}} = \varepsilon_0 \Delta\varepsilon(z)\mathbf{E}. \tag{2.33}$$

Using Eq. (2.31) in Eq. (2.33), the expression of the perturbed polarization as a function of the refractive index modulation of the grating becomes

$$P_{\mathrm{grating}} = 2n\varepsilon_0\Delta n(z)E_t. \tag{2.34}$$

We rewrite now the refractive index modulation of Eq. (2.29) in its complex form and, for simplification purposes, only consider the complex amplitude of the mth diffraction order having an effective period Λ/m and the average refractive index change Δn_0:

$$\Delta n(z) = \Delta n_0 + \Delta n_m \, e^{i[(2\pi m/\Lambda)z \, + \, \Phi(z)]}. \tag{2.35}$$

Inserting Eq. (2.34) and Eq. (2.35) into Eq. (2.28) leads to

$$\frac{\partial A_\nu}{\partial z} \, e^{i(\omega t - \beta_\nu z)} \delta_{k\nu} - \frac{\partial B_\mu}{\partial z} \, e^{i(\omega t + \beta_\mu z)} \delta_{k\mu}$$

$$= + \frac{i\varepsilon_0}{4\omega} \int\!\!\!\int\limits_{-\infty}^{+\infty} \frac{\partial^2}{\partial t^2} \, \Delta n(z) \, [A_\nu e^{i(\omega t - \beta_\nu z)} \mathbf{e}_\nu^{\mathrm{T}}(x,y) + B_\mu e^{i(\omega t + \beta_\mu z)} \mathbf{e}_\mu^{\mathrm{T}}(x,y)] \, \mathbf{e}_k^{\mathrm{T}}(x,y)^* \, dx \, dy$$

$$= - \frac{in\omega\varepsilon_0}{2} A_\nu \int\!\!\!\int\limits_{-\infty}^{+\infty} \Big[\, \Delta n_0 + \Delta n_m \, e^{i[(2\pi m/\Lambda)z \, + \, \Phi(z)]} \Big] \mathbf{e}_\nu^{\mathrm{T}}(x,y) \, e^{i(\omega t - \beta_\nu z)} \mathbf{e}_k^{\mathrm{T}}(x,y)^* \, dx \, dy$$

$$- \frac{in\omega\varepsilon_0}{2} B_\mu \int\!\!\!\int\limits_{-\infty}^{+\infty} \Big[\, \Delta n_0 + \Delta n_m \, e^{i[(2\pi m/\Lambda)z \, + \, \Phi(z)]} \Big] \mathbf{e}_\mu^{\mathrm{T}}(x,y) \, e^{i(\omega t + \beta_\mu z)} \mathbf{e}_k^{\mathrm{T}}(x,y)^* \, dx \, dy.$$

$$(2.36)$$

Now, we split this equation into two equations describing the energy exchange for each mode. On the left hand side, we choose the mode whose energy exchange will be described, called generated wave, for example the mode defined by the index $k = \nu$. Due to the orthogonality condition (see Eq. (2.25)), the term related to the mode μ disappears of the left hand side. On the right hand side, the first exponent must have the same phase term as on the left hand side $e^{i(\omega t - \beta_\nu z)}$ and is proportional to the average refractive index change Δn_0. The reason is that any other phase-velocity dependence like $e^{i[(2\pi m/\Lambda)z \, + \, \Phi(z)]} \, e^{i(\omega t - \beta_\nu z)}$ or $e^{i(\omega t + \beta_\mu z)}$ will not remain in phase with the generated wave. The second exponent is composed of the periodical phase from the refractive index change and of the propagation constant of the other mode $e^{i[(2\pi m/\Lambda)z \, + \, \Phi(z)]} \, e^{i(\omega t + \beta_\mu z)}$, called polarization wave, resulting from the interaction of the refractive index change and the interacting mode with the propagation constant β_μ.

Treating the mode defined by the index μ similarly, we obtain the following coupled equations, which each mode should satisfy:

$$\frac{\partial B_\mu}{\partial z} e^{i(\omega t + \beta_\mu z)} = \frac{in\omega\varepsilon_0}{2} B_\mu e^{i(\omega t + \beta_\mu z)} \iint\limits_{-\infty}^{+\infty} \Delta n_0 \, \mathbf{e}_\mu^{\mathrm{T}}(x,y) \, \mathbf{e}_\mu^{\mathrm{T}}(x,y)^* \, dx \, dy$$

$$+ \frac{in\omega\varepsilon_0}{2} A_\nu \, e^{i([(2\pi m/\Lambda) - \beta_\nu]z \, + \, \Phi(z))} \iint\limits_{-\infty}^{+\infty} \Delta n_m \, \mathbf{e}_\nu^{\mathrm{T}}(x,y) \, \mathbf{e}_\mu^{\mathrm{T}}(x,y)^* \, dx \, dy$$

$$(2.37)$$

$$\frac{\partial A_\nu}{\partial z} e^{i(\omega t - \beta_\nu z)} = -\frac{in\omega\varepsilon_0}{2} A_\nu \, e^{i(\omega t - \beta_\nu z)} \iint\limits_{-\infty}^{+\infty} \Delta n_0 \, \mathbf{e}_\nu^{\mathrm{T}}(x,y) \, \mathbf{e}_\nu^{\mathrm{T}}(x,y)^* \, dx \, dy$$

$$- \frac{in\omega\varepsilon_0}{2} B_\mu \, e^{i([(2\pi m/\Lambda) + \beta_\mu]z \, + \, \Phi(z))} \iint\limits_{-\infty}^{+\infty} \Delta n_m \, \mathbf{e}_\mu^{\mathrm{T}}(x,y) \, \mathbf{e}_\nu^{\mathrm{T}}(x,y)^* \, dx \, dy.$$

$$(2.38)$$

Two important conditions must be met to allow an efficient energy exchange between the two considered modes: phase matching and a non-zero overlap integral.

Phase matching condition

As the amplitude of the second mode is a part of the second term, an efficient energy exchange between the two modes is possible if

$$2\pi m/\Lambda + \beta_\mu = -\beta_\nu, \tag{2.39}$$

which is the *phase matching condition* already mentioned in Sec. 2.2.1 Eq. (2.13) for $\beta_1 = \beta_\nu$ and $\beta_2 = -\beta_\mu$, β_μ and β_ν being positive. Here we considered the mth diffraction order with the effective period Λ/m, m being positive.

This condition allows the continuous transfer of energy between the generated wave on the left hand side and the polarization wave on the right hand side. Finally, the frequency ω of the generated wave must remain unchanged in order to fulfill energy conservation. This gives a relation for the wavelength λ_B verifying the phase matching condition

$$\lambda_B = (n_{\mathrm{eff}_\mu} + n_{\mathrm{eff}_\nu})\Lambda/m. \tag{2.40}$$

Overlap integral

The efficiency of the energy exchange is also governed by the overlap integral between the profile of the refractive index modulation $\Delta n(z)$ and both interacting modes denoted by μ and ν defined by

$$\iint\limits_{-\infty}^{+\infty} \Delta n(z) \, \mathbf{e}_\nu^{\mathrm{T}}(x,y) \, \mathbf{e}_\mu^{\mathrm{T}}(x,y)^* \, dx \, dy, \tag{2.41}$$

where $\mathbf{e}_\nu^{\mathrm{T}}(x,y)$ and $\mathbf{e}_\mu^{\mathrm{T}}(x,y)$ are the transverse mode field distributions of the considered modes ν and μ.

In absence of perturbation, an energy exchange between two modes is impossible as both modes are orthogonal. For two different modes, due to the orthogonality relation, a non-constant periodic perturbation along the fiber cross section is necessary to get a non-null overlap integral. Whereas for two similar modes propagating in two opposite directions, as the transverse electric fields are identical, the overlap integral will have a non zero value even if the periodical refractive index change is uniform across the fiber cross section.

Generalized coupled-mode equations

In order to consider the energy exchange when the phase matching condition is not fulfilled, we introduce the phase mismatch parameter $\Delta\beta = \beta_\mu + \beta_\nu - 2\pi m/\Lambda$. The coupled-mode equations can then be rewritten as

$$\frac{\partial B_\mu}{\partial z} = i\kappa_{dc}B_\mu + i\kappa_{ac}A_\nu e^{-i[\Delta\beta z - \Phi(z)]} \tag{2.42}$$

$$\frac{\partial A_\nu}{\partial z} = -i\kappa_{dc}A_\nu - i\kappa_{ac}^*B_\mu e^{i[\Delta\beta z - \Phi(z)]}, \tag{2.43}$$

where κ_{ac} is the ac coupling constant defined as

$$\kappa_{ac} = n\omega\epsilon_0/2 \iint\limits_{-\infty}^{+\infty} \Delta n_m \, \mathbf{e}_\nu^{\mathrm{T}}(x,y) \, \mathbf{e}_\mu^{\mathrm{T}}(x,y)^* \, dx \, dy \tag{2.44}$$

and κ_{dc} is the dc coupling constant defined as

$$\kappa_{dc} = n\omega\epsilon_0/2 \iint\limits_{-\infty}^{+\infty} \Delta n_0 \, \mathbf{e}_\mu^{\mathrm{T}}(x,y) \, \mathbf{e}_\mu^{\mathrm{T}}(x,y)^* \, dx \, dy. \tag{2.45}$$

κ_{ac} and κ_{dc} are composed of the overlap integral of the ac and dc components of the refractive index change with the considered modes. κ_{dc} describes the influence of the change in the average refractive index on the propagation of the mode and κ_{ac} describes the efficiency of the mode coupling, which depends directly on the value of the refractive index modulation.

2.3. Uniform FBGs

In this section, we use the previously derived coupled-mode equations to obtain an analytical expression for the reflectivity of uniform Bragg gratings, whose refractive index profile is invariant along the fiber axis. To simplify the analytical expressions and for a better physical understanding of the influence of the different parameters, we consider the refractive index change as homogeneously distributed over the whole fiber core as is the case for conventional UV written gratings (see Sec. 3.1.1). However, for femtosecond written gratings, the size of the modifications is mainly defined by the focusing conditions (see Sec. 3.2.3). For that reason, the overlap of the modifications with the interacting modes must be taken into account for the calculation of the coupling constants. Thus, effective values for the refractive index change over the whole fiber core will be considered in order to allow for a comparison with the refractive index changes induced by standard UV absorption.

2.3.1. Coupled-mode equations

We use the coupled-mode equations (2.37) from Sec. 2.2.2 to model the energy exchange between a forward- and an identical backward-propagating (reflected) mode. In most cases, the LP_{01} fundamental core mode is considered, as single mode fibers are used preferentially in telecommunication systems and fiber laser applications. So we now consider the forward- and backward-propagating modes, respectively defined as

$$A(z) \; \mathbf{e}^{\mathrm{T}}(x,y) \; e^{i(wt-\beta z)}, \quad B(z) \; \mathbf{e}^{\mathrm{T}}(x,y) \; e^{i(wt+\beta z)} \tag{2.46}$$

with $A(z)$ and $B(z)$ being the amplitudes of the modes, $\mathbf{e}^{\mathrm{T}}(x,y)$ the transverse electric field of the mode and β the propagation constant of the LP_{01} fundamental core mode.

Inserting Eq. (2.46) into Eq. (2.37), the coupled-mode equations become:

$$\frac{dR}{dz} = -i\delta R(z) - i\kappa_{ac}^* S(z) \qquad (2.47a)$$

$$\frac{dS}{dz} = i\delta S(z) + i\kappa_{ac} R(z) \qquad (2.47b)$$

with $R(z) = A(z)\, e^{-i/2[\Delta\beta z - \Phi(z)]}$ and $S(z) = B(z)\, e^{i/2[\Delta\beta z - \Phi(z)]}$.

The general dc self coupling coefficient is defined as

$$\delta = \kappa_{dc} + 1/2\left(\Delta\beta - \frac{d\Phi(z)}{dz}\right). \qquad (2.48)$$

κ_{dc} influences the propagation of the mode due to the induced change in the effective index. The detuning parameter $\Delta\beta/2 = \beta - \pi m/\Lambda$ indicates how rapidly the power is exchanged between the generated field and the polarization field. Finally, the rate of change of $\Phi(z)$ signifies a chirp in the period of the grating and has an effect similar to that of the detuning. κ_{ac} defines the efficiency of the energy exchange between the two modes under consideration.

The profile of the refractive index change is further taken as defined in Eq. (2.35) and is composed of an average refractive index change Δn_0 and a modulation of the refractive index change Δn_m for the grating with a period Λ used in its mth diffraction order. The design Bragg wavelength is thus given by $\lambda_B = 2n_{\text{eff}}\Lambda/m$.

Considering the refractive index change as homogeneously distributed over the whole fiber core, the expressions of κ_{ac} and κ_{dc} from Eq. (2.44) and Eq. (2.45) simplify to [9]:

$$\kappa_{ac} = \frac{\pi}{\lambda}\,(\Delta n_m)_{\text{eff}} \qquad (2.49)$$

and

$$\kappa_{dc} = \frac{2\pi}{\lambda}\,(\Delta n_0)_{\text{eff}}, \qquad (2.50)$$

where $(\Delta n_m)_{\text{eff}}$ and $(\Delta n_0)_{\text{eff}}$ are the average and modulated changes in the effective refractive index. These effective refractive index changes are obtained from the calculation of the overlap integrals (Eq. (2.41)) of the locally induced refractive index changes Δn_m and Δn_0.

2.3.2. Diffraction efficiency and reflectivity

The coupled-mode equations (2.47) can be solved using standard techniques [13]. The boundary conditions are the following: at the entrance of the grating (of length L), the amplitude of the incident radiation at $z = 0$ is $R(0) = 1$; at the end of the grating ($z = L$), the

amplitude of the reflected wave is $S(L) = 0$, meaning that no light can be reflected after the end of the grating.

The amplitude reflection coefficient is defined as the quotient of the amplitude of the reflected light at the entrance of the grating and the initial amplitude of the reference [11]:

$$\rho = \frac{S(0)}{R(0)} = \frac{-\kappa_{ac} \ \sinh(\sqrt{|\kappa_{ac}|^2 - \delta^2} \ L)}{\delta \ \sinh(\sqrt{|\kappa_{ac}|^2 - \delta^2} \ L)) - i \ \sqrt{|\kappa_{ac}|^2 - \delta^2} \ \cosh(\sqrt{|\kappa_{ac}|^2 - \delta^2} \ L)} \tag{2.51}$$

and the reflectivity is defined as:

$$r = |\rho|^2 = \frac{\sinh^2(\sqrt{|\kappa_{ac}|^2 - \delta^2} \ L)}{\cosh^2(\sqrt{|\kappa_{ac}|^2 - \delta^2} \ L) - \frac{\delta^2}{|\kappa_{ac}|^2}}. \tag{2.52}$$

The relations show a number of interesting features:
The value of $\kappa_{ac}L$ is characteristic for the grating strength, i.e., the grating reflectivity, as can be seen in Fig. 2.4, where the grating reflectivity is calculated for a uniform grating for two different values of $\kappa_{ac}L$.

The presence of side lobes in the grating reflectivity is characteristic for uniform gratings. These side lobes can be suppressed by varying the coupling constant κ_{ac} over the grating length while maintaining a constant average refractive index. This procedure is called grating apodization [9] and is currently used for telecommunication applications where a top hat reflectivity is desirable.
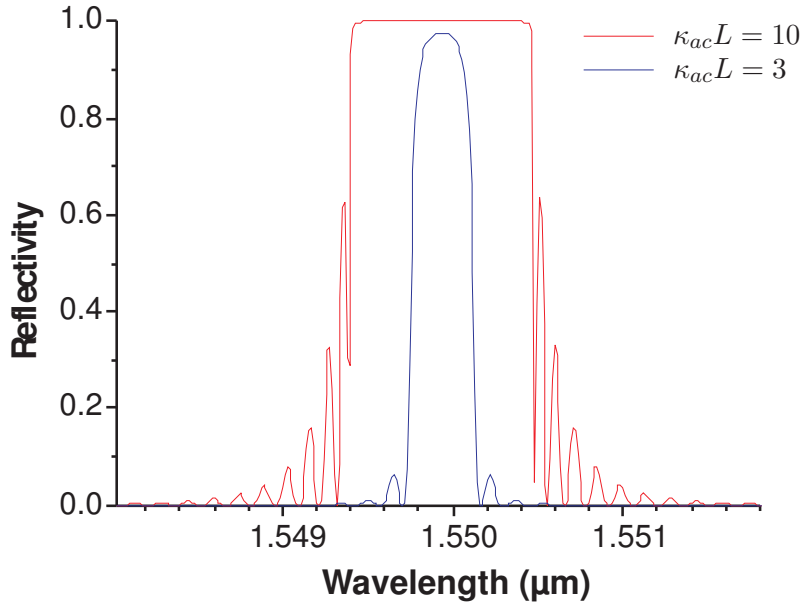The maximum reflectivity can be derived from Eq. (2.52) by setting $\delta = 0$ to

$$r_{max} = \tanh^2(\kappa_{ac}L) \tag{2.53}$$

at the wavelength defined by [9]:

$$\lambda_{max} = \lambda_B \left(1 + \frac{(\Delta n_0)_{\text{eff}}}{n_{\text{eff}}} \right). \tag{2.54}$$

The term $(\Delta n_0)_{\text{eff}}$ can be interpreted as the change in the mode effective index induced by the average refractive index change of the grating.

Figure 2.4: Calculated reflection spectrum for two uniform gratings with $\kappa_{ac}L = 3$ (blue line) and $\kappa_{ac}L = 10$ (red line). The grating length is 5 mm in both cases.

2.3.3. Bandwidth

The bandwidth of the grating is defined as the width between the first zeros on either side of the maximum reflection. Using Eq. (2.52), we obtain [9]:

$$\frac{\Delta\lambda_0}{\lambda} = \frac{(\Delta n_m)_{\text{eff}}}{n_{\text{eff}}}\sqrt{1 + \left(\frac{\lambda_B}{(\Delta n_m)_{\text{eff}}L}\right)^2}. \tag{2.55}$$

For femtosecond written FBGs the use of the coupling constant κ_{ac} is more appropriate, as the refractive index change is not homgeneously distributed over the whole fiber core and can be determined with precision from the grating response (see Sec. 4.3.2). Thus, inserting Eq. (2.49) in Eq. (2.55) the first zeros bandwidth reads as

$$\frac{\Delta\lambda_0}{\lambda} = \frac{\kappa_{ac}\lambda}{\pi n_{\text{eff}}}\sqrt{1 + \left(\frac{\lambda_B\pi}{\lambda\kappa_{ac}L}\right)^2}. \tag{2.56}$$

Depending on the grating strength, the grating bandwidth demonstrates two different behaviors:

Length limited (weak gratings)

For weak refractive index changes, i.e. $\kappa_{ac}L \ll \pi$, the bandwidth is inversely proportional to the grating length and reads as:

$$\frac{\Delta\lambda_0}{\lambda} \rightarrow \frac{\lambda_B}{n_{\text{eff}}L} = \frac{2}{L}. \tag{2.57}$$

Bandwidth limited (strong gratings)

For strong gratings where $\kappa_{ac}L \gg \pi$, the bandwidth depends only on the modulation of the refractive index change as can be seen in the following expression

$$\frac{\Delta\lambda_0}{\lambda} \rightarrow \frac{(\Delta n_m)_{\text{eff}}}{n_{\text{eff}}}. \tag{2.58}$$

Indeed, as the grating gets stronger, the effective grating length assuring the reflection decreases. This leads to a broader reflection spectrum, as can be seen in Fig. 2.4 for $\kappa_{ac}L = 10$, and to a deviation from a symmetric sinc or a Gaussian shape for the main reflection peak (see Fig. 2.4 for $\kappa_{ac}L = 3$).

For strong gratings, the Full Width at Half Maximum (FWHM) bandwidth is equivalent to its first zeros bandwidth. For weak gratings however, the behavior between FWHM and first zeros bandwidth depends on the grating strength and length [14].

The analytical solutions for the grating reflectivity and the grating bandwidth exposed here are only valid in the case of uniform gratings. For real gratings with more complex index modulation profiles, the reflectivity spectra and other grating characteristics like phase and group delay differ from the uniform grating case and can be modeled using numerical methods like the transfer matrix method [15] or Rouard's Method [16]. The complex grating shape is then decomposed into sections of small uniform gratings or into a thin-film stack of layers having a half-period width, respectively.

2.3.4. Cladding mode coupling

Even for a short period grating, a coupling to the cladding modes can be observed for wavelengths shorter than the Bragg reflection wavelength if the phase matching condition (Eq. (2.39)) is fulfilled and the overlap integral (Eq. (2.41)) is non-null.

In the theory, the refractive index modulation induced in the fiber core is considered as

constant over the whole fiber core and the overlap integral between the cladding modes, the grating transverse profile and the fundamental mode is null for cladding modes with azimuthal order $l > 1$ due to their parity [17]. However, a coupling from the core mode into the cladding modes occurs for low-order ($l = 1$) odd modes, as those cladding modes contain non negligible intensities symmetrically distributed over the fiber core. Nevertheless, when the refractive index modulation is non-constant over the fiber core, as is the case for UV written gratings as part of the inscription beam is strongly absorbed while propagating through the fiber core, the overlap integral of the cladding modes with azimuthal order $l > 1$ with the fundamental core mode is non-null. Thus, the coupling of the core mode into the cladding modes occurs for a greater number of modes.

In order to find the wavelengths for which phase matching occurs, the evolution of the propagation constant of the cladding and core modes with the wavelength must be studied. For that purpose, we derive from Eq. (2.39) the general phase matching condition

$$\beta_2 = \beta_1 - \frac{2\pi m}{\Lambda}, \tag{2.59}$$

with β_1 and β_2 being the propagation constants of the fundamental core mode and of the mode being coupled to, respectively. The direction of propagation is given by the sign of the propagation constants.

Using the definitions of the propagation constants $\beta_1 = \frac{2\pi}{\lambda} n_{\text{eff}_1}$ and $\beta_2 = \frac{2\pi}{\lambda} n_{\text{eff}_2}$, Eq. (2.59) becomes

$$n_{\text{eff}_2} = n_{\text{eff}_1} - \frac{m\lambda}{\Lambda}. \tag{2.60}$$

For a better understanding, Fig. 2.5 shows a diagram of the evolution of the effective refractive index for the fundamental core mode ($n_{\text{cl}} < |n_{\text{eff}}| < n_{\text{co}}$) and a backward- and a forward-propagating cladding mode ($1 < |n_{\text{eff}}| < n_{\text{cl}}$) with respect to the wavelength (see Sec. 2.1.1). These curves are obtained from the dispersion relation of the modes. The continuum of radiation modes is obtained for $|n_{\text{eff}}| < 1$ when the coating of the fiber has been removed, which is usually the case when FBGs are written. The direction of propagation is given by the sign of the effective refractive index.

For a FBG, Bragg reflection takes place at the Bragg wavelength verifying Eq. (2.60) for the coupling between the forward- and the backward-propagating core mode. This phase matching condition is shown in Fig. 2.5 by the arrow representing the ratio $m\lambda_B/\Lambda_{FBG}$. For the same grating pitch Λ_{FBG}, a coupling between the core fundamental mode and one of the backward-propagating cladding modes ($-1 < n_{\text{eff}} < -n_{\text{cl}}$) can also occur for a wavelength λ_1 slightly shorter than λ_B as the effective refractive index of the fundamental core mode increases. As several cladding modes are bounded to the fiber, several discrete transmis-
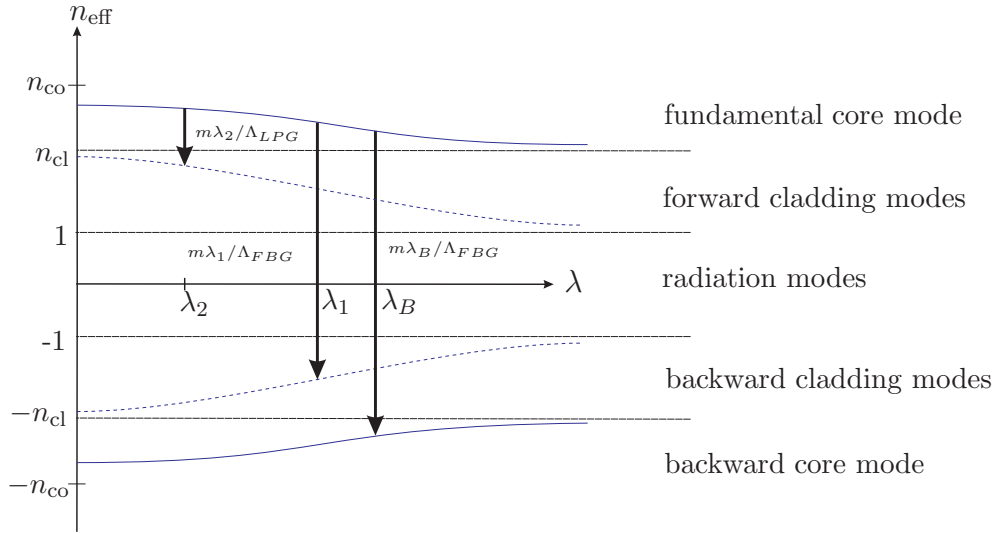
Figure 2.5: Illustration of the phase matching condition $n_{\text{eff}_2} = n_{\text{eff}_1} - m\lambda/\Lambda$ using the mode dispersion diagram (from [18], modified). n_{eff_1} corresponds here to the fundamental core mode. n_{eff_2} is the mode into which the light is coupled. In the diagram, the arrows stand for $-m\lambda/\Lambda$.

sion losses appear on the shorter side of the Bragg wavelength and have no impact on the grating reflectivity. The cut-off wavelength as well as the distance between each peak can be determined by applying the coupled-mode theory to cladding modes [19]. A coupling to the radiation modes can also occur for shorter wavelengths but is not clearly visible, as the coupling is continuous and further away from the Bragg wavelength. Furthermore, a coupling of the fundamental mode into the forward-propagating cladding modes can be achieved with much bigger grating pitches (as represented in Fig. 2.5 by the arrow $m\lambda_2/\Lambda_{LPG}$).

After this short introduction to the basics of the FBG theory, the next chapter will consider the different possible techniques for the inscription of FBGs in photosensitive as well as in non-photosensitive and in rare-earth doped fibers.

3. Fiber Bragg gratings inscription

This chapter gives a brief review of the commonly used UV inscription techniques and the mechanisms linked to fiber photosensitivity and refractive index change. The achieved refractive index changes are strongly dependent on the fiber composition as well as on the type of laser used making the inscription of strong reflecting FBGs into actively doped fibers difficult to realize. For that reason, a more flexible technique based on the multi-photon absorption of IR femtosecond pulses has been developed to realize FBGs almost independent of the fiber composition. As ultrashort pulses have short coherence lengths, standard interferometric setups are difficult to use and other inscription techniques such as the "point by point" or the "phase mask scanning" technique are more promising. As high energy densities are needed to overcome the threshold for permanent material modification, a strong focusing of the laser beam and an accurate positioning of the focused beam into the fiber core are necessary for the realization of high quality FBGs. Both issues are also treated in the following chapter.

3.1. Laser induced refractive index change

This section gives an overview of the different techniques to induce a refractive index change in a glass using laser radiation. Historically, refractive index changes were first induced in germanosilicate fibers by Hill *et al.* in 1978 [1, 20] while studying the non-linear properties of germanium-doped silica fibers. By launching intense 488 nm Argon-ion laser radiation into a germanium doped fiber, the first Bragg grating was written by a standing wave pattern resulting from the partial reflection of the laser radiation at the fiber end facet. Further studies showed that the photosensitivity was due to a two photon absorption in the germanium oxygen-vacancy defect band [21]. Meltz *et al.* demonstrated in 1989 that gratings could be written in a more efficient way using a transverse holographic method and single photon absorption at 244 nm [22]. Since then Bragg gratings have been usually written using UV light into photosensitive fibers. To overcome the use of photosensitive fibers, ultrashort pulses can be used to induce refractive index changes based on the non-linear absorption of the pulses. This method has the advantage that Bragg gratings can be inscribed into fibers practically independent of their chemical composition.

3.1.1. Refractive index change induced by UV radiation

The inscription of fiber Bragg gratings using UV radiation is based on the linear absorption of the radiation in the core of photosensitive fibers. Photosensitive fibers are containing defects in the fiber core that allow the absorption of UV light within its absorption bands around 240-250 nm and below 200 nm. The main absorption band around 240 nm is linked to the presence of Ge-Si and Ge-Ge "wrong bonds" [23] formed during the Modified Chemical Vapor Deposition (MCVD) process in the core of germanosilicate fibers. The structural changes resulting from the absorption and breaking of the bonds are responsible for a change in the refractive index. Other fiber compositions also allow the absorption of UV light through the presence of defects but the highest photosensitivity (i.e. capacity to induce a refractive index change) is only reached by germanosilicate fibers. However, the photosensitivity can be additionally increased by hydrogen loading (also called hydrogenation), by flame brushing or boron codoping [24].

Hydrogen loading [25] is done by diffusing hydrogen molecules into the fiber core at high temperatures and pressures. The hydrogen molecules react in the glass at normal Si-O-Ge sites, forming OH species and UV bleachable germanium oxygen deficiency centers, which are responsible for the enhanced photosensitivity [26]. Using that technique, refractive index changes up to 1×10^{-2} can be achieved even in optical fibers with low germanium concentrations such as standard telecommunication fibers. Unfortunately, the increase in the photosensitivity is not permanent as the hydrogen diffuses out of the fiber. Thus, hydrogenated fibers must be used quickly after having been loaded with hydrogen.

The flame brushing technique [27] is based on a similar process. The fiber is brushed repeatedly by a flame fueled with hydrogen and a small amount of oxygen. The flame reaches a temperature of 1700 °C and the hydrogen diffuses into the fiber core very quickly reacting with the germanosilicate glass to produce germanium-oxygen deficient centers. Using that technique, refractive index changes $> 10^{-3}$ have been achieved in standard telecommunication fibers [27]. In contrary to the hydrogen loading technique, the increased photosensitivity is permanent. However, the major drawback of this technique is that the high-temperature flame weakens the fiber.

Germanosilicate fibers co-doped with boron demonstrate a higher photosensitivity than a high germanium doped fiber without boron co-doping [28]. However boron co-doping does not enhance the absorption of the fiber and another mechanism should be responsible for the increased refractive index change. It is believed that boron co-doping facilitates photoinduced stress relaxation initiated by the breaking of the wrong bonds.

26

Mechanisms responsible for the refractive index change

Irradiating the photosensitive fiber with 240 nm UV light ionizes a Ge-Si "wrong bond" leaving the germanium atom with one unpaired electron occupying a tetrahedral (sp^3) orbital (see Fig. 3.1 a)). This defect is called GeE' center and is creating a new absorption band at 195 nm. The free generated electrons can diffuse in the glass matrix and can be trapped by Ge(1) or Ge(2) defects [29] to form Ge(1)$^-$ and Ge(2)$^-$ centers. Those defects are comprised of an electron trapped at a normal four-coordinated germanium atom having a distortion of the tetrahedral structure. The Ge(1)$^-$ center is coordinated to four O-Si bonds and the Ge(2)$^-$ center to one O-Ge and three O-Si bonds (see Fig. 3.1 b)). Those defects are associated with new absorption bands at 281 nm and 213 nm, respectively [30, 31].
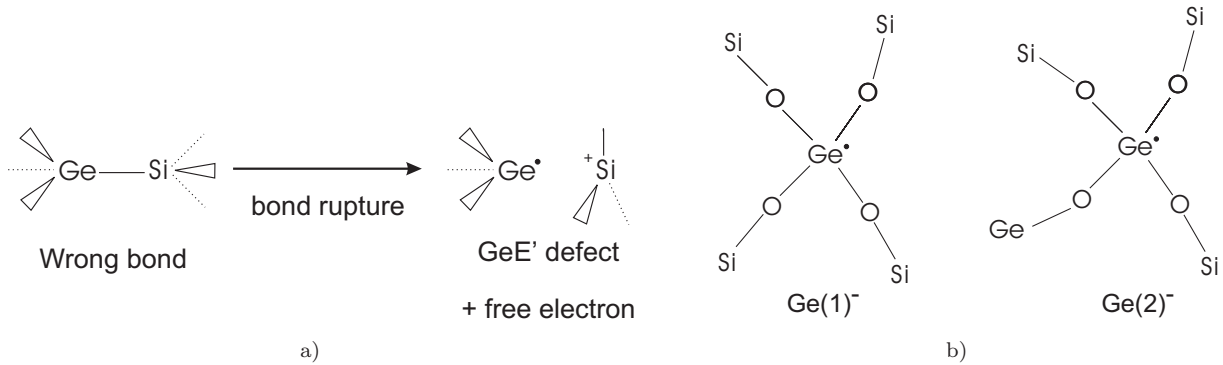
Figure 3.1: Representation of point defects present in germanosilicate glasses: a) Rupture of the Ge-Si "wrong bond" and formation of a GeE' defect, b) the Ge(1)$^-$ and Ge(2)$^-$ centers (after [32]). The dot symbolizes an unpaired electron.

The change in the absorption bands could be responsible for the refractive index change according to the Kramers-Kronig relationship [33]. However, the refractive index change evaluated with this model is smaller than the measured change. It is thus more likely that the refractive index change is due to a combination of other mechanisms [24]. Fonjallaz *et al.* [34] observed a strong tension increase in the fiber core after illumination with UV light. This tension increase was proportional to the refractive index modulation. Although an increase in the tension lowers the refractive index through the photoelastic effect, a mean positive refractive index change was observed in the experiments. The proposed densification model [35] considers structural changes into more compact configurations as an important component of fiber photosensitivity. The UV-induced increase of the refractive index in the fiber core, due to both color-center and compaction effects, is believed to exceed the decrease caused by the photoelastic effect. The amount of each contribution might vary strongly as a function of fiber content, pre-irradiation treatment and irradiation wavelength.
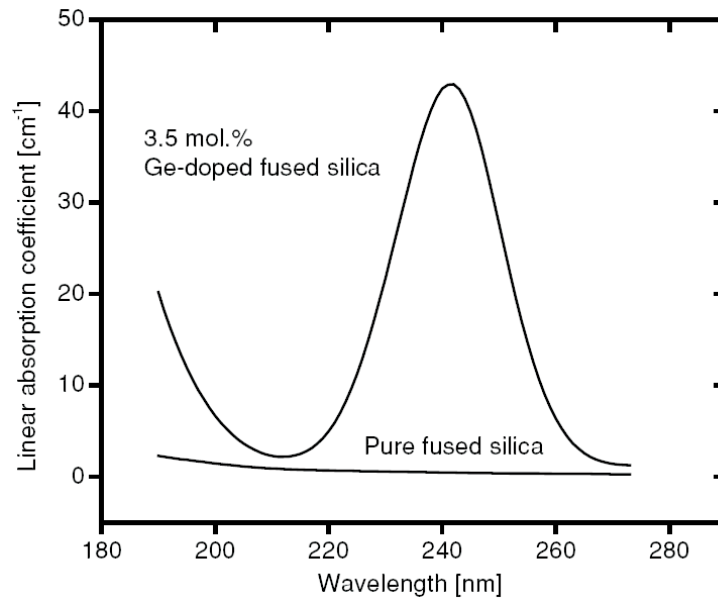
Figure 3.2: Absorption properties of pure fused silica and germanosilicate glass [36].

FBG inscription

Some of the main laser sources used for the grating inscription are shown in Table 3.2. Their wavelengths coincide with the absorption bands of the photosensitive fibers as can be seen in Fig. 3.2. The inscription method is chosen depending on the beam quality and spatial and temporal coherence of the source.

For lasers having good temporal and spatial coherence, beam splitting interferometers can be used which allow great flexibility in the choice of the grating period by adjusting the angle between the two overlapping beams. With those sources, good quality gratings can be written.

Low coherence sources such as excimer lasers provide high peak powers for the inscription of type II gratings (see next section). However, the quality of the gratings is affected by the low transverse coherence of the laser beam. Due to power density variations, the reflectivity and Bragg wavelength vary from grating to grating written with one pulse. One way to overcome the problem is to use multiple pulses to average out those effects. Another option is the use of phase masks placed in close proximity to the fiber. This approach is well suited for imprinting the interference pattern assuring low path differences between the overlapping beams.

LASER	WAVELENGTH	BEAM QUALITY	APPLICATION
KrF ns pulsed excimer laser	248 nm	low spatial / temporal coherence	Type II gratings mass production during fiber drawing
ArF ns pulsed excimer laser	193 nm	low spatial / temporal coherence	planar devices, non-Ge fibers
Argon ion laser (frequency doubled)	257 nm 244 nm	high coherence, good beam quality	interferometric, contact and non-contact phase mask

Table 3.1: Some of the frequently used UV laser sources for grating formation adapted from [11].

Grating strength and temperature stability

Depending on the evolution of the grating strength during irradiation and on the thermostability, the gratings can be classified into three groups:

- *Type I gratings* are inscribed with UV fluences well below the damage threshold of the material involved. The refractive index change gradually increases with irradiation time. Those gratings are of good quality but have a low thermal stability. For example, 90 % of the initial grating reflectivity is remaining after exposition of a FBG written in a highly germanium doped fiber to a temperature of only 250°C [37]. Furthermore, hydrogen loaded fibers demonstrate an even lower thermal stability as their unloaded counterparts for small temperatures [38, 39].

- *Type IIA gratings* appear after the growth and erasure of a type I grating into fibers with high germanium concentration (20 mol% or more) in the absence of hydrogenation. During the formation of the type I grating, the average refractive index is positive whereas it is negative during the erasure of the type I grating and the formation of the type IIA grating [40, 41]. Thus the evolution of the refractive index change with time results from two different local reactions. The first producing some defects and the second results in a structural reorganization. Generally type IIA gratings have a better temperature stability than the initial type I grating like in boron-codoped germanosilicate fibers [42].

- *Type II gratings* are damage gratings which are obtained when the pulsed UV source fluence is greater than the damage threshold of the fiber. Those gratings have high reflectivities and bandwidths as well as a good thermal stability. For example, gratings

written with a 30 ns 40 mJ KrF laser pulse are stable over 24 hours at a temperature up to 800°C whereas a grating written with a pulse energy of 30 mJ can be erased within seconds at 450°C [43].

In conclusion, the quality and strength of the gratings written using UV radiation depend on the fiber composition or photosensitization technique as well as on the laser source used. The photosensitivity of germanosilicate fibers can be improved by hydrogen loading. However, for aluminosilicate and phosphosilicate fibers other dopants must be used to increase the photosensitivity [44] which is lower as for germanosilicate fibers.

Recently, an alternative method based on the two-step absorption of a pulsed ArF laser (pulse duration $\sim$ 15ns) [45] has been used for the inscription of FBGs into non-photosensitive fibers. A refractive index change of $\sim 3 \times 10^{-4}$ could be realized but the use of a fluorine-depressed cladding was necessary to lower the absorption before the fiber core was reached. Thus, this method is still linked to the use of specially prepared fibers to obtain high refractive index changes.

3.1.2. Refractive index change induced by femtosecond pulses

Due to their extremely high intensities, the non-linear absorption of femtosecond pulses can be used as a new approach to induce refractive index changes in transparent materials. Near IR femtosecond pulses are usually used and the modifications of the refractive index change are located at the focus of the laser beam. Using this technique, waveguides in different glasses and crystals [4, 46–48] as well as three-dimensional guiding structures such as 3D beam splitters [2] and 3D arrays [3] have been realized. Such refractive index changes are well suited for the realization of fiber Bragg gratings.

Femtosecond laser systems

Different femtosecond laser systems can be used like Titanium:Sapphire solid state lasers or Ytterbium based fiber laser systems. Intensities of the order of 1 to $5 \cdot 10^{13} \text{W/cm}^2$ are necessary to enable the non-linear absorption which corresponds to fluences of 1 to 5 J/cm^2 for 100 fs pulses [49]. Such fluences can only be reached by focusing the femtosecond pulses. For energies of the order of the nJ, the laser beam has to be tightly focused (close to the diffraction limit) whereas for pulse energies in the range of the µJ, a milder focusing is sufficient.

Furthermore, the laser repetition rate has an influence on the morphology of the modifications induced in the glass material. For low repetition rates, the time between each pulse is larger than the time necessary for the deposited energy to diffuse out of the focal volume ($\tau \sim 1\,\mu s$). Thus, the modification is the result of the interaction of each pulse. The modification is restricted to the focal region which has an asymmetric shape [50]. For high repetition rates, the time between each pulse is lower than the time necessary for the deposited energy to diffuse out of the focal volume and a heat accumulation occurs. Consequently, the induced modifications have a spherical shape, whose size is depending on the accumulated fluence and on the repetition rate of the laser [51, 52].

Mechanisms responsible for femtosecond-laser-induced structural changes

By focusing femtosecond pulses inside the bulk of a transparent material the intensity in the focal volume can become high enough to initiate absorption through nonlinear field ionization (multiphoton absorption and tunneling ionization) and avalanche ionization [53–55]. Through the recombination of the electron-ion plasma created in the focal volume and the dissipation of its energy, permanent structural changes can be induced in the material. Three different types of structural changes take place depending on the laser parameters (like pulse duration, wavelength, energy, repetition rate of the laser), the focusing conditions (i.e. the numerical aperture of the focusing lens) and the material parameters (thermal expansion coefficient and bandgap of the material):

For low energy densities, an isotropic refractive index change [46, 47] is observed and is attributed to localized melting and rapid resolidification of the glass [56]. Depending on the glass thermal behavior, the refractive index and material density can increase or decrease [57]. Indeed, when the glass is heated and rapidly cools down, the properties of the higher temperature state are frozen in the material. For fused silica, an increase of the material density (i.e. a densification of the material) and accordingly an increase of the refractive index change have been observed with typical values of $\sim 10^{-3}$ [58].

For high energy densities, voids resulting from an explosive expansion of highly excited, vaporized material out of the focal volume is observed. The microexplosion leaves a less dense or hollow core surrounded by a densified shell of material [59, 60].

For intermediate energy densities, a birefringent refractive index change is observed [61]. Here, the presence of nanogratings consisting of layers with different densities leads to a form birefringence. Interference between the femtosecond laser field and the electric field of bulk electron plasma waves in the laser-produced plasma could be responsible for the formation of the layers of different densities [62].

Temperature sustainability of the refractive index modifications

Similar to UV induced refractive index changes, IR femtosecond pulses can induce two types of modifications with different temperature dependent behavior depending on the energy deposited, as first demonstrated by Sudrie *et al.* in bulk glass [61]. Type I modifications are obtained for low energies and are fully erased at a temperature of 900°C whereas type II modifications subsist after heating at 900°C and are obtained from higher pulse energies. A similar temperature dependent behavior is also expected for the femtosecond written FBGs.

These different temperature behaviors correspond to different types of refractive index modifications. Type I modifications correspond to an isotropic refractive index change resulting from a material densification in fused silica whereas type II corresponds to a microexplosion resulting from the overdense ion-electron plasma. The power thresholds for type I and type II modifications were measured at 0.63 MW and 1.94 MW respectively for a microscope objective with a numerical aperture of 0.5 and a pulse duration of 110 fs. These thresholds should be expressed in terms of threshold intensities (W/cm^2) in order to take into account the focusing conditions and pulse durations and allow the comparison with other experiments.

3.2. FBG inscription using femtosecond pulses

The aim of this section is to describe the techniques that can be used for the inscription of fiber Bragg gratings with near IR ultrashort pulses. Due to the short coherence length of femtosecond pulses, conventional interferometric methods are difficult to use. Therefore, two other methods can be applied: the "point by point" technique and the "phase mask" technique. After a short description of the "point by point" technique, we put the emphasis on the "phase mask" technique which is used for the inscription of the FBGs in this thesis. Specific issues linked to beam focusing and fiber positioning are also discussed.

3.2.1. "Point by point" technique

The principle of the "point by point" writing technique can be seen in Fig. 3.3. The laser beam is focused into the fiber core and the refractive index is locally modified at the laser focus. The fiber is then translated a distance Λ_G along the fiber axis before the next modification is introduced to produce a periodical refractive index change of period Λ_G. By translating the fiber with a constant velocity, each pulse produces a localized refractive index change
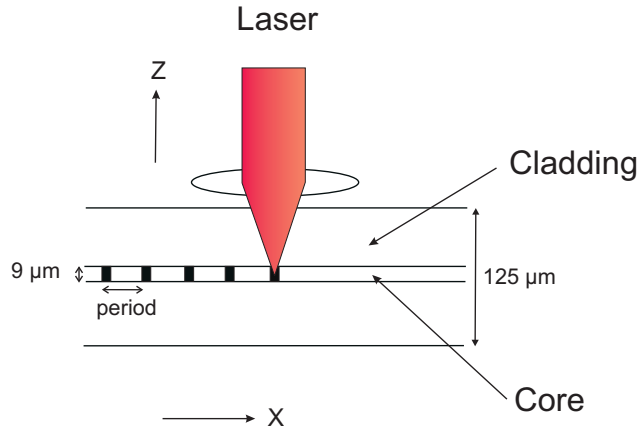
Figure 3.3: Schematic of the FBG inscription using a "point by point" technique. The tightly focused laser beam produces a refractive index change localized in the fiber core with a periodicity Λ_G.

separated by a distance inversely proportional to the laser repetition rate and proportional to the translation velocity [63].

To increase the efficiency of the fiber grating, the fiber can also be translated in the y-direction before being translated in the direction of the fiber axis by the distance Λ_G [64]. Thus, a plane of refractive index is inscribed in the whole fiber cross-section and the overlap between the grating and the guided mode is maximized. However, this method requires longer fabrication times due to the fiber translation along the y-axis. An alternative method is to perform a beam shaping of the laser beam to get an elliptical focus with its long axis orientated in the y-direction. Thus, the refractive index change is induced in the whole fiber core and the fiber is only translated along the fiber axis. Such a beam shaping method has already been used by Osellame *et al.* to realize waveguides with a circular cross-section to increase mode matching with standard telecommunication fibers [65].

Both methods allow the realization of gratings with a high flexibility in the grating period. However, the laser beam has to be tightly focused by a microscope objective and the positioning of the modifications into the fiber core is quite difficult to realize with the required precision. Moreover, the grating quality strongly depends on the accuracy of the positioning system.

3.2.2. "Phase mask" technique

Another possibility to inscribe a periodical refractive index change into the fiber core is the use of an interferometric method based on the overlap of two beams having different angles of incidence. Due to the short coherence length of the femtosecond pulses, a setup using mirrors and a delay line is difficult to use. The use of a phase mask is therefore preferable to

produce the two interfering beams. By overlapping a pair of diffraction orders, a high contrast interference pattern is obtained quite easily as the two overlapping beams have propagated the same distance. This technique has been used within this thesis.

Usually, the phase mask is illuminated at normal incidence and the +1st and -1st orders overlap in the vicinity of the phase mask (Fig. 3.4). The period of the interference pattern is then half of the phase mask pitch.
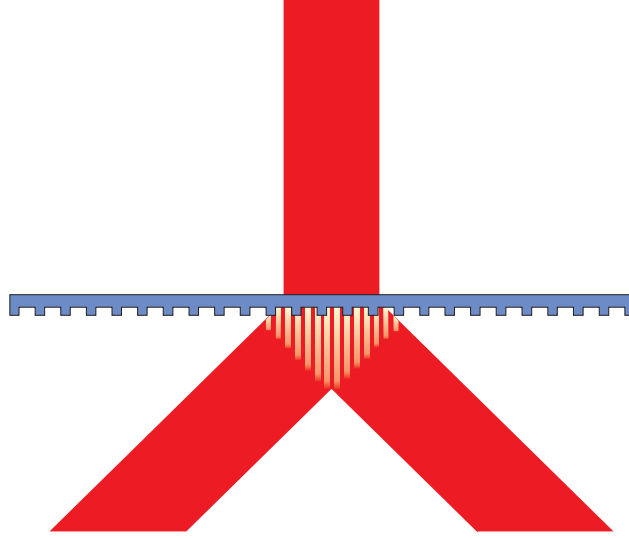
Figure 3.4: Interference after the phase mask resulting from the overlap of the +1st and -1st diffraction orders.

The phase masks were produced in our institute with electron beam lithography and an ion etching technique in a fused silica substrate of 1.5 mm thickness. The phase masks are written by exposing the glass substrate to an rectangular pattern having the width of the grating groove and the substrate is translated of the phase mask period before the next exposure to the electron beam. The precision accuracy of micropositioning of the electron beam (Jenoptik,ZBA 23) is of 2.5 nm. The phase masks are designed for the center wavelength $\lambda = 800$ nm of our femtosecond laser system (Sec. 3.3.1). The period of the phase-masks is chosen according to Eq. (2.15), λ_B being the designed Bragg wavelength. The measured Bragg wavelength λ_{max} differs from the theoretical Bragg wavelength due to the induced average refractive index change (Eq. 2.54). Typical phase masks characteristics are resumed in Table 3.2 for different Bragg wavelengths.

1.55 µm is a typical wavelength for telecommunications systems operating in the C- Band and based on Erbium fiber amplifiers. 1.04 µm is a typical wavelength for ytterbium doped fiber lasers. For such a short Bragg wavelength first order Bragg gratings cannot be written with the inscription wavelength of $\lambda_i = 800$ nm since in this case it follows for the phase mask period $\Lambda_{pm} \leq \lambda_i$. This phase mask can not generate +1st and -1st diffraction orders.

Λ_{pm}	Λ_{FBG}	λ_B	m	θ
1.075 µm	0.5375 µm	1.553 µm	1	48.1°
2.15 µm	1.075 µm	1.553 µm	2	21.8°
1.435 µm	0.7375 µm	1.036 µm	2	33.9°

Table 3.2: Some typical phase masks periods Λ_{pm} used for the FBG inscription. The design Bragg wavelengths λ_B are given for an effective refractive index $n_{\text{eff}} = 1.445$, which is the refractive index of fused silica near 1.55 µm with a refractive index increase of 1×10^{-3} due to the fiber grating inscription. Depending on the fiber used, the n_{eff} and thus the resulting Bragg wavelength λ_B may differ. The diffraction angle θ for the 1st diffraction order is useful for the calculations of the effective overlap length (Eq. (3.3)) for example.

Therefore, phase masks designed for the second order diffraction are used for the FBG inscription at 1.04 µm. FBGs are also written and characterized in the second diffraction order for a Bragg wavelength of 1.55 µm (see Sec. 4.3). The optimized parameters will be used for the inscription of second order gratings at 1.04 µm in Sec. 5.2.1.

If the phase mask also diffracts the beam into other diffraction orders, the interference pattern resulting for the overlap of the diffracted beams will become more complex and show a periodicity in the z direction as well as a perturbation of the periodicity in the x direction. Considering two different diffraction orders n and p, the longitudinal and transverse periods can be derived from a scalar treatment [66] to

$$\Lambda_z = 2\pi/(k_{nz} - k_{pz}) \tag{3.1a}$$

$$\Lambda_x = \frac{\Lambda}{|n - p|}, \tag{3.1b}$$

where k_{nz} and k_{pz} are the projections of the diffracted wave vectors in the z direction.

Thus, good quality interference patterns will be obtained by maximizing the diffraction efficiency of the +1st and -1st orders as well as minimizing the other diffraction orders. The 0th order can be minimized by destructive interference between light transmitted through the etched and non-etched regions of the phase mask. The efficiency of the +1st and -1st diffraction orders can be maximized by choosing an appropriate width and depth for the grating grooves as can be seen Fig. 3.5. The graph represents the first order diffraction efficiency versus the depth and the fill factor of the grating grooves. The fill factor is defined as the ratio of the width of the grooves to the period. The zeroth order diffraction efficiency in percent is shown by the isocurves. The calculation was made using the commercial GSOLVER software[1] (Grating Solver Development Co.) for a grating having a period of 2.15 µm and for an inscription wavelength of 800 nm (see Sec. 3.3.1). Note that the maximum efficiency of

---

[1]calculations made by Tina Clausnitzer, Institute of Applied Physics, Friedrich-Schiller-University Jena

the first diffraction order does not correspond to a minimum for the zeroth diffraction order. Thus, for the fabrication of the phase masks used in this thesis the grating grooves depth was chosen to minimize the 0th diffraction order at the expense of the 1st order diffraction efficiency.
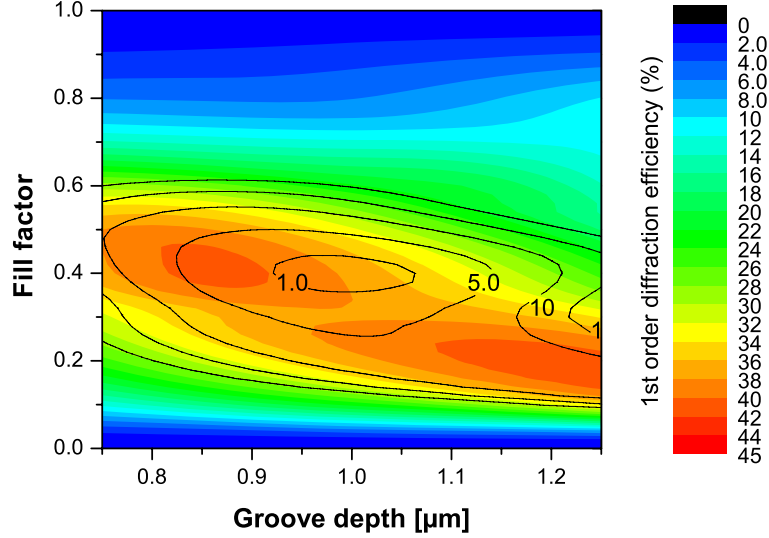

Figure 3.5: Diffraction efficiency of the 1st order versus depth and fill factor of the grating grooves. The grating period is 2.15 µm and the illumination wavelength 800 nm. The diffraction efficiency in percentage is represented by colors for the 1st order and by isocurves for the the 0th order.

Unfortunately, the grating groove depth and width chosen to maximize the +1st and -1st diffraction order and minimize the 0th order does not necessary lead to non-existing higher orders. However, due to their larger diffraction angle, the higher diffraction orders will not overlap if the fiber is placed sufficiently far away from the phase mask in contrast to the 0th order that will always overlap with the 1st diffraction order.

However, a pure two beam interference pattern can be obtained with femtosecond pulses using the order walk-off effect [67]. As the pulses are diffracted into diffraction orders having different angles, pulses diffracted into the ± 1st orders will need more time to reach the fiber core as the 0th order propagating perpendicularly to the phase mask, for example. Thus, by placing the fiber far enough from the phase mask, the 0th and 1th orders will reach the fiber with a time difference greater than the laser coherence time resulting in a pure two-beam interference pattern [68].

The necessary distance between the phase mask and the fiber can be found using a simple geometrical model as represented in Fig. 3.6.
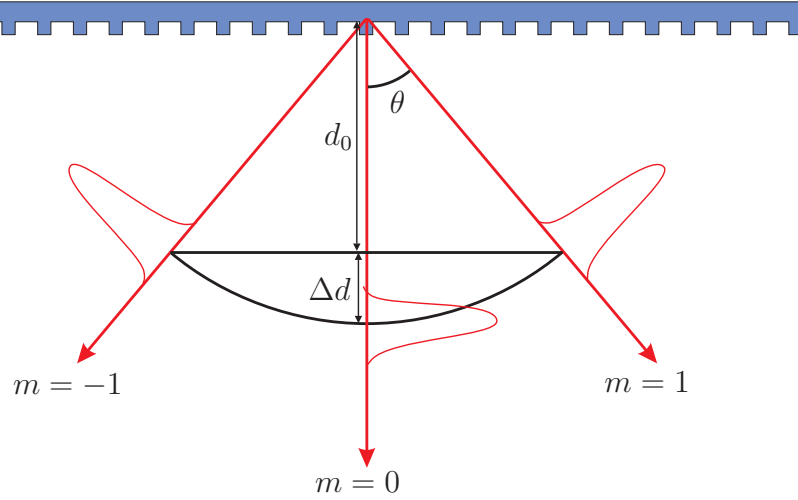
Figure 3.6: A geometrical explanation of the order walk-off after a phase mask observed with ultrashort pulses for the $\pm$ 1st and 0th order.

With d_0 being the distance between the phase mask and the fiber core (i.e. the distance for the plane of observation), the distance between the pulses diffracted through the zeroth and the first order can be determined using the following geometrical relation

$$\Delta d = d_0 \left(\frac{1}{\cos(\theta)} - 1 \right), \tag{3.2}$$

θ being the diffraction angle for the first order defined by Eq. (2.12).

Pure two beam interference will be obtained for $\Delta d >> l_{coh}$. As an example, for femtosecond pulses with a pulse duration of 50 fs, the coherence length of the pulses is of 10 µm.

Another parameter to consider while increasing the distance between the phase mask and the fiber is the effective overlap of the +1st and -1st diffraction order. The effective overlap length $L_{overlap}$ can be calculated using a simple geometrical formula as

$$L_{overlap} = 2\omega - 2d_0 \tan\theta, \tag{3.3}$$

where ω is the laser beam radius, d_0 the distance between the phase mask and the fiber and θ the diffraction angle for the first diffraction order. The effective overlap length is an important parameter to take into account while comparing gratings written under different conditions such as different phase mask/fiber distances and diffraction angles resulting from the use of phase-masks designed for the inscription of FBGs of different order like in Sec. 4.2 and Sec. 4.3.

3.2.3. Beam focusing and fiber positioning

Using femtosecond pulses to induce the refractive index change requires a tighter focusing of the laser beam as usually used for the UV inscription of fiber gratings due to the non-linear absorption processes involved. Furthermore, as the refractive index change is induced in the focal region of the laser beam it is essential to position those modifications accurately into the fiber core [68].

Preliminary experiments showed that it is impossible to induce modifications into the core of a fiber having a 125 µm cladding diameter using a cylindrical lens of focal length 60 mm with a laser beam having a beam radius of 2.4 mm. In this case the fiber curvature is not negligible and has to be taken into account while focusing the laser beam into the fiber. In order to simplify the modeling of the focusing to a one-dimension problem, we consider the case of a cylindrical lens (see Fig. 3.7) which is typically used in the phase mask approach.

Beam focusing with low NA cylindrical lens

As the laser beam has a Gaussian profile, Gaussian beam optics and the paraxial approximation will be used to study the influence of the fiber curvature on the focusing of the laser beam.

The evolution of the Gaussian beam with its propagation direction z can be defined by its intensity $I(x, y, z)$ as:

$$I(x, y, z) = I_0 \left[\frac{W_0}{W(z)} \right]^2 \exp \left[-\frac{2(x^2 + y^2)}{W(z)^2} \right] \tag{3.4}$$

with $W(z)$ being the width of the beam defined by $W(z) = W_0 \left[1 + \left(\frac{z}{\rho} \right)^2 \right]^{1/2}$ in the plane (x, y) perpendicular to the propagation direction z. W_0 is called beam waist and is linked to the Rayleigh length ρ by $W_0 = \left(\frac{\lambda \rho}{\pi} \right)^{1/2}$.

In the general case, let's consider an optical fiber having a cladding radius R and a refractive index n. The refractive index difference between the core and the cladding of the fiber is neglected. The optical axis is taken normal to the fiber axis and the beam waist position before and after passing through the fiber surface are z and z'. At the fiber surface, we set $z = 0$.

To successfully inscribe FBGs using non-linear absorption processes, the beam waist position has to be within the fiber core ($z' = R$).

The propagation of optical rays through an optical system can be calculated in the paraxial
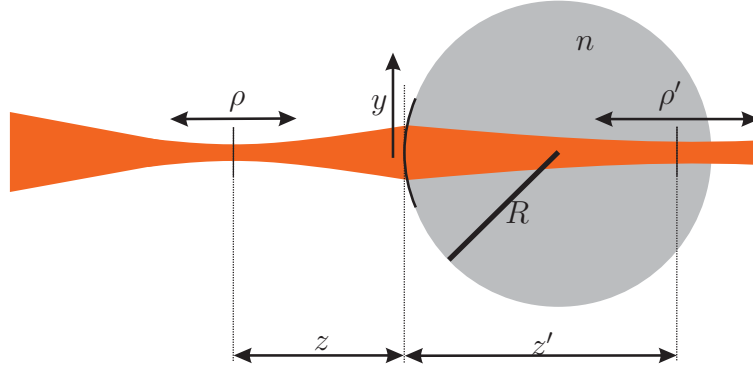
Figure 3.7: Illustration of the influence of the curved fiber surface on a focused Gaussian beam defined through its beam waist position z and its Rayleigh length ρ. Due to the fiber curvature, the focused beam is now positioned at a distance z' from the fiber surface and has a modified Rayleigh length ρ'.

approximation using the ray-transfer matrix method. A ray transfer matrix is defined through its components A, B, C, D and models for ray optics the change in the inclination and position of the light ray.

For Gaussian optics, the evolution of the beam waist and curvature radius can be described using the q parameter. With ρ and ρ' being the Rayleigh lengths of the Gaussian beam outside and inside the fiber, the complex q parameter is defined by $q = z + i\rho$ and $q' = -z' + i\rho'$. Thus the Gaussian beam inside the fiber can be described by the ABCD-law [69] defined as

$$q' = \frac{Aq + B}{Cq + D} \tag{3.5}$$

In the paraxial approximation, the ray transfer matrix of a curved boundary of radius R between air and the medium of refractive index n [70] is given by

$$M = \begin{pmatrix} A & B \\ C & D \end{pmatrix} = \begin{pmatrix} 1 & 0 \\ -\frac{n-1}{nR} & \frac{1}{n} \end{pmatrix} \tag{3.6}$$

By inserting Eq. (3.6) into Eq. (3.5) the real part of q' reads as

$$z'(z) = \frac{D}{C}\left(\frac{Cz + D}{(Cz + D)^2 + C^2\rho^2} - \frac{1}{D}\right), \tag{3.7}$$

and gives the position of the beam waist inside the fiber. The beam waist position z can be altered by the distance between lens and fiber.

The result can be generalized by normalizing the different parameters with the fiber radius

R. By setting $\tilde{z} = z/R$, $\tilde{z}' = z'/R$, $\tilde{\rho} = \rho/R$ and $\tilde{f} = n/(n-1)$, Eq. (3.7) becomes

$$\tilde{z}'(\tilde{z}) = -\frac{\tilde{f}}{n}\left(\frac{-\tilde{z}/\tilde{f} + 1/n}{(-\tilde{z}/\tilde{f} + 1/n)^2 + (\tilde{\rho}/\tilde{f})^2} - n\right). \tag{3.8}$$

This relation is shown in Fig. 3.8 for different values of the normalized Rayleigh length depending on the focal length of the focusing cylindrical lens. For large Rayleigh lengths i.e. large focal lengths (dotted line) the minimum position of the beam waist is located after the fiber core making the inscription of the Bragg grating impossible. For smaller Rayleigh lengths i.e. short focal lengths (solid and dashed line) the fiber core can be reached by the laser beam.
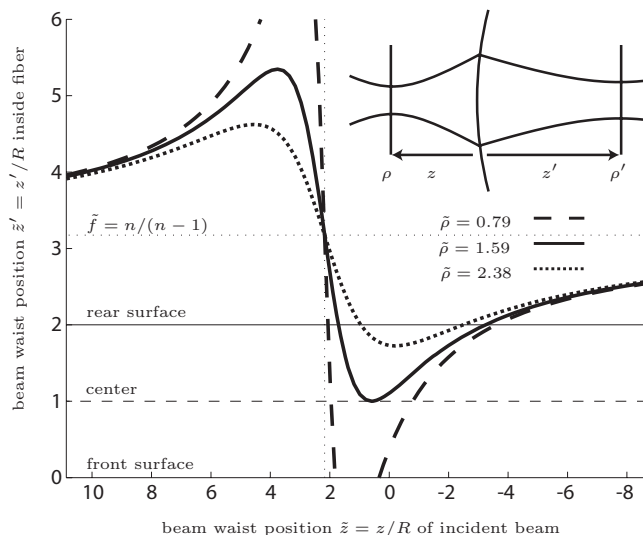
Figure 3.8: Beam waist position $\tilde{z}' = z'/R$ after a curved surface of radius R and a refractive index of $n = 1.457$ in dependence of the incoming beam waist position $\tilde{z} = z/R$.

In order to know the maximum Rayleigh length for which the fiber core can be reached, we calculate the minimal distance of the beam waist $\tilde{z}'$ by solving $(\partial\tilde{z}'/\partial\tilde{z}) = 0$. The minimal distance of the beam waist $\tilde{z}'$ measured from the curved surface is thus obtained for $\tilde{z}_{min} = \tilde{f}/n - \tilde{\rho}$ and evaluates to

$$\tilde{z}'(\tilde{z}_{min}) = \tilde{f}\left(1 - \frac{\tilde{f}}{2n\tilde{\rho}}\right). \tag{3.9}$$

The minimum beam waist position is precisely located in the center of the fiber for $\tilde{z}' = 1$ (see Fig. 3.8 solid line) when the normalized Rayleigh length $\tilde{\rho}$ equals $\tilde{f}/(2n(1-\tilde{f}))$ according to Eq. (3.9). Using the definition of the normalized focal length $\tilde{f} = n/(n-1)$, the minimum

position of the focused beam is located in the fiber core for

$$\rho = \frac{nR}{2(n-1)}. \tag{3.10}$$

By focusing the laser beam to that particular Rayleigh length allows the positioning of the laser beam into the fiber core with lower requirements on the positioning accuracy in that case.

Let us consider a standard single mode fiber around 1.55 µm with a cladding radius $R = 62.5$ µm and a core radius $r = 4.5$ µm. The refractive index is assumed to be uniformly $n = 1.457$ within the fiber, corresponding to pure fused silica at $\lambda = 800$ nm. Equation (3.10) yields an optimal Rayleigh length of $\rho = 100$ µm for the focused beam to just reach the fiber core. Using such focusing conditions, the divergence angle $\theta = \left(\lambda/(\pi\rho)\right)^{1/2} \approx 0.06 \ll 1$ is reasonably small and the paraxial approximation is still valid. For the grating inscription a laser with a beam radius of $W_0 = 2.4$ mm is used and a cylindrical lens having a focal lens of $f \approx 40$ mm should thus be used in order to meet the ideal Rayleigh length.

For real lenses the ray-transfer terms differ from the ideal case of a thin lens in its A and B terms. We therefore simulated our complete setup including the cylindrical lens based on the values given above using the Gaussian analysis tool of the commercial ray tracer ZEMAX. By varying the position of the fiber with respect to the focusing cylindrical lens we plot the position of the beam waist relative to the fiber surface in Fig. 3.9. The beam waist of the focused beam is positioned within the fiber core ($R - r = 58$ µm$< z' < R + r = 67$ µm) for the region marked by the bold line. As can be seen from Fig. 3.9, the required alignment accuracy is only of 40 µm in the y-direction and of 100 µm along the beam propagation axis.

Please note that lenses having a smaller focal lens can also be used for the focusing into the fiber core. However, the requirements on the position accuracy are higher in this case. Furthermore, as spherical aberrations become more important with increasing numerical aperture a corrected cylindrical lens should be used.

Accurate positioning of the modifications into the fiber core

In the previous section, we took into account the fiber curvature in order to find the appropriate lens to induce a refractive index change in the fiber core. However, it is still necessary to find the correct position of the fiber with respect to the focusing lens. The lateral position of the focused laser beam can be centered along the y direction using the deviation of the laser beam through the curved surface. The appropriate distance between the fiber and the focusing lens is found by monitoring the luminescence observed when the focused laser beam
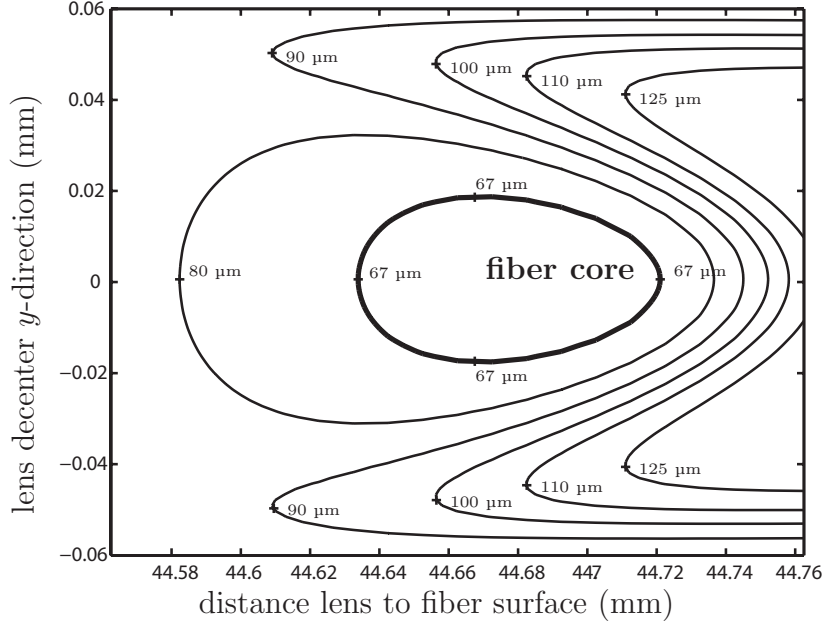
Figure 3.9: The lens position with respect to the fiber determines the beam waist position z' inside the fiber.

reaches the fiber core. That luminescence shows different spectra depending on the fiber core composition as can be seen Fig. 3.10. For standard germanium doped fibers and erbium doped fibers, the luminescence is blue whereas the luminescence for ytterbium doped fibers is yellowish green. Consequently, the luminescence induced in the fiber core is correlated to the multi-photon excitation of different defects present in the fiber core.

In the following experiment the laser beam is focused with a 40 mm cylindrical lens through a germanosilicate single mode fiber for 1550 nm (J-fiber IG 09/125/250, 9 µm core diameter, 125 µm cladding diameter) with a pulse energy of 100 mW and a pulse duration of 50 fs. For that intensity the refractive index change is negligible as will be seen later in Sec. 3.3.2. Figure 3.11 shows the luminescence spectra measured on the side of the fiber with a spectrometer (Ocean optics, USB2000) for different positions of the laser focus inside the fiber. The initial detector and fiber positions were optimized to obtain a maximum signal around 400 nm according to Fig. 3.10. The distance between the fiber and the focusing lens was then varied and the luminescence around 400 nm changed accordingly.

This measurement proves that the luminescence emitted from the fiber core can be used to precisely position the modifications into the fiber core. Furthermore, high reflective FBGs can be written using the position corresponding to the maximum luminescence as will be shown later.
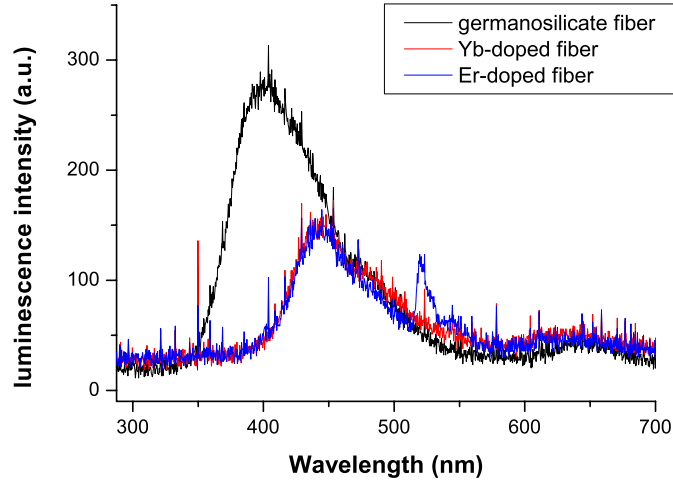
Figure 3.10: Luminescence spectra for an erbium, ytterbium and standard germanosilicate fiber. The luminescence spectra were measured at the fiber side.
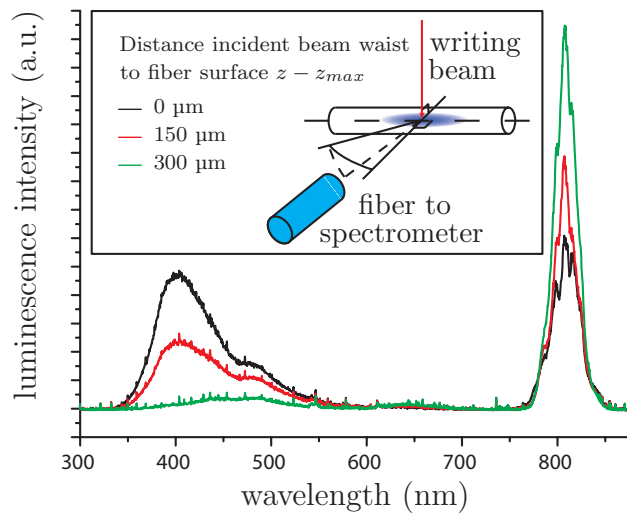
Figure 3.11: Schematic setup and spectra of fs-pulse induced luminescence (z_{max} corresponds to the incident beam waist position of the strongest 400 nm signal).

As we have seen here, the inscription of FBGs using femtosecond pulses requires a tight focusing in order to be able to overcome the fiber curvature and thus reach the fiber core. A precise positioning of the laser beam is also necessary and is achieved by monitoring the luminescence induced by the non-linear absorption of the defects present in the fiber core.

For the phase mask technique, a cylindrical lens must be used to focus the beams diffracted by the phase mask. Thus, a possible astigmatism of the focused laser beam is avoided. Furthermore, the requirements on the positioning accuracy are lowered by using a lens for which the minimum position of the focused beam waist corresponds to the fiber core.

For the point by point technique, the laser beam must be strongly focused in order to minimize the grating period and the overlap of the individual modifications. The influence of the fiber curvature must also be canceled in order to avoid beam astigmatism by using lenses with high numerical aperture like aberration corrected microscope objectives. A diffractive optical element can also be used to compensate the fiber curvature and allow to cover the whole fiber core cross-section by shaping the beam. Due to the extremely small spot size, the requirements on the positioning accuracy are of the order of the fiber core radius and even smaller.

Even though the point by point technique is the most flexible method for the FBG inscription with ultrashort pulses, the grating quality is depending strongly on the accuracy of the positioning system and its ability to reach the grating period. However, by translating the fiber with a constant velocity, the requirements on the positioning system accuracy can be lowered and the grating pitch is defined by the ratio between the writing velocity and the laser repetition rate [63, 71, 72].

Using a phase mask technique allows to easily meet the requirements on the grating period with high precision and reproducibility. Therefore, the approach based on the phase mask technique has been pursued within this thesis. The next section describes the equipment and methods used during the inscription of the FBGs with a phase mask technique.

3.3. Experimental setups and methods for the inscription of the FBGs

In this section, the laser system and the inscription setup are described with more details. During the grating inscription, the transmission and reflection spectra are also measured and will be used in Chapter 4 for the characterization of the written FBGs.

3.3.1. Laser system

As the FBGs are written with a phase mask technique, a laser system with a low repetition rate (Spectra Physics, Spitfire) is used in order to avoid heat accumulation (see Sec. 3.1.2). Thus, the refractive index modifications are restricted to the high energy density region and an optimum contrast for the refractive index modulation can be obtained. The detailed setup of the laser system is shown in Fig. 3.12 as well as its main characteristics. The initial pulse energy of 7 nJ delivered by the oscillator is enhanced to 700 µJ using a Chirped Pulse Amplification technique [73]. Such pulse energies are necessary to enable the realization of refractive index modifications with low NA focusing lenses, such as the cylindrical lenses used for the inscription of FBGs with a phase mask technique. In order to avoid the destruction of the optics and the non-linear effects induced by the high intensity of the laser pulses, the pulse duration is increased to a value of 400 ps using a grating based stretcher. The pulse peak intensity has thus been reduced by 4 orders of magnitude. After several round trips in the amplifier, the pulses are recompressed using a grating based compressor compensating for most of the phase changes induced by the grating stretcher and the dispersion of the beam due to passage through the crystal and the Pockels cells. Thus, 50 fs pulses with a pulse energy of 700 µJ and a repetition rate of 1 kHz leave the amplifier system. A beam splitter is placed at the laser output in order to perform a pulse autocorrelation.
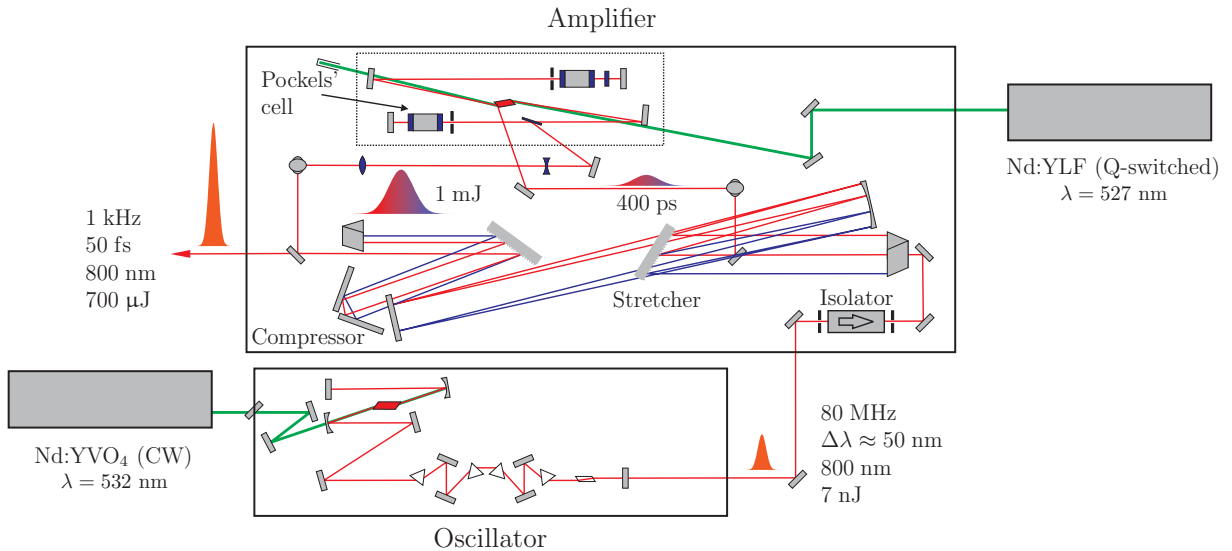
Figure 3.12: Representation of the laser system Spitfire

3.3.2. Inscription setup

The setup used for the inscription of FBGs using the "phase mask" technique is shown Fig. 3.13. The laser beam is focused into the fiber core using a cylindrical lens with a focal
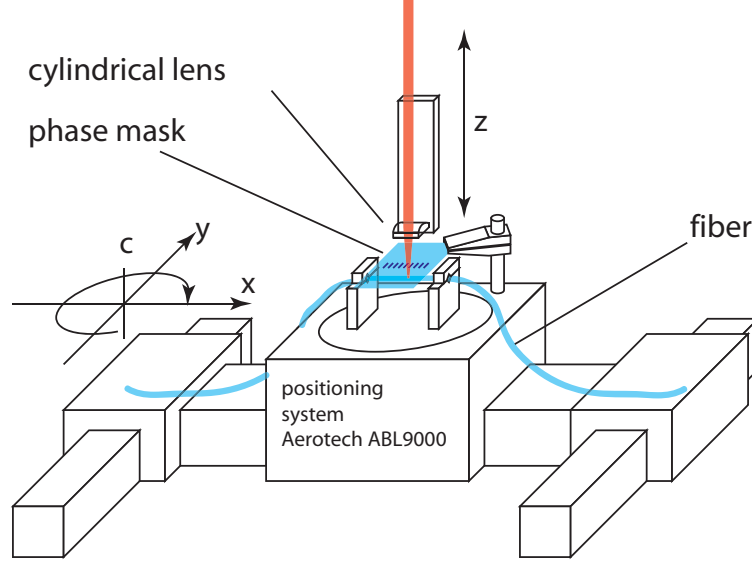

Figure 3.13: The phase mask inscription setup. The phase mask and the dismantled fiber are moved with respect to the focused laser beam with a velocity v.

length of 40 mm as derived in Sec. 3.2.3. Using that lens, the fiber curvature is overcome and the focused laser beam can be positioned into the fiber core. Furthermore, an easier positioning of the modifications into the fiber core, with less requirements on the positioning accuracy can be done as the minimum beam waist position of the focused laser beam corresponds to the fiber core. The interference pattern is produced by the overlap of the +1st and -1st diffraction orders produced by the phase mask. A pure two-beam interference is realized by choosing a distance between the phase mask and the fiber for which the pulses diffracted in the 0th and the $\pm$ 1st diffraction orders are separated by a distance greater than the coherence length of the pulses (see Eq. (3.2)). This distance is depending on the phase mask characteristics described in table 3.2. The accurate positioning into the fiber core is done by monitoring the luminescence (see Sec. 3.2.3) resulting from the non-linear absorption of the defects present in the fiber core. The fiber core is scanned until the maximum luminescence, which corresponds to the fiber core, is obtained. Thereby, a pulse energy below the threshold for permanent refractive index modification (typically 100 µJ) is used so that the grating profile is not perturbed by the scanning of the fiber core.

As the length of the grating is limited by the effective overlap of the diffraction orders (see Sec. 3.2.2, Eq. (3.3)), the length of the written FBG is thus increased by translating the

phase mask and the fiber with respect to the laser beam. This technique is called the "phase mask scanning" technique. This technique has the advantage of enabling the inscription of apodized as well as continuously chirped gratings. The accurate positioning is assured for the starting and end points of the grating to be written and the phase mask as well as the fiber are moved with a constant velocity with respect to the laser beam between those two points. During the grating inscription, the transmission and reflection spectra of the gratings are recorded using two optical spectrum analyzers (HP 86142A) having a resolution of 0.06 nm. The measurement setup can be seen in Fig. 3.14.
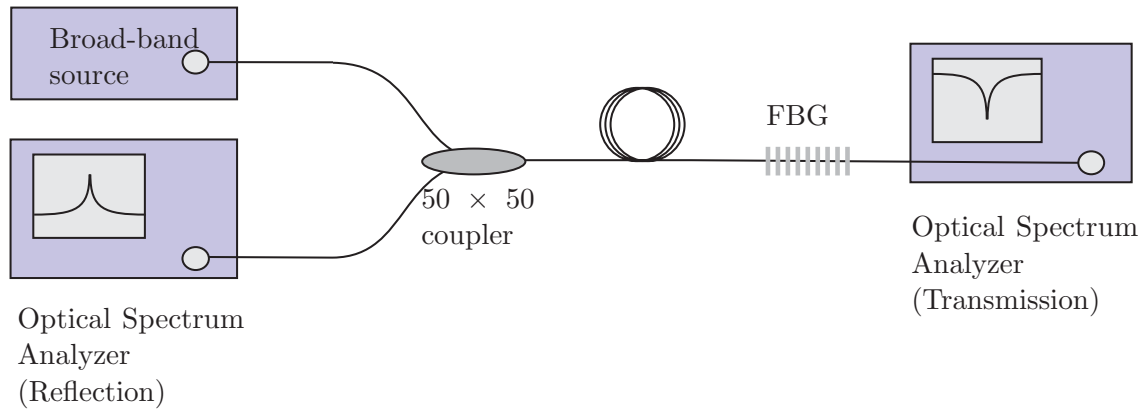
Figure 3.14: Measurement setup for the grating reflection and transmission spectra.

A broad-band source is connected to one arm of a 50×50 coupler. Light passes through the coupler and is coupled into the fiber containing the FBG. The transmission spectrum of the FBG is then collected after the FBG by an Optical Spectrum Analyzer (OSA). Light reflected by the grating passes through the 50×50 coupler once more and is collected at the output of the second arm.

For normalization purposes, reflection and transmission spectra are collected before the grating is inscribed. Therefore, the end of the fiber where the grating will by inscribed is perpendicularly cleaved. Consequently, the initial reflection spectrum is a fraction of the Fresnel reflection at the fiber end facet as losses are present at each connection from one fiber to the other (due to splice losses or butt-coupling with connectors). Light passing through the coupler experiences insertion losses as well.

During grating inscription, the transmission and reflection spectra are recorded and used in the next chapter for diagnostic and characterization purposes. When the grating inscription is finished, the end of the fiber containing the grating is angle cleaved to suppress the Fresnel reflection. The grating reflection spectrum can then be fully characterized.

4. Femtosecond written FBGs in non-photosensitive fibers

The aim of this chapter is to study the characteristics of FBGs written with femtosecond pulses, using the phase mask tecnique, into standard non-photosensitive single mode fibers. In contrast to conventional UV techniques, the refractive index modifications are restricted to the focal region of the focused laser beam and therefore do not necessarily extend over the whole fiber core. For this reason, the size of the induced modifications as well as their impact on the grating response will be studied first. In the second section, the characteristics of first order static FBGs, whose fiber position is not varied during the grating inscription, are studied. This is typically the standard configuration for the inscription of UV gratings and will allow us to compare the growth behavior and the quality of the written gratings. This will also give us an initial indication on the inscription parameters as well as on the achievable grating bandwidths. In the third section, the FBGs will be written preferentially using a phase mask scanning technique. Using that technique, the grating length is increased by translating the phase mask and the fiber under the inscription laser beam. This allows a greater control of the grating bandwidth and reflectivity. After a short discussion of the characteristics of the first order FBGs written by phase mask scanning, the FBGs will be preferably written in the second order in order to enable the inscription of FBGs for fiber laser applications at 1.04 µm and 1.55 µm (see next chapter). The influence of the writing parameters will be studied with more details at a Bragg wavelength of 1.55 µm in order to find the optimum writing parameters. In the last section, a study of the FBGs' temperature sustainability will give us informations about the type of modifications induced (type I or type II similar to conventional UV inscribed FBGs).

4.1. General characteristics of the written FBGs

In this section and in the following, FBGs are written in a standard single mode fiber (J-fiber IG09/125/250) designed for 1.55 µm using the phase mask technique. The characteristics of the phase masks used are detailed in Table 3.2. The refractive index change is induced by the non-linear absorption (see Sec. 3.1.2) of the focused laser beam. As a low repetition

rate laser system (Sec. 3.3.1) is used, no heat accumulation occurs (see Sec. 3.1.2) and the modifications are restricted to the focal volume. The cylindrical lens used for the focusing of the laser beam has a short focal length in order to overcome the fiber curvature and to enable the fiber core to be reached (see Sec. 3.2.3). Thus, the induced modifications do not necessarily cover the whole fiber core. Therefore, the size of the induced refractive index modification as well as its impact on the grating characteristics are studied.

The modifications are written into the fiber as previously described in Sec. 3.3.2. The laser beam is focused by a 40 mm cylindrical lens in order to enable an easier positioning of the modifications into the fiber core, with less requirements on the positioning accuracy. The luminescence induced by the non-linear aborption of the defects present in the fiber core is used to precisely position the modifications in the fiber core. The fiber is translated with respect to the fiber axis in order to increase the length of observable modification under the microscope. The fiber can thus be cut and polished to obtain pictures of the fiber cross-section of good quality.

Figure 4.1 shows a picture of the cross-section of a refractive index modification written with a translation velocity of 10 mm/min and a pulse energy of 300 µJ. The picture was taken with a polarization microscope. The modifications can also be observed with a dark field microscope but better contrast is obtained with the polarization microscope. The probe has a length of about 100 µm.

The modifications have a width of about 2 µm and a depth of about 50 µm. Using Gaussian optics and the ABCD law (Eq. (3.5)), the depth of the modification is evaluated to 137.5 µm and corresponds to the Rayleigh length of the focused beam. The width of the modification is given by the diameter of the focused beam and is evaluated to 5.9 µm. The calculations were made assuming an initial Rayleigh length of 100 µm resulting from the focusing of the laser beam with a beam radius of 2.4 mm with the 40 mm cylindrical lens. The discrepancy between the size of the refractive index change and the theoretical focal volume dimensions is due to the non-linear absorption process and the existence of an energy threshold for the generation of a permanent refractive index modification.

The picture of Fig. 4.1 was taken with a polarization microscope with crossed polarizer and analyzer. As the modification is still visible and not extinguished, an unquantifiable degree of birefringence has been induced during the writing process. The observed birefringence can possibly be attributed to stress induced in the fiber [74] or to the presence of nanogratings [62] (see Sec. 3.1.2).

As the refractive index modification is not covering the whole fiber core, only effective values for the refractive index modulation can be calculated and the coupling constant κ_{ac} will be preferably used to quantify the strength of the coupling to the back-propagating mode.
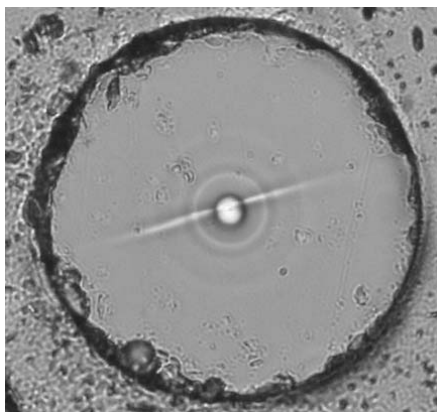
Figure 4.1: Picture taken with a polarization microscope of a modification written with 300 µJ and a translation velocity of 10 mm/min.

Moreover, the strong asymmetry of the refractive index change results in a position dependent value of the overlap integral between the grating transverse profile and the interacting modes. The coupling to a particular cladding mode, for example, can be favored by optimizing the overlap of the grating transverse profile with that cladding mode.

4.2. First order static FBGs

The inscription of the FBGs with femtosecond pulses is first studied using a first order phase mask with a period of 1.075 µm, optimized for the inscription wavelength of 800 nm. The FBGs are written without moving the phase mask and the fiber during the laser exposure, which corresponds to the conditions usually used for the inscription of standard FBGs. The characteristics of the written gratings are studied and compared with standard UV written FBGs. The study of the grating growth gives an indication about the optimum inscription parameters and the transmission and reflection spectra about the quality of the written gratings.

4.2.1. Grating growth

In order to study the influence of the pulse energy on the grating growth, different gratings were written with a phase mask having a period of 1.075 µm. The distance between the focusing lens and the fiber was set to 1.3 mm. At that distance, a pure two-beam interference as well as a good overlap of the $\pm$ 1st diffraction orders is obtained (see Sec. 3.2.2) and the destruction of the phase mask due to the high energy densities used is minimized. The grating

transmission as a function of irradiation time (i.e. number of laser shots) was monitored and the graph in Fig. 4.2 shows the evolution of the Bragg wavelength as well as the transmission at the Bragg wavelength as a function of the number of pulses. For this measurement the laser repetition rate was reduced to 200 Hz which allowed a greater number of OSA scans to be collected. Two different regimes have been observed while inscribing first order FBGs :

- for $E \leq 410$ µJ (Fig. 4.2 a), the transmission depth of the grating at the Bragg wavelength saturates and the Bragg wavelength increases with the number of pulses, revealing the inscription of a positive refractive index change;

- for $E \geq 410$ µJ (Fig. 4.2 b), the transmission depth of the grating at the Bragg wavelength decreases after having reached its maximum depth. This corresponds to a grating erasure which can be due to the saturation of the refractive index profile as was first assumed by Xie *et al.* [12]. However, the slow grating regrowth rather reveals the inscription of a type IIA grating (see Sec. 3.1.1). The Bragg wavelength nevertheless continued to increase with the number of pulses, which is uncharacteristic for type IIA gratings written with UV radiation [41]. In type IIA UV written gratings the grating saturation and regrowth is attributed to the formation of a negative refractive index modification which results in a decrease or stabilization of the Bragg wavelength. In our case, the Bragg wavelength is still increasing during the formation of the type IIA grating. This can possibly be explained by the fact that ~ 20 % of the diffracted energy were contained in the 0th diffraction order of the phase mask. This could possibly result in an overall increase of refractive index and mask a decrease of the Bragg wavelength attributed to the formation of a negative refractive index modification. This hypothesis can be inferred by the study made by Sudrie *et al.* on the thresholds for type I and type II modifications [61] in fused silica. They observed a reduction of the thresholds when the beam was translated several times over the same region, passing over a pre-treated region or by reducing the translation velocity, exposing a region for longer time. It was also observed in phosphate glass that the refractive index change became negative after 7 passes over the same region [75]. Thus, a transition between type I and type II modifications can possibly occur for long expositions of the probe at a constant energy. In order to to avoid the grating erasure and to maximize the grating reflection, the exposure of the grating should not exceed 60 000 pulses.

Considering both regimes, the grating begins to saturate in a range between 6 000 and 40 000 pulses, depending on the inscription pulse energy, and should lead to the appearance of the second order Bragg wavelength [12]. Due to the saturation of the grating profile, higher Fourier components appear (see Eq. (2.29) in Sec. 2.2.2) which lead to Bragg reflection
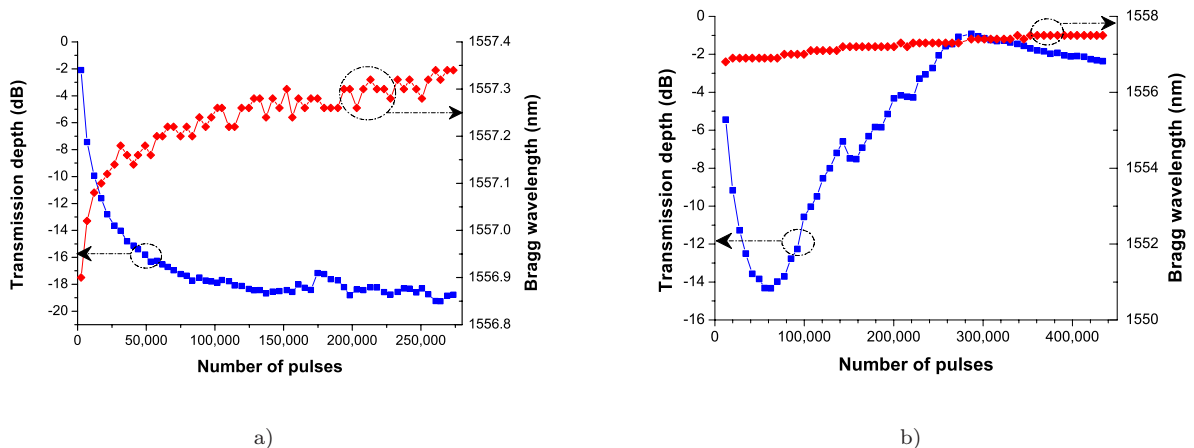
Figure 4.2: Evolution of the grating transmission depth (black squares) and Bragg wavelength (red diamonds) with the number of incident pulses for (a) a pulse energy of 260 µJ and (b) a pulse energy of 410 µJ.

at wavelengths inversely proportional to the initial Bragg wavelength (see Eq. (2.40) with $n_{\text{eff}_\mu} = n_{\text{eff}_\nu}$). However, as the fiber used for the FBG inscription was not guiding at 780 nm, we could not measure the growth of the second order Bragg grating.
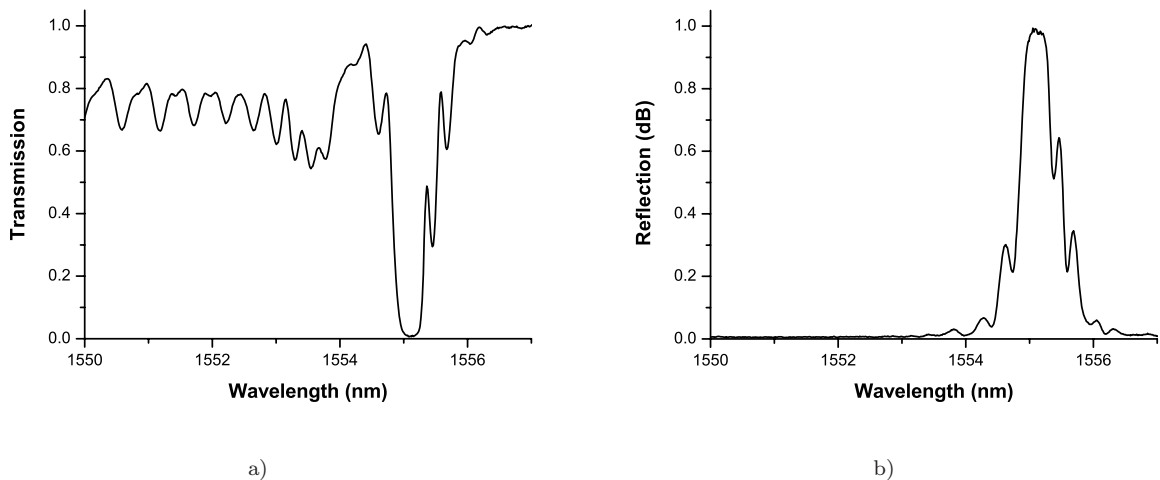
4.2.2. Typical transmission and reflection spectra

As already discussed in Sec. 4.1, the refractive index change is not covering the whole fiber core, which has an influence on the coupling to the cladding modes. Figure 4.3 shows the transmission and reflection spectra of a static first order FBG written with a pulse energy of 410 µJ. Below the Bragg wavelength the transmission spectrum (Fig. 4.3 a) exhibits discrete losses which are due to the coupling of the core mode into back-propagating cladding modes (Sec. 2.3.4). Even for conventional UV gratings, the refractive index modulation is non-uniform across the fiber core as the inscription beam is partly absorbed while propagating through the fiber core and therefore the overlap of the cladding modes with azimuthal order $l > 1$ with the fundamental core mode is non-null [17]. As the refractive index modulation has a strong asymmetric morphology in our case (see Sec. 4.1), the overlap integral between the core mode, the higher order cladding modes and the grating profile is significant and more resonances are visible than for UV written gratings. The cladding modes disappear when they propagate from the uncoated FBG region into a region of fiber still coated which has a refractive index higher than the cladding, and thus the cladding modes are not guided any more. Therefore, cladding mode coupling has no influence on the grating reflectivity (see Fig. 4.3 b) and the FBG can be used as a resonator mirror in fiber laser applications. However,

for telecommunication applications where the grating is used in transmission, the cladding mode coupling induces some unwanted extra losses deteriorating grating quality. For such applications, the cladding mode coupling can be canceled by writing the modifications across the whole fiber core and the immediate surroundings [76]. Since the refractive index change is homogeneously distributed over the whole transverse electric field of the fundamental mode, the orthogonality relation implies a zero overlap integral between the orthogonal core and cladding modes [77].

Furthermore, the reflection spectrum of the grating reveals the presence of side lobes and is thus quite similar to the theoretical reflection spectra calculated in Sec. 2.3.2 for uniform gratings. The refractive index profile of the FBG can thus be considered in a first approximation to be uniform over the grating length. Since the refractive index modification results from a non-linear absorption process, the absorbed intensity is proportional to a supergaussian. On the steep sides of the supergaussian profile, the intensity is not high enough to overcome the threshold for permanent refractive index modification and the grating profile can be approximated by a flat top distribution.

Figure 4.3: Typical normalized transmission a) and reflection b) normalized spectra for a static grating written with a pulse energy of 410 µJ in the first order.

4.2.3. Influence of the pulse energy on the grating reflectivity and bandwidth

Table 4.1 gives the minimum transmission and the equivalent grating reflection at the Bragg wavelength as well as the Full Width Half Maximum (FWHM) bandwidth and the grating efficiency $\kappa_{ac}L$ measured for FBGs written with different pulse energies after their saturation.

The grating efficiency was evaluated using Eq. (2.53) and reads as

$$\kappa_{ac}L = \tanh^{-1}\sqrt{r_{max}}. \tag{4.1}$$

pulse energy (μJ)	transmission (dB)	reflectivity (%)	bandwidth (nm)	$\kappa_{ac}L$
150	-13.2	95.2	0.285	2.2
250	-19.75	98.9	0.165	2.96
410	-21.73	99.3	0.17	3.19

Table 4.1: Characteristics of the first order static gratings (transmission depth, reflectivity, FWHM bandwidth and grating efficiency) for different pulse energies. The efficiency of the grating $\kappa_{ac}L$ is calculated from the grating reflectivity using Eq. (4.1).

As can be seen in table 4.1, the grating reflectivity is increasing with the pulse energy whereas the bandwidth decreases. Furthermore, as $\kappa_{ac}L \leq \pi$, the gratings are in a regime between the length limited and the bandwidth limited regime (see Sec. 2.3.3). Thus, both the refractive index modulation and the grating length have an influence on the bandwidth of the grating.

For applications where a smaller bandwidth or a higher reflectivity is required, the length of the FBG has to be increased. This can be achieved by translating the phase mask and the fiber under the inscription laser beam as explained in Sec. 3.3.2. This method is called the "phase mask scanning" technique. Because it allows a greater flexibility in the grating design (e.g. chirped and apodized gratings can be realized), this method will be used in the following sections.
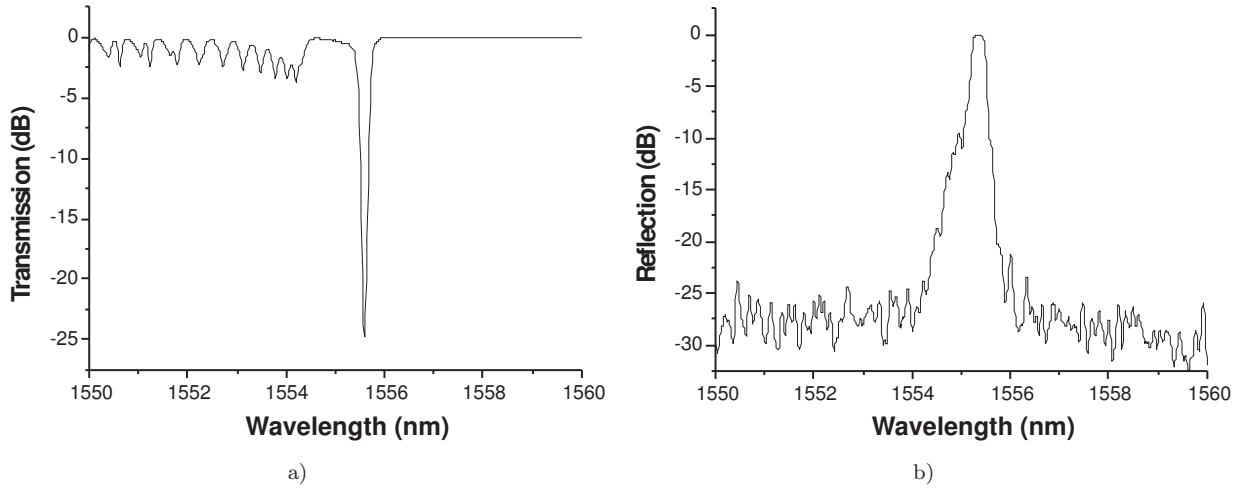
4.3. FBGs written by phase mask scanning

Increasing the length of the FBG offers the possibility to increase the grating reflectivity and to narrow the bandwidth of the grating. However, since no phase masks can be designed in the first order for $\lambda_B \leq 1.04$ μm (see Sec. 3.2.2) for our inscription wavelength ($\lambda = 800$ nm), second order phase masks should be used. In the following, we demonstrate that the inscription of FBGs with a Bragg wavelength of 1.55 μm can be done with both first order and second order phase masks with comparable quality. The characteristics of the FBGs will be studied for a Bragg wavelength of 1.55 μm in order to find the optimum writing parameters. We will show in Sec. 5.2 that those parameters can be used for the inscription of FBGs having a Bragg wavelength around 1.04 μm.

4.3.1. Comparison first order - second order phase mask scanning

In this section, we demonstrate that FBGs can be written in the first and second order by phase mask scanning for a Bragg wavelength around 1.55 µm and that the quality of the written FBGs is comparable.

Figure 4.4 shows the transmission and reflection spectra of a first order grating written with a pulse energy of 400 µJ. The fiber and the phase mask were translated with a velocity of 5 mm/min under the laser beam over a distance of 40 mm, which is limited by the length of the phase mask used. The distance between the phase mask and the fiber was of 1.3 mm as previously used for the inscription of the first order static FBGs. The transmission and reflection spectra are represented in logarithmic scale in order to see the grating efficiency in transmission and the side lobes in reflection with more precision. For clarity, the transmission in dB is defined as $T_{dB} = 10 \log T_{lin}$, where T_{dB} is the transmission in dB and T_{lin} is the linear transmission coefficient. The reflection in dB is defined using the same definition.

Figure 4.4: Transmission (a) and reflection (b) spectra of a first order grating written with the phase mask scanning technique. The FBG was written with 400 µJ pulse energy and a scanning velocity of 5 mm/min.

The grating has a transmission depth of 24.8 dB, which is higher than the 20 dB achieved in the previous section by static gratings. This corresponds to a reflectivity of 99.66 %. Thus, an increase of the grating reflectivity was observed as expected. The FWHM bandwidth is evaluated to ∼ 0.14 nm. The bandwidth is thus smaller than the bandwidth of the static gratings, which is due to the larger grating length. In comparison with the static grating, losses due to the cladding mode coupling are more significant when the scanning technique is used (2.5 dB versus 1.5 dB) as the interaction length is increased.

However, the reflection spectrum of the scanned grating differs slightly from the reflection

spectra of the static grating. The reflection peak is asymmetric and the expected side lobes are replaced by finer structures. This can be explained by small variations of the phase mask period or diffraction efficiency.

Variations of the diffraction efficiency are attributed to changes in the depth or width of the grating grooves and can induce some variations in the refractive index modulation and average refractive index change. The variations of the average refractive index change are responsible for the apparition of secondary reflection peaks, which can induce an asymmetry in the shape of the reflection peak.

Phase errors are the result of the positioning errors during the fabrication of the phase masks using electron beam lithography. For example, as the size of the fields which are exposed to the electron beam is limited, the substrate containing the phase mask has to be moved to write the next field. Thus, some phase errors induced by the positioning system appear at each field boundary [78]. These errors are called "stitching errors" and induce some parasitic reflection peaks, which are easily recognizable as they are periodically distributed outside of the main reflection peak. Such periodical parasitic peaks could not be observed, which let us suppose that the stitching errors have a negligible impact on the grating quality. Smaller inaccuracies in the grating period statistically distributed over the whole phase mask length are attributed to the resolution in the positioning of the electron beam (≤ 2.5 nm). This can possibly result in the apparition of parasitic reflection peaks within the Bragg reflection. However, as the errors in the grating period are statistically distributed over the whole grating length, the parasitic peaks are difficult to identify clearly as their impact might be limited. Variations of the average refractive index as well as local changes in the period can induce an asymmetric main reflection peak due to the apparition of parasitic reflection peaks. It is however difficult to predict from the reflection spectra which of these effects is predominant.

In order to compare the properties of the written gratings, a second order FBG was written by phase mask scanning with the same pulse energy and velocity. The phase mask used has a period of 2.15 µm, which is twice the period of the phase mask used for the first order FBG inscription. Because of the larger phase mask period, the diffraction efficiency could be reduced to a few percents. The grating was written in the same fiber as previously (J-fiber IG09/125/250). The distance between the phase mask and the fiber was of 1.5 mm. At that distance, the focal spots of the 0th and 1st order are separated by 115 µm. Thus, even if a pulse distortion attributed to self phase modulation or dispersion occurs, the 0th and 1st diffraction orders should not interfere.

Figure 4.5 shows the transmission and reflection spectra of a second order FBG written using the phase mask scanning technique with a pulse energy of 400 µJ and a scanning

velocity of 5 mm/min. The grating has a transmission loss of 24.7 dB, which corresponds to a reflectivity of 99.65 %. The reflectivity is the same as achieved by the first order FBG written by phase mask scanning. Thus, efficient FBGs can be written in the first and second order with comparable performances. The good performance of the second order grating is enhanced by the better overlap of the +1st and -1st order, due to the smaller diffraction angle. The effective overlap length was evaluated using Eq. (3.2) to 3.6 mm versus 1.9 mm in the first order. Furthermore, the FWHM bandwidth of the FBG is smaller than the resolution of the OSA. Therefore, FBGs with narrow bandwidth can be written with second order FBGs. The grating has, however, a larger reflection peak than the first order FBG in the logarithmic scale. Thus, the irregularities in the refractive index profile have a higher impact for the second order grating. This is probably due to the longer effective overlap length or to the increased sensitivity due to the use of the second order Fourier component of the refractive index profile. However, the reflection on the sides of the reflection peak is negligible as it represents less than a few percents of the Bragg reflection peak. Furthermore, in comparison with first order FBGs written with the phase mask scanning technique, the coupling to the cladding modes is higher (5 dB losses versus 2.5 dB in the first order). However, the efficiency of the FBG at the Bragg wavelength is comparable. Thus, the different strength of the cladding mode coupling is probably due a different overlap of the grating with the cladding modes.

a)   b)
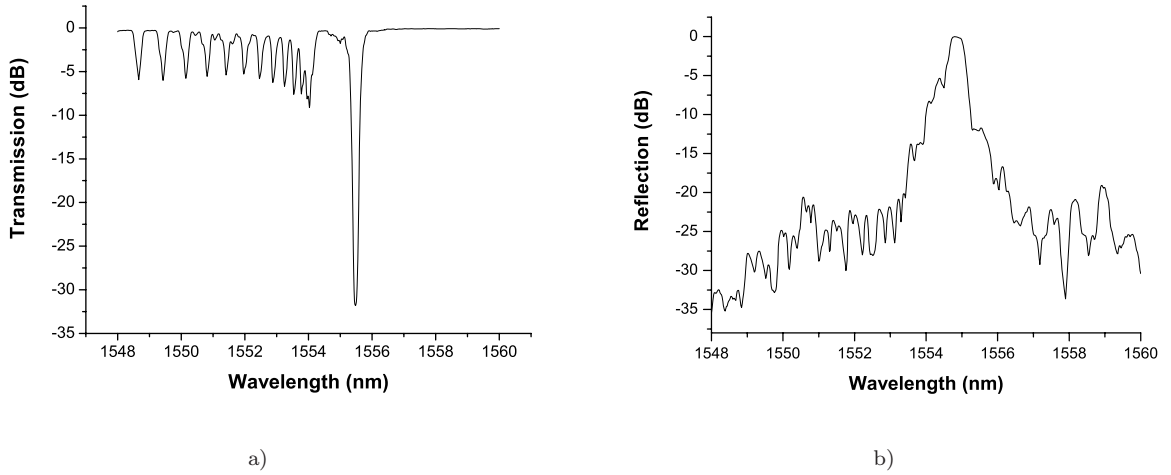
Figure 4.5: Typical transmission a) and reflection b) normalized spectra of a grating written with the phase mask scanning technique. The FBG was written in the second order with a pulse energy of 400 µJ and a writing velocity of 5 mm/min. The FBG was 40 mm long.

Thus, second order phase mask scanning can be used for the inscription of long FBGs with comparable reflectivities and narrower FWHM bandwidths than the first order FBGs written by phase mask scanning.

a)   b)
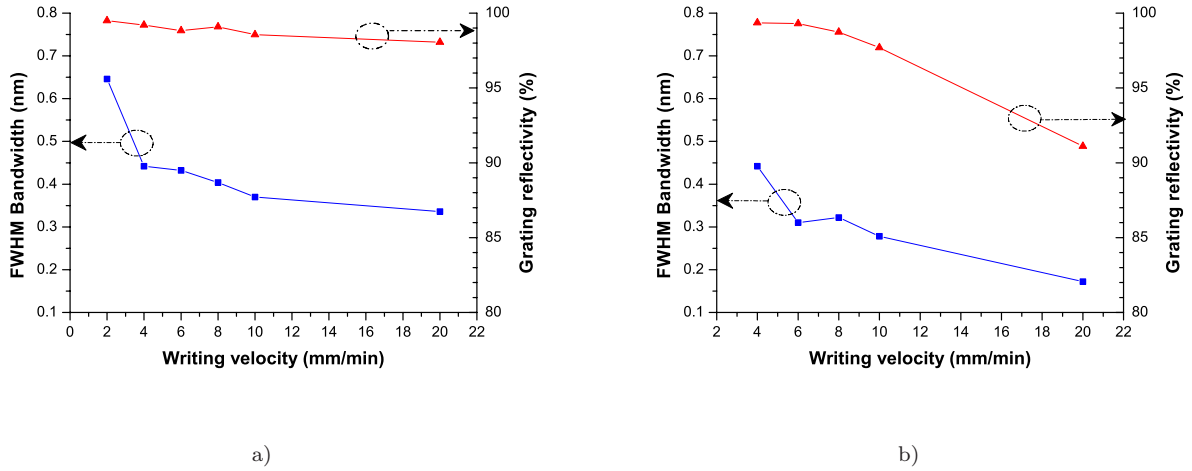
Figure 4.6: Evolution of the FWHM bandwidth (squares) as well as the grating reflectivity (triangles) versus writing velocity for (a) a pulse energy of 400 µJ and (b) a pulse energy of 600 µJ.

In the next section, the influence of the writing parameters like pulse energy and scanning velocity on the grating characteristics will also be studied and the optimum parameters for the grating inscription will be discussed.

4.3.2. Influence of the writing parameters

In order to study the influence of the writing parameters on the grating response, different gratings were written with various pulse energies and translation velocities. The gratings had a length of 40 mm and were written with a constant phase mask/fiber distance of 1.5 mm, as in the previous experiment. The influence of the pulse energy and the writing velocity on the grating reflectivity, bandwidth, Bragg wavelength and coupling constant is studied.

Evolution of the reflectivity and bandwidth

Figure 4.6 shows the evolution of the grating reflectivity as well as the Full Width at Half Maximum (FWHM) bandwidth as a function of the writing velocity for two different pulse energies (400 µJ and 600 µJ). The grating length was 40 mm and the writing velocity was varied from 20 to 2 mm/min, meaning 2 to 20 min to inscribe a 40 mm long grating. The FWHM bandwidth range from 0.2 to 0.7 nm with reflectivities greater than 90 % depending on the pulse energy and on the writing velocity.

As can be seen from the graph, translation velocities ranging from 2 to 20 mm/min can be used for the inscription of second order FBGs using a phase mask scanning technique.

This has to be compared with the values obtained from the saturation of the refractive index profile in first order static gratings (see Sec. 4.2.1). The number of pulses N, hitting the same place while the laser beam is scanned with the velocity v along the fiber can be deduced from the time taken by the beam to translate along its whole length. For a first approximation, the size of the modifications along the fiber axis is given by the effective overlap length L_{overlap} (Eq. (3.3)) resulting from the overlap of the +1st and -1st diffraction order of the focused laser beam. By introducing the repetition rate of the laser in that relation, we get the number of pulses N hitting a particular point as :

$$N = L_{\text{overlap}}/v \times f_R \qquad (4.2)$$

where f_R is the repetition rate of the laser. Using this relation, by translating the fiber with velocities ranging from 2 to 20 mm/min, circa 0.77 to $7.75 \cdot 10^4$ pulses hit the same place which corresponds to the interval given by the begin of the saturation and the erasure of the gratings evaluated in Sec. 4.2.1 in the case of first order static gratings.

The fact that FBGs can be written in the second order before the full saturation of the grating was explained by a model developed by Smelser *et al.*, where they simulated the saturation of the grating refractive index profile [79] for hydrogenated germanosilicate fibers. A measurement has shown that the refractive index modulation Δn_m scales with E^5, which is the deposited energy [80]. Thus, the refractive index change can be attributed to the non-linear absorption of 5 photons for IR fs pulses, which is consistent with the energy bandgap of germanium doped silica (E_g = 7.75 eV [81]). Therefore, the grating refractive index profile was assumed to be proportional to a I^5 intensity profile. Using a particular saturation function, the evolution of the higher order coupling constant was predicted by developing the saturated profile into its different Fourier terms and explained the formation of a second order grating before full saturation of the refractive index.

By decreasing the writing velocity from 20 to 2 mm/min the FWHM bandwidth as well as the grating reflectivity increased. Thus, the induced refractive index modulation increases with slower translation speeds. A similar evolution of the induced refractive index in function of the writing velocity has been observed during the inscription of optical waveguides [82]. Furthermore, an increase of the pulse energy does not lead to an increase of the grating reflectivity and of the refractive index modulation. As the written FBGs are of second order, the second Fourier term of the refractive index profile is responsible for the reflectivity at the considered wavelength. Thus, the second Fourier term is not linearly dependent of the pulse energy and is rather dependent on the evolution of the shape of the saturated refractive index profile.

The same measurement was also made with a pulse energy of 200 µJ (Fig. 4.7) but the reflectivity and FWHM bandwidth did not show any similar evolution. This is probably due to the fact that this pulse energy is near the threshold for refractive index modifications and thus more sensitive to variations in the diffraction efficiency of the phase mask.
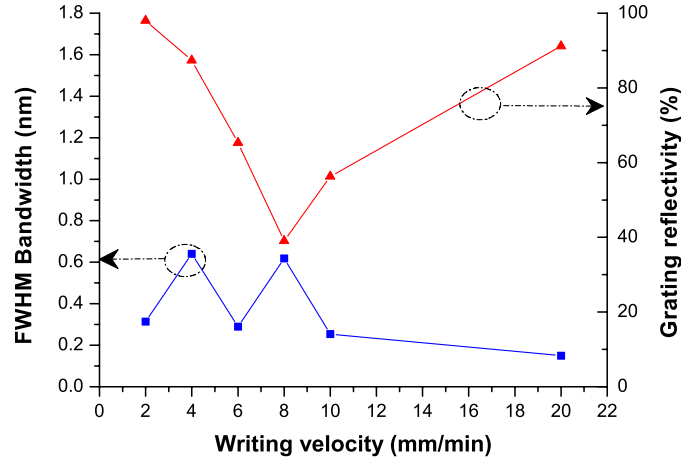
Figure 4.7: Evolution of the FWHM bandwidth (squares) and grating reflectivity (triangles) versus writing velocity for a pulse energy of 200 µJ.
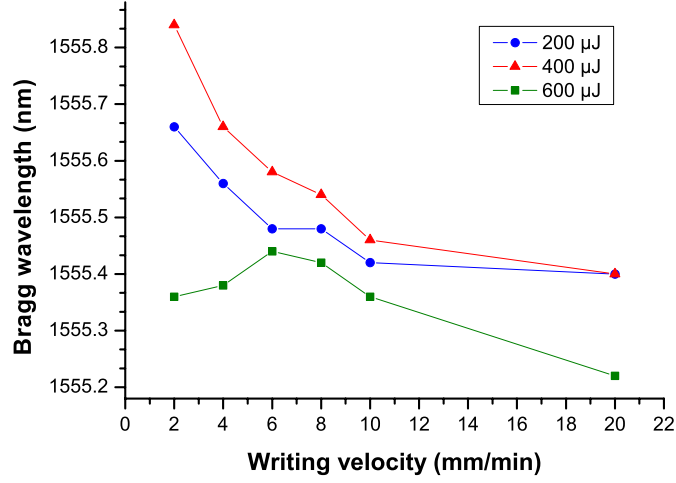
Evolution of the Bragg wavelength

The evolution of the Bragg wavelength depends on the pulse energy and on the writing velocity as shown Fig. 4.3.2 and gives some indication on the evolution of the average refractive index change. As was the case for the reflectivity, the Bragg wavelength increases as the scanning velocity is reduced. This is the result of a longer exposure and hence a greater refractive index change. Increasing the pulse energy from 200 µJ to 400 µJ also leads to an increase of the Bragg wavelength. However, for a pulse energy of 600 µJ, the Bragg wavelength is lowered. A possible explanation is that the higher pulse energy is sufficient to induce a type II modification (see Sec. 3.1.2) which is responsible for a negative refractive index change leading to a smaller Bragg wavelength.

Evolution of the coupling constant

As developed in Sec. 4.2.3, the grating reflectivity depends on the value of the product $\kappa_{ac}L$ according to Eq. (4.1). Thus, the grating strength can be easily defined with the value of

Figure 4.8: Evolution of the Bragg wavelength for 40 mm long gratings written with pulse energies of 200, 400 and 600 µJ. The writing velocities were between 2 and 20 mm/min.

κ_{ac} independently of the size of the modifications. This is useful for the femtosecond written FBGs as the size of the modifications can vary depending on the writing parameters and is not easy to determine with high accuracy (see Sec. 4.1).

As formerly explained in Sec. 3.3, the grating reflection is measured from the normalized transmission spectra. Thus, by monitoring the grating transmission during grating inscription, the evolution of the reflectivity as a function of grating length can be measured. Using Eq. (2.53), the grating efficiency $\kappa_{ac}L$ can be deduced from

$$\kappa_{ac}L = \tanh^{-1}\sqrt{1 - T_{min}}, \tag{4.3}$$

where T_{min} is the minimum transmission at the Bragg wavelength, where we assume that no additional coupling occurs at the Bragg wavelength. The value of κ_{ac} can then be deduced from the slope of $\kappa_{ac}L$ versus grating length L.

Figure 4.9 shows the evolution of $\kappa_{ac}L$ with the grating length for a FBG written with a pulse energy of 600 µJ and a writing velocity of 4 mm/min. The coupling constant was evaluated to $\kappa_{ac} = 0.23$ mm^{-1} by linearly fitting the curve for $0 < L < 13$ mm. For greater grating lengths, the reflectivity of the grating as well as the $\kappa_{ac}L$ product saturate for grating lengths greater than 20 mm.

This saturation can be attributed to scattering losses or to the accumulation of the errors attributed to the phase mask. In order to identify the contribution of the scattering losses, the evolution of the transmission losses for wavelengths above the Bragg wavelength ($1561 < \lambda < 1563$ nm) has been measured as a function of the inscribed grating length (Fig. 4.10).
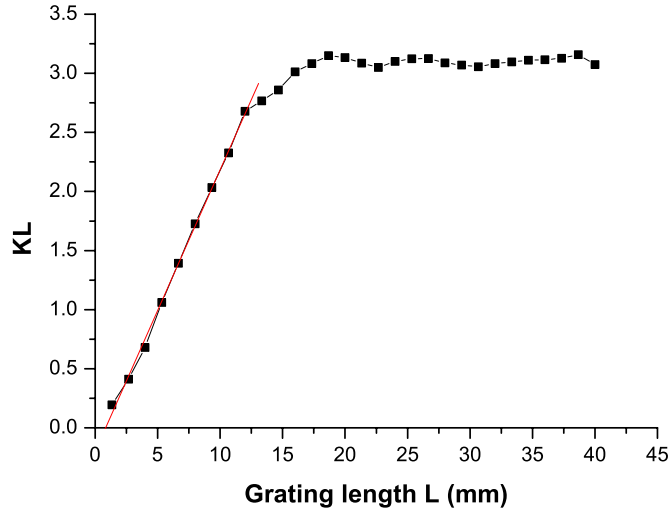
Figure 4.9: Evolution of the grating efficiency versus grating length for a grating written with a pulse energy of 600 µJ and a scanning velocity of 4 mm/min.

The transmission losses outside of the coupling range saturate after a length of 16 mm and thus follow the same evolution than the grating strength $\kappa_{ac}L$. Thus, the saturation of the coupling constant κ_{ac} cannot be attributed to scattering losses, which would have a constant contribution over the grating length. The saturation of the grating strength is thus resulting from the accumulation of the local variations in the grating refractive index profile. These local variations of the refractive index profile are the result of the phase mask irregularities.

By plotting $\kappa_{ac}L$ with respect to the grating length, the coupling constant can be accurately measured before saturation and takes into account the real grating strength. Figure 4.11 shows the evolution of the coupling constant measured for different pulse energies (200 µJ, 400 µJ and 600 µJ) and for writing velocities varying from 20 to 2 mm/min.

Despite some experimental fluctuations, the dependence of the coupling constant on the writing velocity can be predicted for pulse energies of 400 µJ and 600 µJ as the coupling constant varies monotonically with the writing velocity.

For a pulse energy of 600 µJ, the Bragg wavelength is lower than for a pulse energy of 400 µJ. However, as the coupling constant is comparable for translation velocities between 2 and 10 mm/min, the shorter Bragg wavelength does not result from a possible phase mask destruction and can be attributed to a type II modification. The lower coupling constant measured for a velocity of 20 mm/min is attributed to a cumulative effect, where the type I and type II modifications coexist, reducing the refractive index modulation. Thus, writing FBGs with a pulse energy of 600 µJ should lead to the inscription of a type II modification
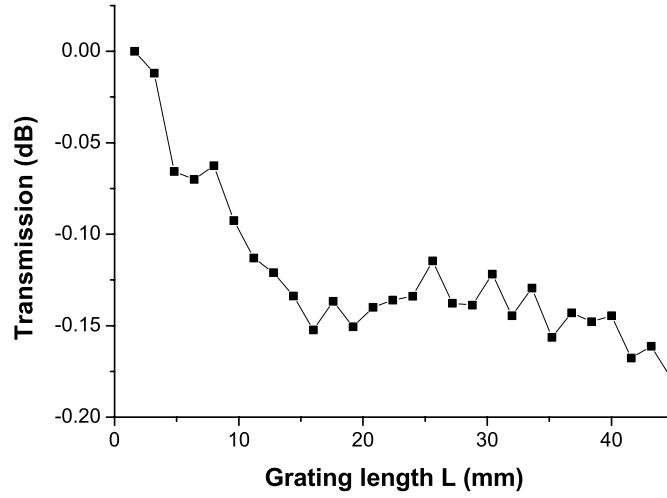
Figure 4.10: Transmission measured outside of the coupling (for $1561 < \lambda < 1563$ nm) for the previous FBG written with a pulse energy of 600 µJ and a scanning velocity of 4 mm/min.

and to a better temperature stability.

For a pulse energy of 400 µJ, the coupling constant varies accordingly with the Bragg wavelength, which is the higher measured in our experiments. This is typical for type I modifications.

For the pulse energy of 200 µJ, the coupling constant is not monolithically varying with the writing velocity.

The data collected on the coupling constant and the Bragg wavelength allows to write FBGs with specific Bragg wavelength and reflectivity. A pulse energy of 400 µJ can be used as the coupling constants and the Bragg wavelength increase monolithically and can be predicted for other scanning velocities depending on the design requirements.

As the effective index of the fundamental core mode at 1.55 µm of our fiber was not known with enough accuracy, the average induced refractive index change $(\Delta n_0)_{\text{eff}}$ could not be estimated. Thus, the pulse energy and the scanning velocity are chosen using Fig. 4.8 to obtain the desired Bragg wavelength. A particular grating reflectivity can be achieved using Eq. (2.53) by choosing the appropriate grating length corresponding to the coupling constant obtained for the chosen pulse energy and writing velocity.

When a particular bandwidth is needed, the coupling constant and the grating length are important parameters to optimize. However, no analytical function gives the value of the FWHM bandwidth as a function of the coupling constant and the grating length. Therefore, numerical methods have to be used to model the grating response and thus give information
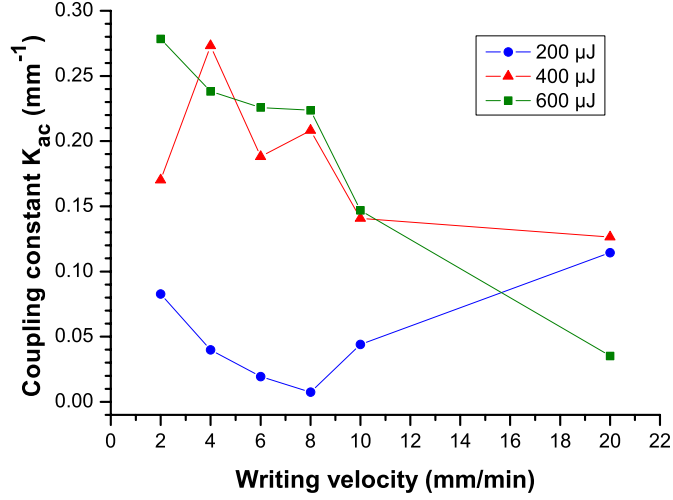
Figure 4.11: Evolution of the coupling constant for 40 mm long gratings written with pulse energies of 200, 400 and 600 µJ. The writing velocities were between 2 and 20 mm/min.

about the grating bandwidth and reflection depending on the grating length and coupling constant. The Transfer Matrix Method [15], for example, can be used. It has however been observed, that, in the case of strong coupling ($\kappa_{ac} > 0.1\text{mm}^{-1}$), the FWHM bandwidth already saturates whereas the reflectivity of the grating still increases from 80 to 100 %(see Fig. 4.12). Thus, for high reflectivity gratings, the FWHM bandwidth can be defined by the choice of the scanning velocity and the writing energy (see Fig.4.6). The length of the grating can be used to fine tune the value of the reflectivity.

4.4. Temperature dependent behavior

As expected in Sec. 3.1.2, type I and type II FBGs can be written with femtosecond pulses [80, 83]. Smelser *et al.* measured the intensity thresholds for type I and type II modifications for static FBGs written with a phase mask technique. The threshold for Type I corresponds to the threshold for grating formation and occurs at an intensity of $1.8 \pm 0.4 \times 10^{13}$ W/cm^2. The threshold for type II was measured when white light generation occurred at $4.6 \pm 0.4 \times 10^{13}$ W/cm^2 [80]. Those thresholds have been compared after conversion to the peak power thresholds measured by Sudrie *et al.* [61] and demonstrate good agreement. However, those thresholds were measured by translating the laser beam with a piezoelement over a distance of ± 10 µm in the fiber core every 20 second. Thus, the thresholds could be slightly different for other exposure conditions like a different scanning velocity.
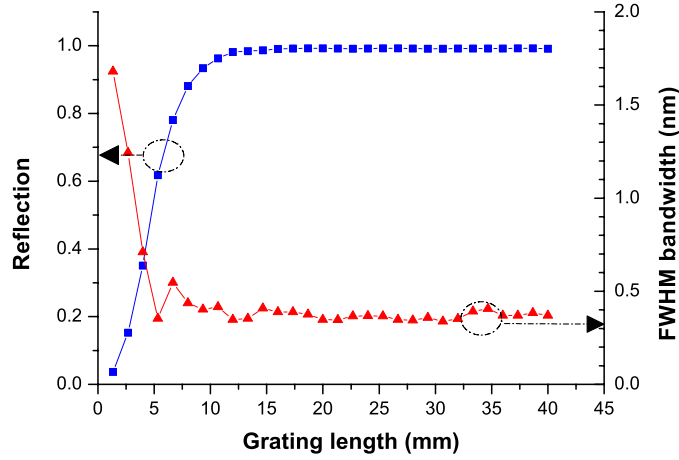
Figure 4.12: Evolution of the grating transmission at the Bragg wavelength and FWHM bandwidth of a FBG written with a pulse energy of 600 µJ and a scanning velocity of 4mm/min in function of the grating length.

The temperature dependent behavior of the gratings confirmed that the grating strength of type I gratings decreased as a function of temperature. Furthermore, the stability of the written gratings is dependent on the strength of the induced refractive index change [84, 85]. For type II gratings, the grating strength increased as a function of the applied temperature. This can be explained by the presence of a type I modification coexisting with the type II modification. As the temperature of the grating is increased, the positive refractive index resulting from the type I modification erases leading to an overall larger negative refractive index modulation. The type of induced modification (type I or type II) can thus be deduced from the temperature dependent behavior of the gratings.

In the following section, the temperature behavior of femtosecond written FBGs with the phase mask scanning technique in the second diffraction order is investigated.

4.4.1. Experimental setup

The setup for the measurement of the temperature sustainability of the gratings is shown in Fig. 4.13. As the fiber can be weakened by the burning of the coating at elevated temperatures, the fiber coating was first stripped off and the fiber was placed in the middle of the tube furnace (Nabertherm, $T_{max} = 1200$°C). The fiber was heated progressively to different temperatures and the transmission spectra were recorded for each step. The temperature of the grating was controlled by a thermoelement placed in the proximity of the grating.
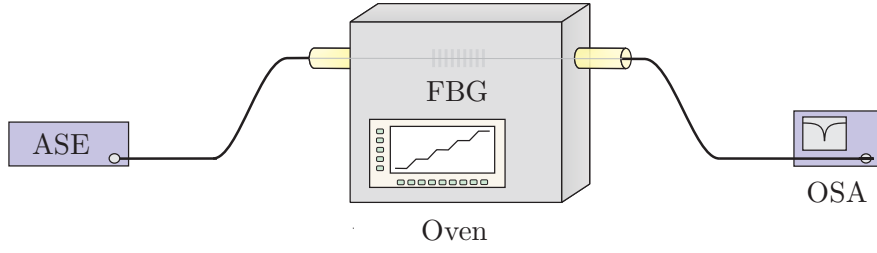
Figure 4.13: Setup for the measurement of the temperature sustainability of the gratings. The fiber containing the FBG is placed in the middle of the tube furnace as well as a thermoelement recording the temperature next to the FBG. The evolution of the grating reflectivity with the temperature is measured in transmission for simplification of the normalization.

The evolution of the refractive index modulation during the exposition to the temperature T is monitored by plotting the evolution of the normalized coupling coefficient NCC defined as

$$NCC(t) = \frac{(\kappa_{ac}L)_t}{(\kappa_{ac}L)_{t=0}} \tag{4.4}$$

where t stands for the time of the measurement and the grating strength $\kappa_{ac}L$ is calculated using Eq. (4.3). The FBG was measured initially at room temperature at $t = 0$.

Using the thermal coefficient α_T defined as $\alpha_T = 1/L \ (dL/dT)$, the elongation of the fiber attributed to a temperature increase can be evaluated by $dL = \alpha_T \ L \ dT$. By heating the fiber at room temperature to $T = 1200°$ C, the fiber elongates of only 0.07 % using the expansion coefficient for fused silica of $0.55 \cdot 10^{-6}$ °C^{-1} [86]. Thus, the grating length can be considered constant and the normalized coupling constant is proportional to the refractive index modulation $(\Delta n)_{\text{eff}}$ (see Eq. (2.49)).

During the measurement, the Bragg wavelength increases as a function of the temperature. Different mechanisms can be responsible for that effect: the thermal expansion of the fiber and the increase of the effective refractive index with temperature. The relative influence of the temperature on the refractive index of the fiber and on the grating period can be evaluated by comparing the value of their temperature coefficients α_n and α_T. The temperature coefficient of the refractive index α_n is defined as $\alpha_n = 1/n \ (dn/dT)$ similarly to the thermal expansion coefficient α_T. For fused silica, $\alpha_n = 8 \times 10^{-6}$ °C^{-1} whereas $\alpha_T = 0.55 \times 10^{-6}$ °C^{-1} [86]. The contribution of both effects is thus constant and depends on the temperature increase profile. However, the average refractive index $(\Delta n_0)_{\text{eff}}$ of the grating has also an influence on the Bragg wavelength and can change during the thermal treatment depending on the type of refractive index modification. Thus, a non linear evolution of the Bragg wavelength gives some information on the evolution of the average refractive index modulation $(\Delta n_0)_{\text{eff}}$ of the grating.

4.4.2. Temperature sustainability

In order to study the temperature sustainability of the gratings, we first studied the behavior of a grating at different temperatures increasing in steps of 100°C for one hour each for a grating written with a pulse energy of 500 µJ and a scanning velocity of 10 mm/min.

Figure 4.14 shows the evolution of the normalized reflectivity as well as of the normalized coupling coefficient i.e. normalized refractive index modulation after one hour annealing at the temperature T for each temperature increase. As can be seen in Fig. 4.14 a, the reflectivity of the grating remains quite stable until a temperature of 600°C. The reflectivity of the grating after one hour heating at $T = 600$°C is still of 95 %. For higher temperatures, the grating reflectivity decreases more abruptly. As can be inferred from Fig. 4.14 b, the normalized refractive index modulation decreases gradually with the temperature even for low temperatures which is characteristic for type I modifications. After one hour annealing at 600°C, 80 % of the refractive index modulation still remains which corresponds to 95 % remaining reflectivity (Fig. 4.14 a). The discrepancy between the evolution of the reflectivity and coupling constant result from the $\tanh^2$ dependence of the grating reflectivity on $\kappa_{ac}L$ (Eq. (2.53)). Thus, as the grating has a length of 40 mm, a reduction of the refractive index modulation has a restricted influence on the reflectivity of the grating. Furthermore, our grating demonstrates a better thermal stability in terms of normalized refractive index modulation than type I gratings written with 193 nm excimer radiation in germanosilicate fibers using two photon absorption [37].
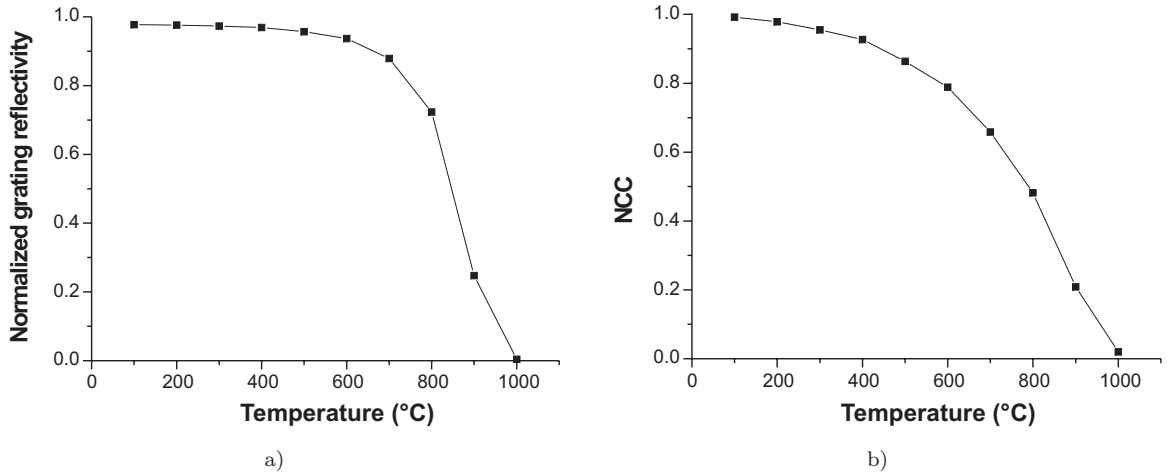
Figure 4.14: Short-term annealing study of a FBG written with the phase mask scanning technique. The temperature was raised in 100°C steps and stabilized for one hour. The evolution of the normalized grating reflectivity (a) as well as the evolution of the normalized coupling coefficient NCC (b) are shown in function of the applied temperature.

67

In order to study the stability of the FBG for high temperature applications, a long term annealing experiment was performed at a temperature of 600°C for a grating also written with 500 µJ and a writing velocity of 10 mm/min (Fig. 4.15). The grating was passed through the tube furnace after the oven temperature was stabilized to 600°C. The normalized coupling coefficient as well as the normalized refractive index modulation dropped quite quickly in the first 60 minutes of the measurement and slowly stabilized to a value of 87 %. This value is similar to the 80 % obtained while heating the FBG successively in 100°C steps. Thus the short-term annealing study of Fig. 4.14 is validated. The Bragg wavelength has a similar behavior except from the instantaneous increase of the Bragg wavelength from 1555.26 to 1563.56 nm which is attributed to the fiber elongation and effective refractive index increase. As the OSA resolution is of 0.06 nm, the stabilization of the Bragg wavelength probably occurred at the same time as the normalized refractive index modulation stabilized.

a)   b)
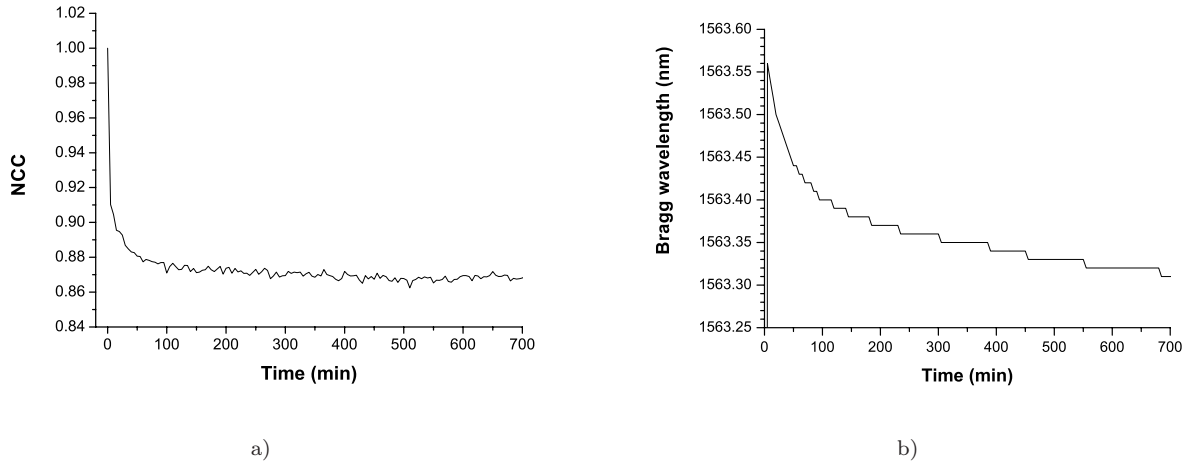
Figure 4.15: Long term annealing study of a FBG at 600°C. The evolution of the normalized coupling coefficient (a) as well as the Bragg wavelength (b) are represented versus annealing time.

4.4.3. Sensor applications

As the Bragg wavelength varies as a function of the applied temperature, FBGs can be used as compact temperature sensors in airborne or restricted environments. However, some hysteresis can occur depending on whether the fiber was cooled down or heated up to the tested temperature. This hysteresis can be induced by the grating annealing in the heating phase. For that reason, the response of the Bragg wavelength with respect to temperature was tested for a FBG first annealed during 40 hours at a temperature of 600°C. The transmission spectra of the grating was measured during the grating was heated from room temperature to

a temperature of 600°C and the oven temperature was monitored using a calibrated thermocouple. The measurement continued after the oven was shut down in order to determine whether the same Bragg wavelength was reached when the grating cooled. Figure 4.16 shows the result for a heating rate of 50°C per hour. The same Bragg wavelength was reached for a given temperature independently whether the grating had been cooled or heated. Thus, the FBG was sufficiently annealed so that the Bragg reflection wavelength did not change during the last heating phase and no hysteresis occurred. Hence, this FBG can be used as a high precision temperature sensor. The curve showing the Bragg wavelength was then fitted with a second order polynomial, which yielded a Bragg wavelength shift of 0.0104 nm/K^{-1}. The error was evaluated to $2 \times 5.38 \cdot 10^{-6}\ T$ and was obtained from the second coefficient of the curve polynomial fit. Furthermore, the grating reflectivity at the end of the measurement was still of 97 % of its initial value which is due to the higher temperature stability of our gratings compared to conventional type I UV written gratings.
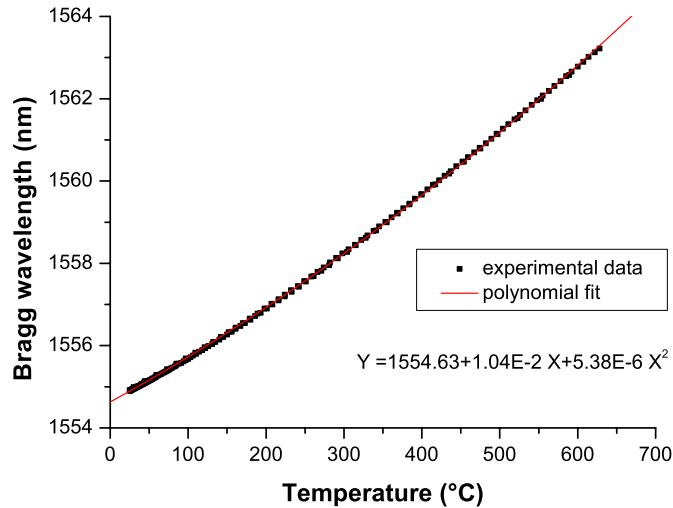
Figure 4.16: Evolution of the Bragg wavelength versus temperature. The annealed FBG was heated continuously at a rate of 50°C per hour until 600°C. The oven was then switched off which resulted in the decrease of the temperature in the oven.

We demonstrated here the efficient inscription of FBGs with IR femtosecond pulses and a phase mask technique. The FBGs can be written statically (without moving the phase mask) or by translating the phase mask and the fiber under the laser beam. This method is called the "phase mask scanning" technique and allows the inscription of FBGs with higher reflectivities and narrower bandwidths, which are of interest for fiber laser applications for example. As the inscription wavelength is of 800 nm, FBGs cannot be written in the first order for Bragg wavelengths of 1.06 µm or less, which limits the application range of our

gratings. We therefore compared the inscription of FBGs using a phase mask scanning technique in the first and second order. Both FBGs demonstrated higher reflectivities and narrower bandwidths than static FBGs. Furthermore, as the first and second order FBGs have comparable efficiencies, second order FBGs were preferably written. The characteristics of the second order FBGs have been studied in more details as a function of the pulse energy and scanning velocity for a Bragg wavelength of 1.55 µm. It has been shown that the coupling constant and Bragg wavelength increase monolithically with the scanning velocity for a pulse energy of 400 µJ. The design of gratings with specific Bragg wavelengths and reflectivities can thus be realized using that pulse energy since an interpolation of the parameters is possible. For a pulse energy of 600 µJ, the Bragg wavelength decreased, which is characteristic of a type II modification and should demonstrate a better temperature sensibility. However, as the Bragg wavelength and coupling constants are varying non linearly in function of the scanning velocity, this pulse energy is not adapted for the realization of FBGs with specific reflectivities and Bragg wavelengths.

The study of the temperature sustainability of a grating written with a pulse energy of 500 µJ and a writing velocity of 10 mm/min revealed a behavior typical for a type I modification as the refractive index modification already decreased at low temperatures. Its temperature behavior should be similar to the gratings written with a pulse energy of 400 µJ with similar refractive index changes. However, 80 % of the refractive index modulation remained at a temperature of 600°C, which is higher than for typical type I UV gratings written with 193 nm excimer radiation. Furthermore, as the grating reflectivity was still of 95 %, the long grating length (L = 40 mm) limited the influence of the decrease of the refractive index modulation. These gratings can be used for temperature sensoring for T < 600°C as the Bragg wavelength remained stable after previous annealing of the FBG at 600°C for 40 hours. It was also shown that no hysteresis in the Bragg wavelength occured depending on wether the fiber had been cooled or heated to the temperature to be measured, making a reliable measurement of the temperature possible.

In the next chapter, the inscription of FBGs into rare-earth-doped fibers as well as their implementation in the realization of fiber lasers is discussed and demonstrated.

5. Fiber laser applications

In the last twenty years, the FBG technology swiftly matured as a technology making the realization of highly compact and efficient fiber lasers possible. The FBGs are thus used as resonator mirrors, which typically have a narrow bandwidth and an operating wavelength for the laser precisely defined by the Bragg wavelength. Furthermore, the coupling losses due to the use of bulk components are avoided and no optical alignment is necessary.

The FBGs are usually written with UV radiation in standard photosensitive fibers and then spliced onto the rare-earth doped fibers. However, in order to increase the laser efficiency and robustness and to scale the output powers, it is favorable to inscribe the FBGs directly into the rare-earth-doped fiber. Doing so, e.g. Distributed Feedback Reflectors have to be written directly into the gain medium as well.

The complexity of the photosensitization mechanisms is nevertheless increased by the presence of the different host glasses optimized for particular rare-earth dopants composition. Therefore, the use of a femtosecond laser alleviates the need for photosensitivity since the refractive index change is attributed to non-linear absorption allowed by the high peak powers of the pulses. This allows to directly write FBGs into rare-earth doped fibers without any particular requirements on the fiber composition (like co-doping with photosensitive dopants) or pre- or post-treatments such as hydrogen loading.

In the following, we demonstrate the flexibility of our method by writing highly reflective FBGs directly into rare-earth doped fibers and use them as resonator mirrors in fiber lasers. Efficient FBGs were written in erbium- as well as in ytterbium-doped fibers and highly simplified, robust and compact fiber lasers with narrow linewidths were realized. We also demonstrate the inscription of FBGs into Polarization Maintaining (PM) fibers which allows for the realization of stable and linearly polarized fiber lasers.

5.1. Erbium-doped fiber laser

Erbium is the privileged rare-earth doped ion for amplification or laser emission in the C telecommunication band around 1.55 µm, which demonstrates the lowest transmission losses in silica fibers. For compatibility purposes, many sources for telecommunications applications are based on erbium-doped fiber lasers. An important application is the implementation

of multichannel sources for Dense Wavelength Division Multiplexing (DWDM). For that purpose, several fiber lasers can be combined [87, 88] or multiwavelength fiber lasers can be realized in a single gain medium provided cross-saturation between the different wavelengths can be suppressed or overcome. Different techniques have been used to define the multiple lasing wavelengths with different types of wavelength selective filters such as chirped grating Fabry Perot cavities or sampled gratings [89, 90], cascaded gratings [91], and scanning Fabry Perot filters [92]. Since these gratings are incorporated in the laser cavity, a direct inscription of the filters in the actively doped fiber would increase the robustness, compactness and efficiency of the fiber lasers. However, polarization effects like polarization hole burning [93] and highly birefringent fibers [94] can also be used to induce multiple wavelength lasing but require the use of polarization controllers which lowers the robustness of the fiber laser.

Because of the low cost of the telecommunication components, a broad spectrum of applications has been implemented in addition to the standard telecommunication applications. One example is the single frequency fiber laser used in spectroscopy, fiber sensor and LIght Detection And Ranging (LIDAR) applications. Single frequency fiber lasers are realized in short cavity lengths using Distributed Bragg Reflectors (DBR), generally spliced to the active fiber [95] or Distributed FeedBack (DFB) [96, 97], directly written into the erbium doped fiber. In order to increase the efficiency of such short length cavity, the pump light absorption can be increased by the adjunction of ytterbium ions, which have a greater absorption cross-section [98, 99]. Another possibility is the use of a Master Oscillator Power Amplification (MOPA) configuration, in which the laser emission from the oscillator is further amplified using the residual pump [100]. Furthermore, high power and ultrashort fiber lasers have been developed for material processing and medical applications, as 1.55 µm is an eye safe wavelength. Clearly, all these applications would benefit from the inscription of FBGs directly into the active doped fiber, which would increase the compactness and robustness as well as the efficiency of the fiber lasers.

In the following, we demonstrate that FBGs can be written directly in erbium-doped fibers with femtosecond pulses. Thus, a codoping with a photosensitive ion or H_2 loading is not necessary and enables a flexible FBG inscription directly into the unprepared erbium doped fiber. We also demonstrate that the written FBGs can be implemented as cavity mirrors in different fiber laser designs using free-space coupling for example. The efficiency of the laser is further enhanced by realizing an all-fibered setup which is more compact, robust and has less intracavity loss.

5.1.1. Characteristics of FBGs written in Er-doped fibers

FBGs were recorded into a highly Er-doped single mode fiber (Liekki Er80-8/125) with a core diameter of 8 μm and a cladding diameter of 125 μm. The fiber core is free from germanium and any other photosensitive dopants. As the fiber cladding and core diameter are similar to the standard telecommunications fibers used in chapter 4, the same focusing and positioning schemes as in Sec. 3.2.3 based on the fiber luminescence were used during the grating inscription. Due to the absorption band of erbium ions which is situated at 800 nm, there was a strong photoluminescence emanating from the fiber due to upconversion processes which aided the alignment procedure.
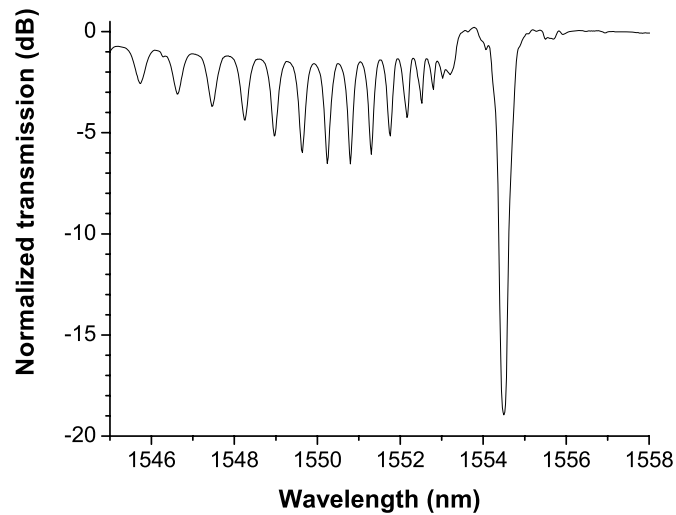

Figure 5.1: Normalized transmission spectra of a grating written with a pulse energy of 640 μJ and a translation velocity of 3 mm/min. The grating length is 40 mm and the grating period Λ_{FBG} is 1.075 μm.

The gratings were written with a grating period of 1.075 μm corresponding to the second order diffraction for a Bragg wavelength of 1554.5 nm which is within the emission spectrum for erbium (1510 nm $< \lambda <$ 1574 nm). The grating length was 40 mm. A typical transmission spectrum is shown in Fig. 5.1 for a grating written with a pulse energy of 640 μJ and a translation velocity of 3 mm/min. The spectrum was recorded by coupling light of the ASE source into the doped fiber. A part of the ASE source was absorbed but enough power was left to record the transmission spectrum of the grating.The transmission loss at the Bragg wavelength of 19 dB corresponds to 98.7 % reflectivity which is similar to the values obtained for gratings written in standard telecommunication fibers (see Sec. 4.3). The insertion losses induced by the grating inscription were negligible.

5.1.2. Realization of erbium-doped fiber lasers

The erbium-doped fiber containing the high reflective FBG of Sec. 5.1.1 can be directly implemented in a fiber laser setup. This was the first demonstration of a fiber laser with a FBG directly written in the active doped fiber with femtosecond pulses and a phase mask scanning technique [101]. The pump beam is coupled into the erbium-doped fiber using a free-space coupling scheme (Fig. 5.2). The laser cavity is constituted by the high reflective FBG mirror and the 4 % Fresnel reflection at the fiber end facet used for the coupling of the pump laser ($\lambda = 976$ nm). An isolator protects the pump laser diode from back reflections and a tilted dichroic mirror deviates the laser output beam ($\lambda = 1554.5$ nm) for the measurement of the laser spectrum as well as the laser output power.
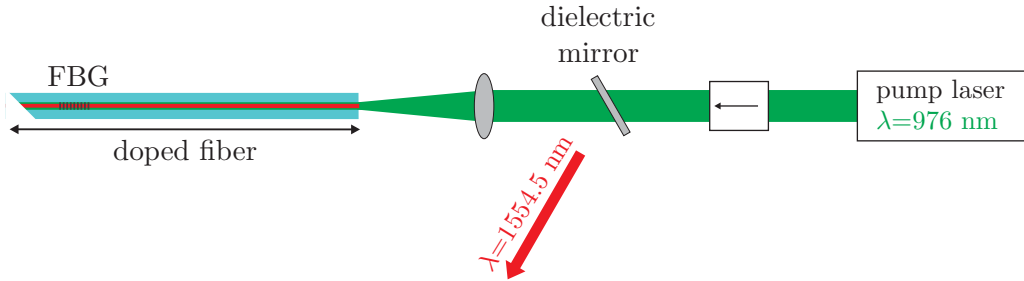
Figure 5.2: Erbium fiber laser setup with free beam coupling

As can be seen in Fig. 5.3 a), the laser wavelength of 1554.5 nm corresponds to the Bragg wavelength of the grating (Fig. 5.1). The signal to noise ratio is of remarquable -60 dB. The evolution of the laser output power vs. pump power is shown in Fig. 5.3 b). A maximum output power of 40 mW was measured and as no saturation effects are visible, the output power is only limited by the available power of the pump laser diode. The measured slope efficiency was of 21.1 % (Fig. 5.3 b). The quite low slope efficiency is partly attributed to low coupling efficiency of the pump power into the actively doped fiber. Another reason is that the fiber length was not optimized to minimize the reabsorption of the laser beam in the fiber.

In order to avoid the losses induced by the free space coupling, a Wavelength Division Multiplexer (WDM) coupler (Fig. 5.4) is used to inject the pump into the doped fiber and prevent coupling of the laser into the pigtailed laser diode. The pump laser itself is protected from possible pump back reflections at the fiber splices by an isolator.

The high reflecting FBG used in this experiment was written with a length of 40 mm and has a maximum loss of 16.15 dB at the Bragg wavelength of $\lambda =$1556 nm corresponding to a reflectivity of 97.6 %. It was written with a translation velocity of $v = 5$ mm/min and a pulse energy of $E = 500$ µJ. The transmission spectrum of the FBG is shown Fig. 5.5.

74

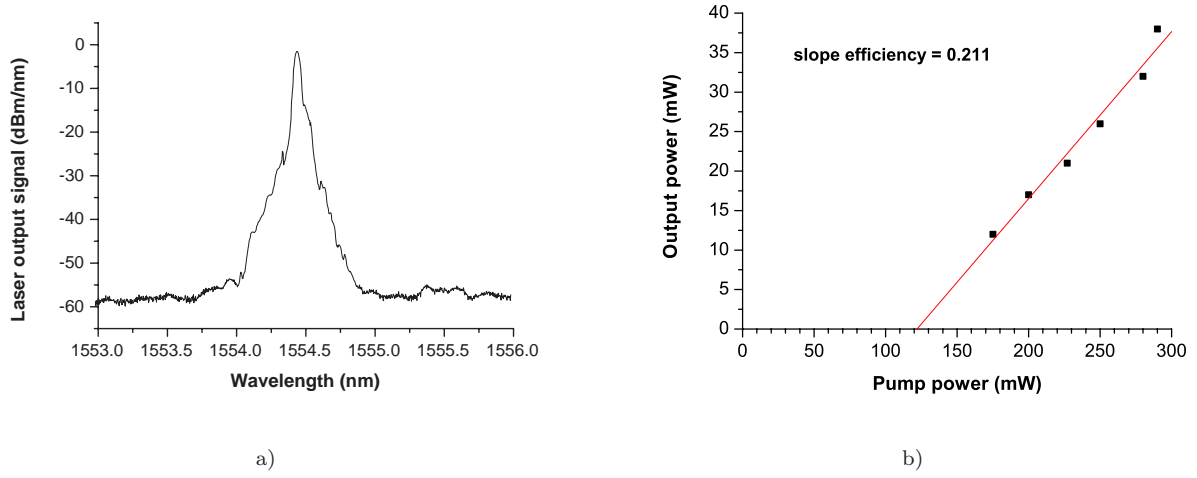a)   b)

Figure 5.3: Output spectrum a) and output power vs. launched pump power b) of the erbium-doped fiber laser with free beam pump coupling.
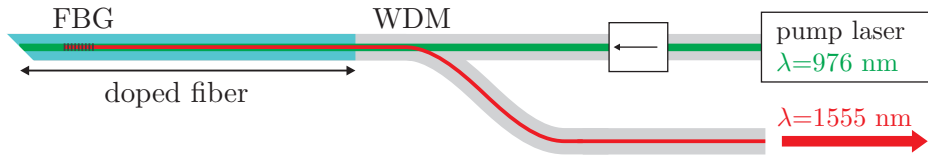

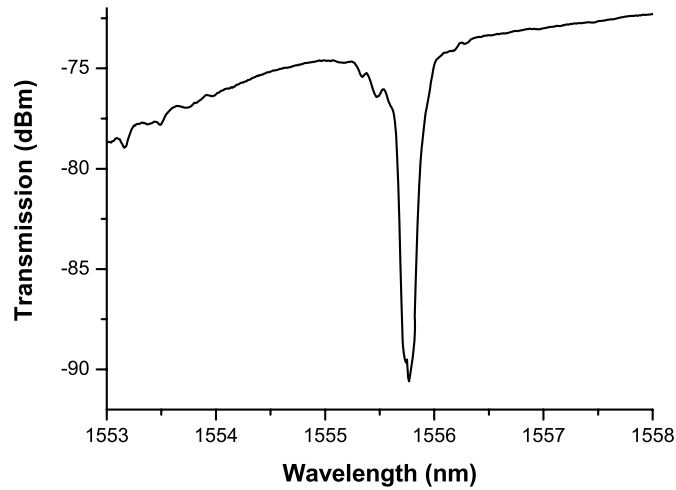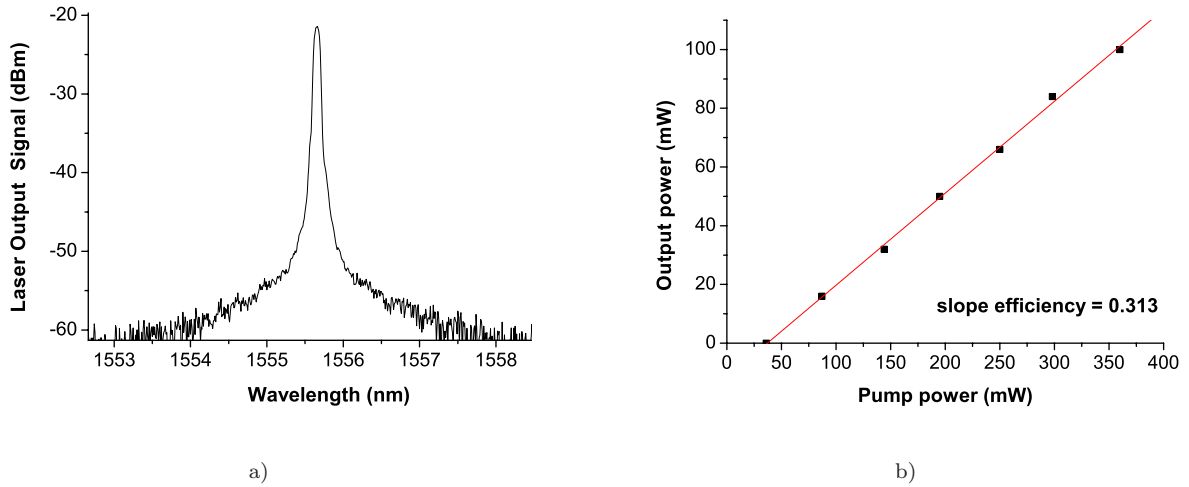**Figure 5.4:** All-integrated erbium fiber laser setup

Figure 5.5: Transmission spectrum of the FBG written in the erbium-doped fiber with a pulse energy of 500 µJ and a velocity of 5 mm/min.

75

Figure 5.6: Output spectrum a) and output power vs. launched pump power b) of the all-integrated erbium-doped fiber laser.

The output cavity mirror consists of a 4 % Fresnel reflection off the perpendicularly cleaved end facet at the output of the WDM.

The evolution of the laser output power vs. pump power is shown in Fig. 5.6 b). It exhibits a non-optimized slope efficiency of 31.1 % and a maximum output power of 100 mW for a launched power of 375 mW. The laser threshold is of the order of 30 mW. The slope efficiency can be increased by using an optimal output coupler and an optimized cavity length. The output signal had a FWHM bandwidth limited by the OSA resolution (< 0.06 nm) and a signal to noise ratio of -45 dB (see Fig. 5.6 a)).

In conclusion, we have demonstrated that efficient FBGs can be written into Erbium-doped fiber using writing parameters similar to those used for the inscription of FBGs into standard telecommunication fibers. This demonstrates the flexibility of our method. Furthermore, the positioning of the modifications using the induced luminescence is facilitated by the upconversion of the absorbed photons at 800 nm. Moreover, these highly reflective FBGs have been implemented in a free-space and a monolithic fiber laser setup which facilitate the realization of robust and monolithic fiber lasers. In comparison with the free-space coupling scheme, for comparable grating reflectivities (97.6 % versus 98.7 % for the free-space coupling) and comparable doped fiber lengths (72.5 versus 85 cm for the free-space coupling) above the optimum length defined by the absorption length of the fiber (calculated from the absorption coefficient of 23 dB/m at 976 nm), the lasing threshold is lower and the slope efficiency increased which is due to the lower coupling losses into the laser cavity.

5.2. Ytterbium-doped fiber laser

Ytterbium has the advantage of having a broad absorption band (850 nm $< \lambda_{\text{abs}} <$ 1070 nm) associated to a broad fluorescence (970 nm $< \lambda_{\text{fluor}} <$ 1200 nm). Furthermore, ytterbium ions have high absorption and emission cross-sections and an effective energy conversion close to the quantum-limited operation. Therefore, Yb-doped fibers are currently used for the realization of high power fiber lasers.

However, as non-linear effects limit the power scaling, new fiber designs like Large Mode Area (LMA) [102, 103], microstructured fibers [104] have been developed to allow the propagation of higher energy densities. In order to realize efficient monolithic fiber lasers, the splicing routines must be optimized for each new fiber design and the passive fibers containing the UV written FBGs have to be designed accordingly to allow a good mode matching between the active and the passive fiber containing the FBGs. Furthermore, due to the high energy densities, the splices can be damaged or have an impact on the robustness of the fiber laser. Therefore, the inscription of FBGs directly into the active fiber is necessary to enable the realization of more robust high power fiber lasers.

Another approach to power scaling is the use of a Master-Oscillator Power-Amplifier (MOPA) configuration, whereby the pump power absorbed in the amplifier part allows amplification of the low power oscillator signal. Since the FBGs are within the low power oscillator, power scaling is not a problem for the splices, but induce extra losses within the cavity that should be avoided. Therefore, the direct writing of the FBGs into the core of an active fiber is desirable in all laser configurations.

In the following, we demonstrate the successful inscription of FBGs directly into highly Yb-doped single mode fibers and the potential of our technique to inscribe FBGs in different fibers such as Polarization Maintaining (PM) and Large Mode Area (LMA) fibers. Using these FBGs, we realize a stable single polarization, narrow linewidth (<0.06 nm) fiber laser in a greatly simplified manner.

5.2.1. Characteristics of FBGs written in single mode Yb-doped fibers

FBGs were successfully written into standard Yb-doped single mode fibers having a cladding diameter of 125 µm and a core diameter of about 4.5 to 6 µm. Using the same cylindrical lens as in the former experiments yields a higher overlap integral as the mode field diameter is smaller and the spatial dimensions of the refractive index change remain constant. The phase mask used had a pitch of 1.435 µm corresponding to a second order Bragg grating for a Bragg

wavelength of 1.044 µm. Figure 5.7 shows the transmission spectrum of a grating written in an Yb-doped single mode fiber with a pulse energy of 400 µJ and a scanning velocity of 2 mm/min. The spectrum was measured by pumping the Yb-doped fiber with a pigtailed laser diode ($\lambda = 976$ nm) protected by a spliced on isolator. The power of the pump laser was chosen so that enough ASE is produced to measure the transmission spectrum of the laser. However, the power of the pump laser was kept quite low in order to avoid the building up of a fiber laser cavity lasing at the Bragg wavelength which would lower the power of the entire ASE and narrow the spectrum of the emission. The transmission loss at the Bragg wavelength was about 24 dB which corresponds to a reflectivity of 99.6 %. Thus, FBGs can also be written into ytterbium doped fibers with comparable performances as those of standard single mode and erbium doped fibers and fiber lasers can be realized.
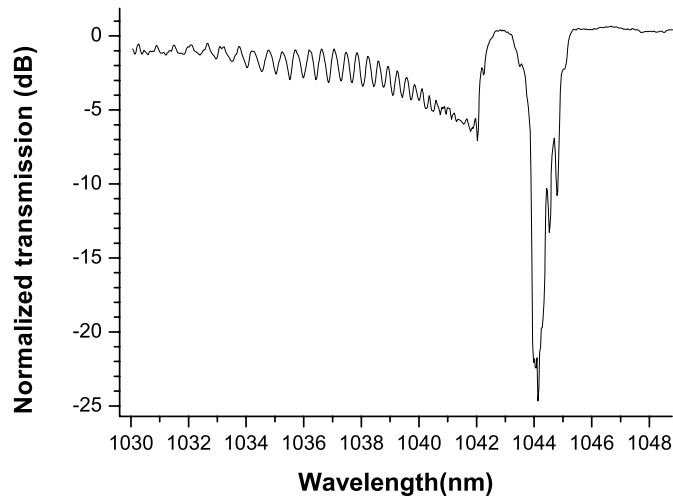
Figure 5.7: Normalized transmission spectrum of a FBG written in an Yb-doped single mode fiber with a pulse energy of 400 µJ and a scanning velocity of 2 mm/min. The period of the FBG is 0.7375 µm and the grating length is 40 mm.

However, due to polarization mode competition, the stability of the fiber laser can be affected by external perturbations. Thus, the fiber laser stability can be increased by the use of PM fibers as polarization mode competition can be avoided when only one distinct polarization is propagating through the fiber. Therefore, the inscription of FBGs in PM fibers as well as their implementation in the realization of single polarization fiber lasers will be studied in the next sections.

5.2.2. Characteristics of FBGs written in PM fibers

PM fibers are birefringent, which means there are two well defined axes in the core that are orthogonal to one another which have different indices. Hence, a mode propagating down the fiber will experience two effective indices for the two orthogonal states of linear polarization. Thus the cross-talk between the two polarization eigenmodes is minimized, although it can become significant with fiber twist and bending. The birefringence can be achieved by introducing Stress Applying Parts (SAP) on both sides of the fiber core or by the implementation of an elliptical fiber core [105]. The PM fibers fabricated using the introduction of SAPs near the fiber core have usually a higher birefringence and can sustain higher bend radius or stresses.

Highly birefringent fibers are constituted of two SAPs on both sides of the fiber core. Depending on the shape of the SAPs one distinguishes mainly between the bow-tie fiber and the panda fiber. The panda fiber is constituted of two round SAPs as can be seen in Fig. 5.8. The SAPs are typically made of boron-doped silica which have a larger thermal expansion coefficient than the cladding. Thus, during the cooling following the fiber drawing, the SAPs shrink and induce a tensile stress in the fiber core leading to stress induced birefringence. The direction perpendicular to the plane of the SAP is called the fast axis and has a lower effective refractive index than the slow axis which is orthogonal to it.

One particular characteristic for FBGs written in PM fibers is the two different reflection peaks due to the fiber birefringence. Indeed, a birefringent fiber has two perpendicular polarizations guided with two different propagation constants and thus two different effective refractive indices. The birefringence B of an optical fiber is defined as the difference between the two effective indices of both polarization directions i.e. $B = \Delta n_{\text{eff}}$. As the value of the Bragg wavelength is proportional to the effective refractive index, each polarization direction has a different Bragg wavelength. Thus, the splitting of the Bragg wavelength $\Delta\lambda_B$ reads as

$$\Delta\lambda_B = \frac{\Delta n_{\text{eff}}\lambda_B}{n_{\text{eff}}} \tag{5.1}$$

using Eq. (2.40) and considering a constant grating period. As the refractive index modification is strongly asymmetric and induces some birefringence (Sec. 4.1), the orientation of the modification with respect to the fiber main axes might have an influence on the fiber birefringence. Thus, the Bragg wavelength splitting can differ from the theoretical value and a increased cross-talk attributed to a decrease of the birefringence can be induced.

Figure 5.9 shows the transmission spectra of a FBG written into a standard PM fiber (Fujikura SM98-PS-U25A) measured with a linearly polarized ASE source. Two sets of

refractive index profile in the x direction
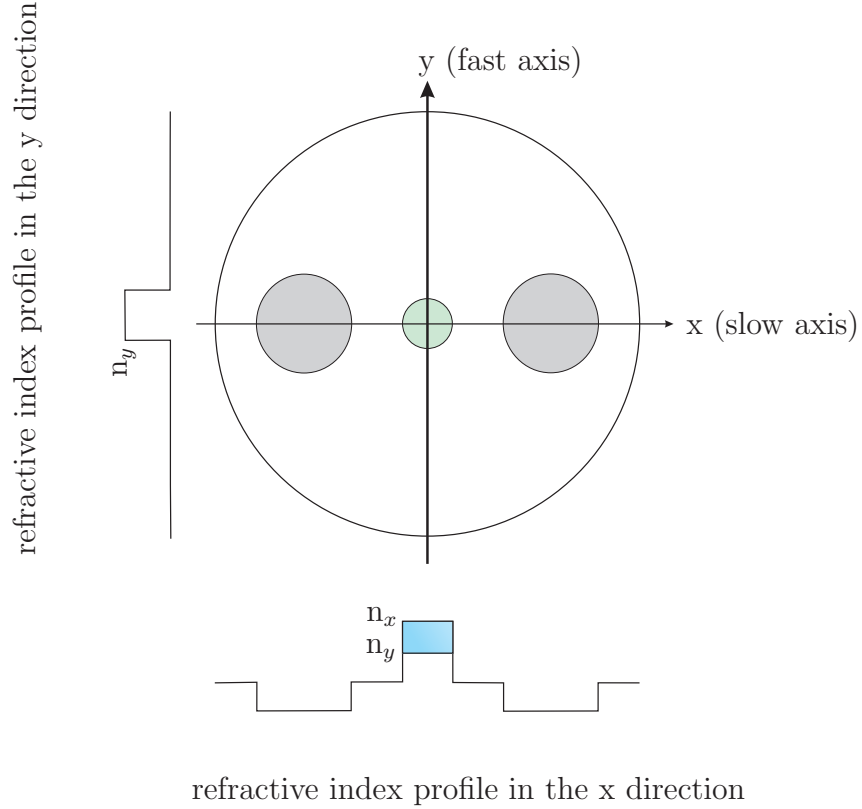
Figure 5.8: Fiber cross-section of a panda PM fiber. The Stress Applying Parts induce a tensile stress resulting in a higher refractive index in the y direction.

spectra are recorded by rotating the polarization using a half wave plate until the maximum and the minimum wavelength shift are observed.

The two peaks are separated by a distance of 0.38 nm which corresponds to a birefringence of $\sim 5 \times 10^{-4}$. In order to evaluate the amount of birefringence induced by the grating inscription, the birefringence of the PM fiber before inscription is measured.

The fiber birefringence can be determined by measuring the beat length L_B which is linked to the fiber birefringence B by $L_B = \lambda/B$. By sending circularly polarized light into the fiber, due to the two different propagation constants, the beam becomes periodically linearly polarized (Fig. 5.10). The beat length is defined as the distance between two points having the same polarization state.

Using Rayleigh scattering, the scattering of plane-polarized light is null in the direction of the electric-field and maximum perpendicular to it. Thus, observing light scattered at an angle of 45° to the fiber principal axes will lead to a periodical pattern having a period equal to the beat length if circularly polarized light (or linearly polarized light with a 45 degree angle to the fiber principal axes) is launched.

Figure 5.11 shows the experimental setup used for the measurement of the beat length using Rayleigh scattering. Light from an Helium Neon laser was coupled into a PM fiber
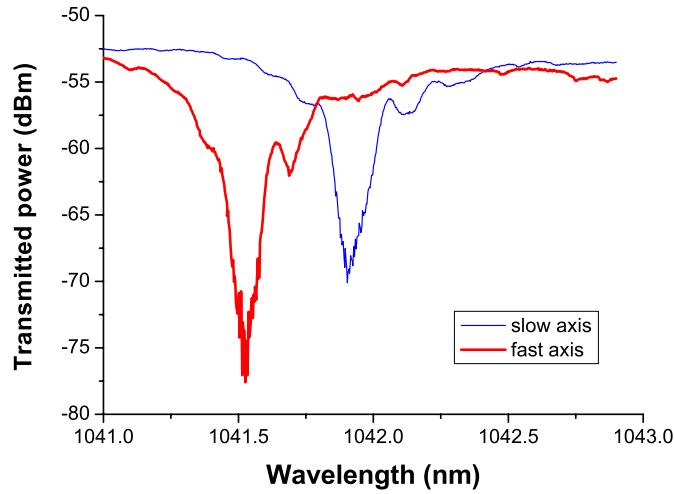
Figure 5.9: Transmission spectrum of a grating written in a PM fiber with a pulse energy of 500 µJ and a velocity of 8 mm/min.
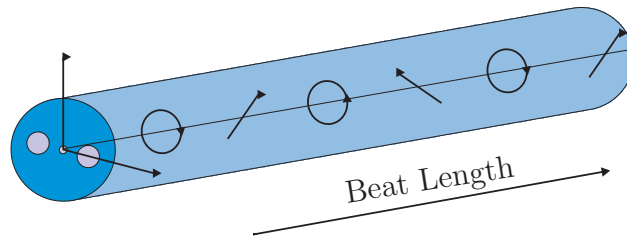
Figure 5.10: Propagation of circularly polarized light through a birefringent fiber. The beat length defines the distance between each same polarization state. Light is periodically linearly polarized with a 45 degree angle with respect to the fiber axes.

(right side). This PM fiber was rotated so that the polarization was in the observation axis of the camera. The fiber to measure (left side) was rotated so that a periodical pattern could be measured along its axis by translating the camera along the fiber axis. This is achieved for an angle of 45° between the main axes and the incident polarization. A microscope objective is used to image the fiber on the camera. The axis on which the camera and the focusing objective are fixed to is then translated along the fiber axis using a step motor. Thus, several pictures of the scattered pattern are made and several periods of the scattered pattern can be represented.

Figure 5.12 a) shows a picture of the scattered light from the panda PM fiber used in the former experiments when the fiber was rotated with an angle of 10° until a periodical pattern was observed. The resulting angle between the fiber main axes and the incoming polarization must thus be of about 45°± 10°. Such a precision is however sufficient as two pictures separated by an angle of 10° show the same periodical pattern. The evaluation of

81
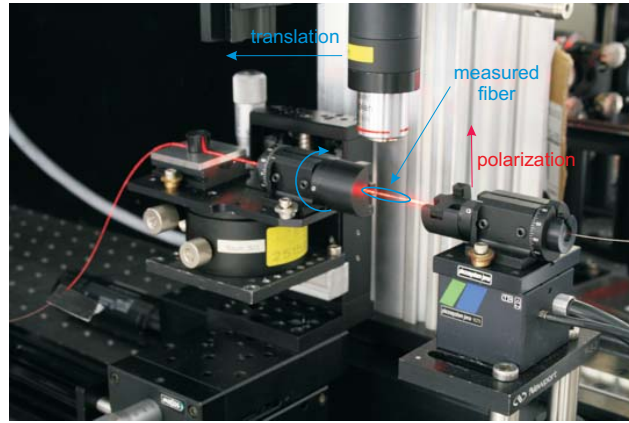
Figure 5.11: Setup for the measurement of the beat length using Rayleigh scattering.

the beat length is made by isolating the periodical pattern in the middle of the fiber and by fitting it with a cosine square function (Fig. 5.12 b). The period of the scattered light which is defined as the beat length is then half the period of the cosine square function. The beat length of the PM fiber containing the FBG of the previous experiment is thus evaluated to 1.47 mm.

As a consequence, the initial birefringence of the fiber evaluates to 4.3×10^{-4} which leads to a theoretical Bragg wavelength splitting of $\Delta\lambda_{B\text{th}} = 0.32$ nm. The theoretical and the measured values for the Bragg wavelength splitting are comparable and the difference between

a)   b)
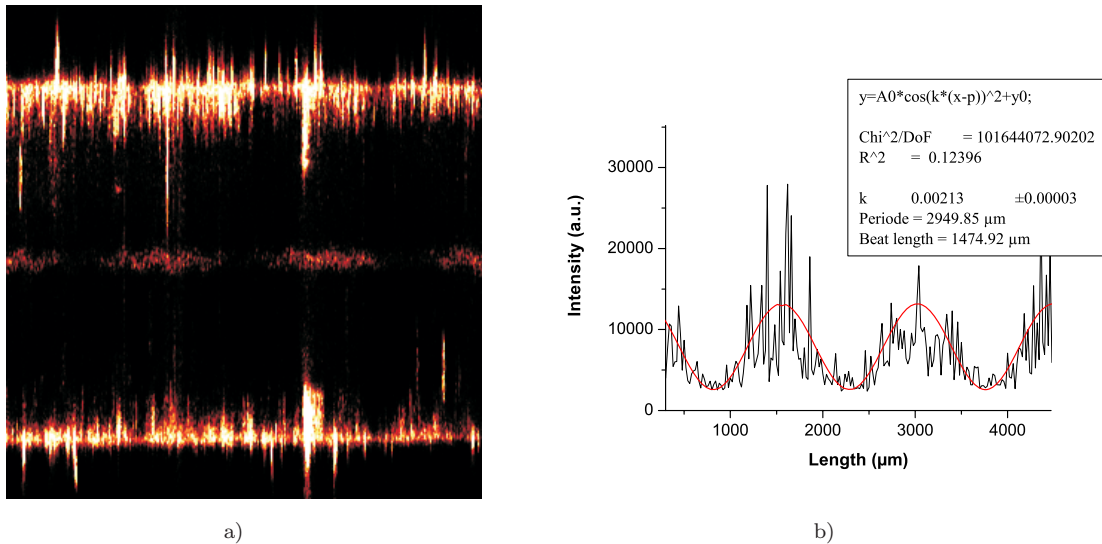
Figure 5.12: Measured (a) and fitted (b) periodical Rayleigh scattering from the PM fiber containing the FBG represented in Fig. 5.9. The PM fiber was rotated with an angle of 10° until a periodical pattern was recognizable. The beat length is obtained by fitting the scattered light with e.g. a cosine squared function which allows to evaluate the period of the scattered light.

both values is within the limits of uncertainty given by the 0.06 nm resolution of the OSA. Thus, the FBG inscription had a negligible influence on the fiber birefringence. Considering one polarization, as no transmission loss was observed at the Bragg wavelength of the other polarization (Fig. 5.9), no cross-talk occurred. The difference in the value of the transmission dips at the Bragg wavelengths is attributed to the different overlap integrals resulting from the slightly different confinement of the modes along both polarization directions. This difference in the confinement of the modes was also observed as light was coupled with different efficiencies depending on the orientation of the polarization along the main axes of the fiber. Thus, the different diffraction efficiency is not necessarily a consequence of the change in the total birefringence.

### 5.2.3. Realization of a single-polarization ytterbium-doped fiber laser

We demonstrate in the following the implementation of PM fibers containing FBGs for the realization of single polarization fiber lasers. The FBG was written directly with a pulse energy of 600 µJ and a writing velocity of 4 mm/min into a panda type PM ytterbium-doped fiber (having a core diameter of 4.8 µm and a cladding diameter of 125 µm). The grating has a length of 40 mm. The transmission spectra for both polarization directions are shown in Fig. 5.13. The two transmission dips are separated by 0.2 nm and correspond to $\sim 55\%$ transmission losses for the fast axis at $\lambda_{FA} = 1043.05$ nm and ~ 35.4 % transmission losses for the slow axis at $\lambda_{SA} = 1043.25$ nm. In contrast with the FBG of Fig. 5.9, some extra losses are observed at a wavelength corresponding to the Bragg wavelength of the other polarization meaning that a cross-talk between both polarizations took place. Furthermore, the Bragg wavelength splitting is of the order of 0.2 nm. Thus, the total birefringence of the fiber decreased. However, even if the FBGs have non smooth spectra, a fiber laser can still be set up with reasonable performance.

The fiber laser was set up as represented in Fig. 5.14 using the written FBG as the highly reflecting cavity mirror. The pigtailed pump laser diode ($\lambda = 976$ nm) was spliced to an isolator to avoid back reflections into the pump. Furthermore, to protect the pump laser from fiber laser radiation, we spliced a WDM coupler between the isolator and the side of the Yb-doped fiber containing the grating. The free end of the WDM was angle cleaved to avoid parasitic back reflections into the fiber laser cavity. The output coupler was realized by a bulk mirror reflecting 10 % of the fiber laser emission. Between the end of the doped fiber and the output mirror, a polarizing cube was inserted to select the polarization propagating through the laser cavity.

The laser characteristics were studied for both the slow and fast axes. The fiber laser op-
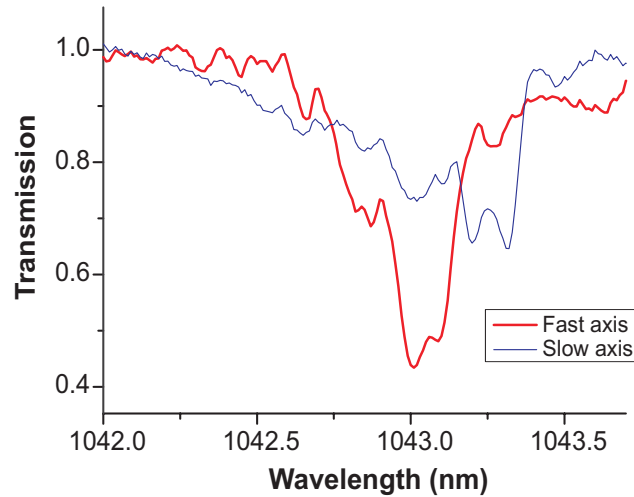
Figure 5.13: Transmission spectra of the FBG written in the Yb-doped fiber with 600 µJ pulse energy and a translation velocity of 4 mm/min. The polarization of the ASE source was aligned with the two axes of the PM Yb-doped fiber.
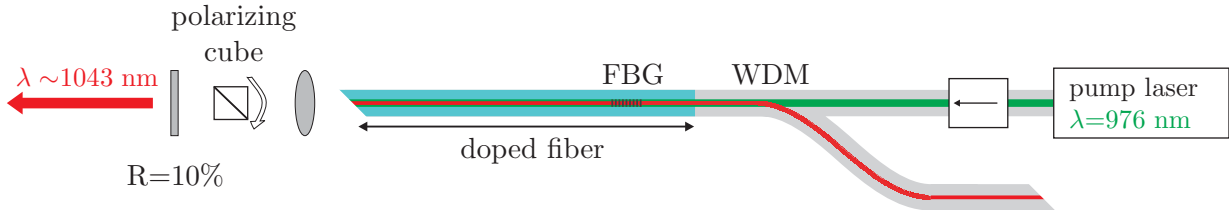
Figure 5.14: Setup for the linearly polarized fiber laser. The polarization cube is rotated to match the polarization direction of the stimulated emission with the slow and fast axes of the PM fiber.

erated off two wavelengths non-simultaneously, separated by 0.2 nm which is consistent with the wavelength spacing defined by the FBG. The small discrepancy between the Bragg wavelengths and the laser spectra can possibly be explained by the use of a differently calibrated OSA.

The non-optimized laser output power versus launched pump power is represented in Fig. 5.15 (b) and has the same slope efficiency for both polarizations (29.2 %).The pump power launched in the fiber laser was measured after the isolator. We did not take into account the losses induced by the WDM, the FBG or the splice losses. Taking those into account would yield a lower maximum launched power and hence a greater laser slope efficiency. An optimization of the laser efficiency was not the purpose here rather the first demonstration of the realization of a fiber laser incorporating a FBG written directly into a PM Yb-doped fiber.

The free space coupling scheme consisted of 3 extra-fiber elements for the selection of the polarization, which induced extra losses in the laser cavity and reduced the laser efficiency. Alternatively, the polarization selection could be achieved using a fiber based polarization
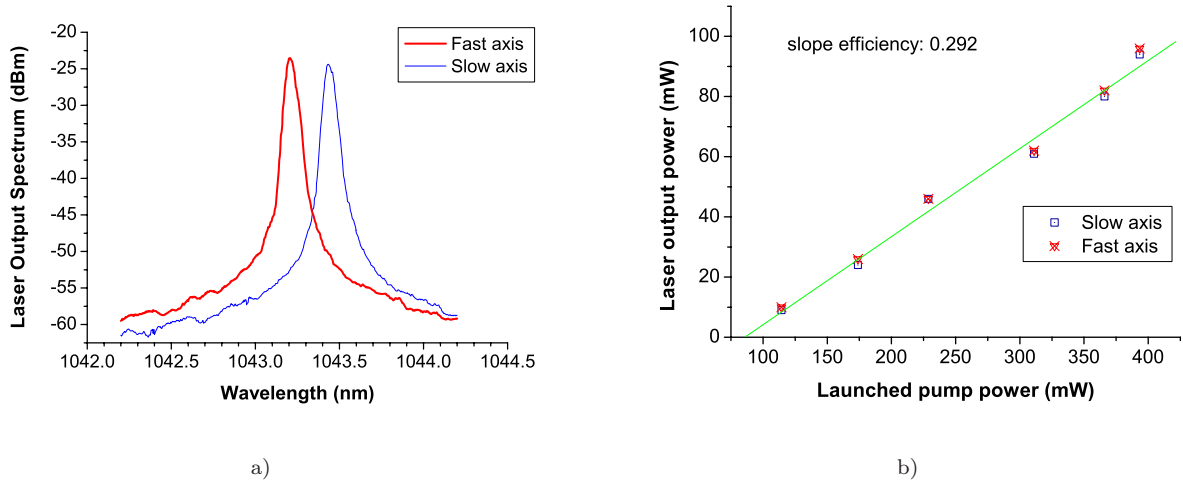
Figure 5.15: Characteristics of the ytterbium fiber laser for both polarization directions (light polarized along the slow and the fast axes of the PM fiber).a) represents the output laser spectrum and b) laser output power vs. launched pump power measured after the isolator.

controller spliced into the fiber cavity [106] or by splicing the PM fibers containing the FBGs so that the fast axis of one PM fiber is parallel to the slow axis of the other PM fiber [107]. Thus, only one polarization allows the simultaneous overlap of the reflection peaks of both PM fibers. This corresponds to the fast axis of the low reflectivity grating and to the slow axis of the high reflectivity (HR) grating. As the Bragg wavelengths of the low reflectivity grating is smaller than for the HR FBG, the Bragg wavelength is shifted by applying a constant temperature in order to assure the maximal overlap of the fast axis of the low reflectivity grating with the slow axis of the high reflectivity grating. This technique of polarization selection is used because the wavelength splitting of both fibers is comparable. However, by writing FBGs with our technique, the total fiber birefringence can be changed by varying the orientation of the birefringent refractive index modification. The wavelength separation of the Bragg wavelength of the slow and fast axis can thus be controlled by the orientation of the modification. Therefore, if both FBGs constituting the laser cavity have different wavelength separations, the propagating polarization can be selected by choosing which of the slow axis or fast axis reflections overlap. The FBG having the lower Bragg wavelengths is thereby heated or submitted to a strain in order to controll the shifting of the Bragg wavelength. Using that technique, both gratings can thus be realized in the same PM fiber which greatly improves the robustness of the laser.

The orientation of the asymmetric refractive index modification relative to the SAPs can be controlled by monitoring the luminescence resulting from the non-linear absorption of the SAPs and the fiber core. Figure 5.16 shows the luminescence spectra observed for different

positions of the focused laser beam in the fiber. The distance between the fiber and the cylindrical lens is kept constant whereas the fiber is translated perpendicular to the fiber axis. The same panda PM Yb-doped fiber as in the former experiment is used for our luminescence measurements. On both sides of the Yb-doped fiber core characterized by a luminescence around 450 nm, a strong blue luminescence ($\lambda = 400$ nm) corresponding to the stress applying parts is detected. As the SAPs have a different dopant composition than the Yb-doped core, the spectrum of the induced luminescence can be used to distinguish between the fiber core and the SAP. By rotating the fiber and observing the relative intensity of the luminescence characteristic for the SAPs or the ytterbium doped fiber core, a particular position of the modifications relative to the SAPs can be reached. When the luminescence corresponding to the SAPs is maximized and is measured on both sides of the fiber core, the SAPs are in a plane perpendicular to the laser beam. In the contrary, if the luminescence corresponding to the SAPs is measured in the middle of the fiber and the luminescence corresponding to the fiber core is barely measurable, the plane of the SAPs is parallel to the laser beam.
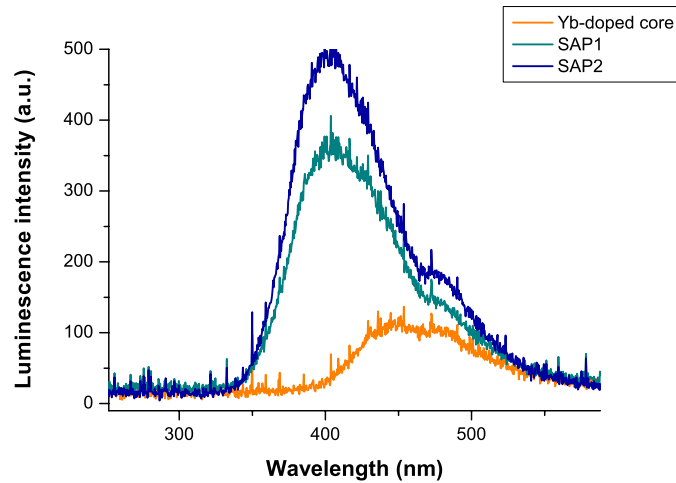
Figure 5.16: Luminescence measured at the fiber side while focusing the laser beam into the fiber core. By translating the fiber perpendicular to the fiber axis while the distance between the fiber and the focusing lens was kept constant, different kinds of luminescence are detected. They correspond to the SAP and to the active core of the PM Yb-doped fiber.

In that case, it is difficult to precisely position the laser beam in the fiber core because of the parasitic luminescence of the SAPs. Therefore, the SAPs should be first oriented perpendicular to the laser beam to allow the measurement of the luminescence attributed to the fiber core, which allows the accurate positioning of the laser beam into the fiber core. The primary orientation of the SAPs can be known using the alignment routine of the SAPs

of the splicing machine.

5.3. FBG inscription into Large Mode Area fibers

In the former sections, the inscription of FBGs and the realization of compact and robust fiber lasers based on standard single mode ytterbium doped fibers has been studied. However, other types of fibers can be used for the realization of high power fiber lasers such as Large Mode Area (LMA) fibers in which higher power densities can propagate without inducing non-linear effects limiting the power scaling.

We demonstrate here what we believe to be the first inscription of a FBG into a LMA fibers using a phase mask scanning technique. The fiber used in our experiments is a PM Ytterbium doped LMA fiber (Liekki Yb-1200-20/125 DC-PM). The cladding has a diameter of 125 µm similar to the cladding diameter of the single mode fiber previously used, which allows us to use the same focusing conditions i.e. cylindrical lens as before. The core diameter of the ytterbium doped fiber was of 20 µm. Due to the large diameter of the fiber core, the fiber is not necessarily single mode and higher order core modes can exist. The laser beam was positioned into the fiber core of a single mode fiber having the same cladding diameter by monitoring the luminescence. The single mode fiber was then removed and replaced by the LMA fiber. The FBG was then written by translating the phase mask and the fiber under the laser beam in the direction of the fiber axis without changing the distance between the cylindrical lens and the phase mask. The grating was 40 mm long and was written with a pulse energy of 470 µJ and a scanning velocity of 4 mm/min. The transmission of the fiber containing the FBG was measured after the grating inscription and can be seen in Fig. 5.17. Light from an ASE source was coupled into the fiber using butt-coupling and the output light was coupled into a single mode fiber connected to the OSA using a collimating and a focusing lens.

A main transmission loss of 12 dB was measured at a wavelength of $\lambda_B = 1041.2$ nm, which demonstrate the feasibility of the FBG inscription with femtosecond pulses and a phase mask scanning technique. A satisfactory overlap of the modifications with the large fiber core is assured through the low NA focusing assured by the cylindrical lens, which is not necessarily the case using a "point by point" technique in which the modifications are of the order of 1 µm [108].

The high losses on the short wavelength side of the Bragg wavelength can be attributed to a coupling to the cladding modes or to higher order core modes. The nature of the coupling is not considered here in more details as a calculation of the fiber modes is necessary and is

87
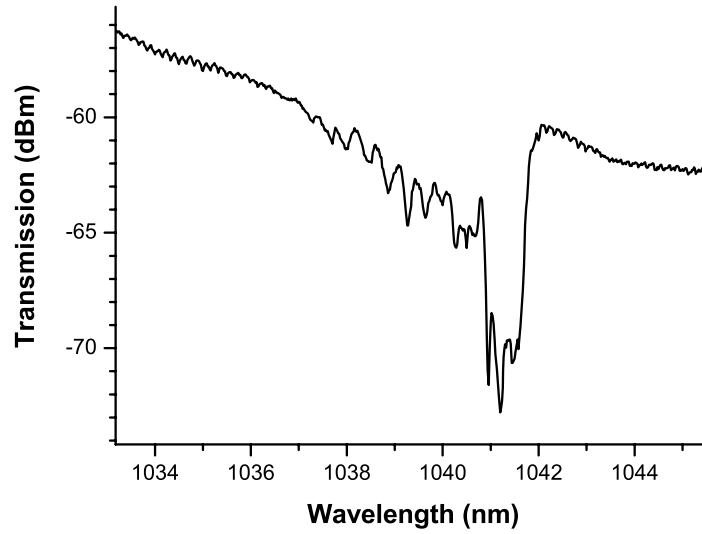
Figure 5.17: Transmission of a PM LMA Yb-fiber containing a 40 mm long FBG written with a pulse energy of 470 µJ and a scanning velocity of 4 mm/min

not under the scope of our investigation. However, the coupling to the cladding modes can easily be avoided by writing the modification across the whole fiber core. Furthermore, the efficiency of the grating is also increased as the modifications have only a width of 2 µm.

In this section we demonstrated the potential of our technique to inscribe efficient FBGs in ytterbium doped fibers. The scope of applications can be increased as the FBGs can also be written into PM fibers, which allows the realization of stable and linearly polarized fiber lasers. The polarization selection was made using a polarization cube, which induced extra losses in the cavity. Alternatively, a fibered polarization controller or two FBGs written in a PM fiber and spliced with perpendicular axes can be used. We proposed a novel technique for polarization selection based on the inscription of two FBGs with different total birefringence in the same actively doped PM fiber, which reduces the losses and greatly improves the simplicity and the robustness of the setup. Since FBGs written with ultrashort pulses and a phase mask technique have a strong asymmetry and are birefringent, the birefringence of the fiber containing the grating can be modified by controlling the orientation of the modification with respect to the main axes of the PM fiber. As the FBGs have a different Bragg separation, the reflection of the both grating can only overlap for one particular polarization, which is controlled by shifting the reflection wavelength of one grating by applying a constant temperature or tension to one of the gratings. The control of the orientation of the SAPs with respect to the inscription laser beam is made by monitoring the luminescence attributed to the SAPs and the fiber core, which have different spectra due to their different dopant

compositions. We also demonstrated, that, due to the long depth of the modifications, the overlap of the grating with the core of a LMA fiber is sufficient and FBGs with a length of 40 mm and a reflectivity of 90 % can be written by phase mask scanning. This opens new possibilities for the realization of monolithic high power lasers without the necessity of splicing the FBGs.

In conclusion, we have demonstrated the inscription of FBGs directly into ytterbium and erbium doped fibers with femtosecond pulses using a phase mask scanning technique. The presence of the rare-earth dopant had no influence on the non-linear absorption process. Thus, our inscription method is universal and do not depend on the fiber chemical composition. Hence, a cost-intensive optimization of the dopant concentrations is avoided. Furthermore, we demonstrated that FBGs directly written into rare-earth doped fibers can be used as cavity mirrors and allow the realization of compact, robust and efficient fiber lasers. We also demonstrated that the inscription of FBGs in PM fibers is possible without changing the initial birefringence of the fiber. However, as the refractive index change is asymmetric and birefringent, the grating birefringence can be influenced by the orientation of the grating with respect to the main axes of the PM fiber. This opens the field for new applications such as the polarization selection using two FBGs with different wavelength separations. As the FBGs can also be written efficiently in rare-earth doped PM LMA fibers, the realization of new monolithic high power fiber lasers becomes possible. Thus, new fiber laser designs based on the use of FBGs directly written into the actively doped fiber can be developed without the need for specialty fibers.

6. Conclusion - outlook

The aim of this work was to investigate the inscription of FBGs with femtosecond pulses into different non-photosensitive fibers (e.g. standard telecommunication fibers, rare-earth doped fibers and polarization maintaining fibers). Our approach is based on the non-linear absorption of femtosecond pulses into transparent glasses to induce a permanent refractive index modification into the fiber core. Because of the short coherence length of the pulses, a standard interferometric method is difficult to implement with the required accuracy and a phase mask was preferably used to produce the interference pattern by overlapping a pair of diffracted beams in the phase mask vicinity.

As the refractive index change is induced by the non-linear absorption of femtosecond pulses, high energy densities are required to overcome the threshold for permanent refractive index modification. We have demonstrated that the fiber core can only be reached if the laser beam is focused strongly enough to overcome the fiber curvature. Therefore, we modeled the focusing of the laser beam through the curved fiber surface and found an analytical condition on the Rayleigh length of the focused laser beam. Furthermore, we lowered the requirements on the positioning accuracy by setting the minimum beam waist position to the fiber core. This can be realized for a particular Rayleigh length of the focused beam depending on the fiber cladding diameter. For a standard single mode fiber with a cladding diameter of 125 µm and a 9 µm fiber core, focusing a 2.4 mm laser beam radius with the optimized 40 mm focal length leads to a required position accuracy of 100 µm for the distance between the fiber and the focusing lens. A method allowing the positioning of the focused laser beam into the fiber core was also developed. We demonstrated, for the first time, the monitoring of the luminescence resulting from the non-linear absorption of the defects present in the fiber core as an effective method to position the modifications into the fiber core. This positioning technique is particularly attractive as it allows the effective inscription of long FBGs by monitoring the luminescence for different points along the axis of the optical fiber.

Using the previously described approaches, we demonstrated, for the first time, the inscription of highly reflective 40 mm long FBGs using a phase mask scanning technique. Furthermore, the monitoring of the grating transmission during the FBG inscription allowed the evaluation of the coupling constant for different writing parameters such as pulse energy and writing velocity. Thus, an optimum pulse energy, for which the coupling constant and

the Bragg wavelength vary monolithically with respect to the writing velocity was found. Specific grating designs can be realized by varying the scanning velocity during the FBG inscription or, for uniform gratings, by choosing the appropriate coupling constant and grating length.

The study of the thermal stability of the FBGs written with the phase mask scanning technique revealed a behavior typical for type I FBGs for pulse energies $E \leq 500\,\mu J$. However, the femtosecond written FBGs demonstrated a higher thermal stability than for typical type I UV gratings. For example, a long-term annealing study revealed that 87 % of the refractive index modulation was still remaining after several hours heating at 600°C. The change of the refractive index modulation had however a limited impact on the grating reflectivity itself as the reduction of the refractive index change was compensated by the long grating length used. Therefore, these FBGs can be used as reliable temperature sensors for T < 600°C with very little change in the grating reflectivity.

Furthermore, we demonstrated the first inscription of FBGs in rare-earth doped fibers and polarization maintaining fibers using femtosecond pulses. These FBGs have been successfully implemented, for the first time, in erbium- and ytterbium-doped fiber lasers as resonator mirrors demonstrating that the structural modification had no influence on the laser properties. This opens the possibility for the realization of more robust fiber lasers in which the FBGs are directly written into the rare-earth doped fiber. We also demonstrated that FBGs can be written into panda type PM fibers to avoid polarization mode competition. Thus, more stable and linearly polarized fiber lasers can be implemented. The inscription of FBGs into Large Mode Area (LMA) fibers was also demonstrated, for the first time, using the phase mask scanning technique. Due to the large size of the grating, a good overlap of the refractive index modification with the fiber core (Φ_{core}=20 µm) is reached and a reflection of 90 % could be measured. Those FBGs can be implemented in the realization of monolithic high power fiber lasers.

In this thesis, the inscription of FBGs with ultrashort pulses was demonstrated for different types of non-photosensitive single mode fibers. This work constitutes the basis for further major development in the implementation and design of highly integrated and robust fiber lasers of a new generation, which are not limited by the use of a photosensitive fiber.

Further open fields of research are, for example, the realization of dispersion compensating devices, such as chirped FBGs, directly into the active fiber. The grating profile can thus be adapted to the fiber laser system using an appropriate chirp of the phase mask period. Furthermore, as the refractive index change is located at the laser beam focus, the overlap between the refractive index modification and a particular mode can be controlled. Hence, the inscription of FBGs with femtosecond pulses also opens new possibilities for the realization of

new devices such as the filtering of a particular mode in a slightly multimode fiber. This could allow an effective single mode operation at a particular wavelength in slightly multimode fibers such as Large Mode Area (LMA) fibers for example.

Bibliography

[1] K. O. Hill, Y. Fujii, D. C. Johnson, and B. S. Kawasaki, "Photosensitivity in optical fiber waveguides: Application to reflection filter fabrication," Appl. Phys. Lett. **32**, 647–649 (1978).

[2] S. Nolte, M. Will, J. Burghoff, and A. Tünnermann, "Femtosecond waveguide writing: a new avenue to three-dimensional integrated optics," Appl. Phys. A **77**, 109–111 (2003).

[3] A. Szameit, D. Blömer, J. Burghoff, T. Pertsch, S. Nolte, and A. Tünnermann, "Hexagonal waveguide arrays written with fs-laser pulses," Appl. Phys. B **82**, 507–512 (2006).

[4] J. Burghoff, H. Hartung, S. Nolte, and A. Tünnermann, "Structural properties of femtosecond laser-induced modifications in LiNbO$_3$," Appl. Phys. A **86**, 165–170 (2007).

[5] H. Kogelnik, "Coupled wave theory for thick hologram gratings," The Bell System Technical Journal **48**, 2909–2947 (1969).

[6] B. Saleh and M. Teich, *Fundamentals of photonics* (Wiley, 1991).

[7] W. v. Etten and J. v. d. Plaats, *Fundamentals of optical fiber communications* (New York : Prentice Hall, 1991).

[8] D. Marcuse, *Light transmission optics* (Malabar, Fla. : Krieger, 1989).

[9] T. Erdogan, "Fiber Grating Spectra," J. Lightwave Technol. **15**, 1277–1294 (1997).

[10] M. Born and E. Wolf, *Principles of optics* (New York: Pergamon, 1987). Sec. 8.6.1, eq.(8).

[11] R. Kashyap, *Fiber Bragg gratings* (Academic Press, 1999), Sec. 4.2.

[12] W. Xie, M. Douay, P. Bernage, P. Niay, J. Bayon, and T. Georges, "Second order diffraction efficiency of Bragg gratings written within germanosilicate fibers," Opt. Comm. **101**, 85–91 (1993).

[13] E. Kreyszig, *Advanced Engineering Mathematics*, 5th ed. (Wiley, 1992). P.345.

[14] P. S. J. Russell, J. L. Archambault, and L. Reekie, "Fiber gratings," Phys. World **10**, 4146 (1993).

[15] M. Yamada and K. Sakuda, "Analysis of almost-periodic distributed feedback slab waveguides via a fundamental matrix approach," Appl. Opt. **26**, 3474–3478 (1987).

[16] L. A. Weller-Brophy, "Analysis of waveguide gratings: Application of Rouard's method," J. Opt. Soc. Amer. A **2**, 863–871 (1985).

[17] T. Erdogan, "Cladding-mode resonances in short- and long-period fiber grating filters," J. Opt. Soc. Am. A **14**, 1760–1773 (1997).

[18] K. Hill and G. Meltz, "Fiber Bragg grating technology fundamentals and overview," J. of Lightwave Technol. **15**(8), 1263–1276 (1997).

[19] V. Mizrahi and J. E. Sipe, "Optical Properties of Photosensitive Fiber Phase Gratings," J. of Lightwave Technol. **11**, 1513–1517 (1993).

[20] B. S. Kawasaki, K. O. Hill, D. C. Johnson, and Y. Fujii, "Narrow-band Bragg reflectors in optical fibers," Opt. Lett. **3**, 647–649 (1978).

[21] D. K. W. Lam and B. K. Garside, "Characterization of single-mode optical fiber filters," Appl. Opt. **20**, 440–445 (1981).

[22] G. Meltz, W. W. Morey, and W. H. Glenn, "Formation of Bragg gratings in optical fibers by a transverse holographic method," Opt. Lett. **14**, 823–825 (1989).

[23] M. J. Yuen, "Ultraviolet absorption studies of germanium silicate glasses," Appl. Opt. **21**, 136–140 (1982).

[24] A. Othonos, "Fiber Bragg gratings," Rev. Sci. Instrum. **68**, 4309–4341 (1997).

[25] P. J. Lemaire, R. M. Atkins, V. Mizrahi, and W. A. Reed, "High pressure H_2 loading as a technique for achieving ultrahigh UV photosensitivity and thermal sensitivity in GeO_2 doped optical fibres," Electron. Lett. **29**, 1191 (1993).

[26] R. Atkins, P. Lemaire, T. Erdogan, and V. Mizrahi, "Mechanisms of enhanced UV photosensitivity via hydrogen loading in germanosilicate glasses," Electron. Lett. **29**, 1234–1235 (1993).

[27] B. Bilodeau, F.and Malo, J. Albert, D. C. Johnson, K. O. Hill, Y. Hibino, M. Abe, and M. Kawachi, "Photosensitization of optical fiber and silica-on-silicon/silica waveguides," Opt. Lett. **18**, 953–955 (1993).

[28] D. Williams, B. Ainslie, J. Armitage, R. Kashyap, and R. Campbell, "Enhanced UV photosensitivity in boron codoped germanosilicate fibres," Electron. Lett. **29**, 45 (1993).

[29] M. G. Sceats, G. R. Atkins, and S. B. Poole, "Photolytic index changes in optical fibers," Annu. Rev. Mater. Sci. **23**, 381 (1993).

[30] P. S. Russell, L. J. Poyntz-Wright, and D. P. Hand, "Frequency doubling, absorption, and grating formation in glass fibers: effective defects or defective effects?", in *Fiber Laser Sources and Amplifiers II*, M. J. F. Digonnet, ed., vol. 1373 of *Proc. SPIE*, pp. 126–139 (1991).

[31] R. Atkins, V. Mizrahi, and T. Erdogan, "248 nm induced vacuum UV spectral changes in optical fibre preform cores: support for a colour centre model of photosensitivity," Electron. Lett. **29**, 385 (1993).

[32] M. G. Sceats, G. R. Atkins, and S. B. Poole, "Photo-induced index changes in optical fibers," Annual Rev. Mater. Sci. **23**, 381–410 (1993).

[33] D. P. Hand and P. S. J. Russel, in *Integrated Optics and Optical Conference (IOOC) proceedings*, 21C3-21C4 (Japan, 1992).

[34] P. Fonjallaz, H. Limbergher, R. Salathe, F. Cochet, and B. Leuenberger, "Tension increase correlated to refractive-index change in fibers containing UV-written Bragg gratings," Opt. Lett. **20**, 1346–1348 (1995).

[35] H. Limbergher, P. Fonjallaz, R. Salathe, and F. Cochet, "Compaction- and photoelastic-induced index changes in fiber Bragg gratings," Appl. Phys. Lett. **68**, 3069–3071 (1996).

[36] D. N. Nikogosyan, "Multi-photon high-excitation-energy approach to fibre grating inscription," Meas. Sci. Technol. **18**, R1–R29 (2007).

[37] J. Albert, B. Malo, K. O. Hill, F. Bilodeau, and S. Johnson, D. C. Thériault, "Comparison of one-photon and two-photon effects in the photosensitivity of germanium-doped silica optical fibers exposed to intense Ar-F excimer laser pulses," Appl. Phys. Lett. **67**, 3529–3531 (1995).

[38] H. Patrick, S. L. Gilbert, A. Lidgard, and M. D. Gallagher, "Annealing of Bragg gratings in hydrogen-loaded optical fiber," J. of Applied Physics **78**, 2940–2945 (1995).

[39] S. R. Baker, H. N. Rourke, V. Baker, and D. Goodschild, "Thermal decay of fiber Bragg gratings written in Boron and Germanium codoped silica fiber," J. of Lightwave Technol. **15**, 1470–1477 (1997).

[40] I. Riant and F. Haller, "Study of the photosensitivity at 193 nm and comparison with photosensitivity at 240 nm. Influence of fiber tension: type IIa aging," J. of Lightwave Technol. **15**, 1464–1469 (1997).

[41] W. X. Xie, P. Niay, P. Bernage, M. Douay, J. F. Bayon, T. Georges, and F. Monerie, "Experimental evidence of two types of photorefractive effects occurring during inscription of Bragg gratings within germanosilicate fibers," Opt. Comm. **104**, 185–195 (1993).

[42] L. Dong and W. F. Liu, "Thermal decay of fiber Bragg gratings of positive and negative index changes formed at 193 nm in a boron-codoped germanosilicate fiber," Appl. Opt. **36**, 8222–8226 (1997).

[43] J.-L. Archambault, L. Reekie, and P. S. J. Russell, "100 % reflectivity Bragg reflectors produced in optical fibres by single excimer laser pulses," Electron. Lett. **29**, 453–455 (1993).

[44] M. Douay, W. Xie, T. Taunay, P. Bernage, P. Niay, P. Cordier, B. Poumellec, L. Dong, J. Bayon, H. Poignant, and E. Delevaque, "Densification Involved in the UV-Based Photosensitivity of Silica Glasses and Optical Fibers," J. of Lightwave Technol. **15**(8), 1329–1342 (1997).

[45] J. Albert, M. Fokine, and W. Margulis, "Grating formation in pure silica-core fibers," Opt. Lett. **27**(10), 809–811 (2002).

[46] K. Miura, J. Qiu, H. Inouye, T. Mitsuyu, and K. Hirao, "Photowritten optical waveguides in various glasses with ultrashort pulse laser," Appl. Phys. Lett. **74**, 3329–3331 (1997).

[47] K. Florea and K. A. Winick, "Fabrication and Characterization of Photonic Devices Directly Written in Glass Using Femtosecond Laser Pulses," J. of Lightwave Technol. **21**, 246–253 (2003).

[48] J. Thomas, A. Ancona, M. Heinrich, J. Burghoff, S. Nolte, and A. Tünnermann, "Femtosecond laser-written quasi-phase-matched waveguides in lithium niobate," Appl. Phys. Lett. **91**, 151108 (2007).

[49] G. Della Valle, R. Osellame, and P. Laporta, "Micromachining of photonic devices by femtosecond laser pulses," Journal of Optics A: Pure and Applied Optics **11**(1), 013001 (18pp) (2009).

[50] M. Will, S. Nolte, B. N. Chichkov, and A. Tünnermann, "Optical Properties of Waveguides Fabricated in Fused Silica by Femtosecond Laser Pulses," Appl. Opt. **41**(21), 4360–4364 (2002).

[51] R. R. Gattass, L. R. Cerami, and E. Mazur, "Micromachining of bulk glass with bursts of femtosecond laser pulses at variable repetition rates," Opt. Express **14**(12), 5279–5284 (2006).

[52] S. Eaton, H. Zhang, P. Herman, F. Yoshino, L. Shah, J. Bovatsek, and A. Arai, "Heat accumulation effects in femtosecond laser-written waveguides with variable repetition rate," Opt. Express **13**(12), 4708–4716 (2005).

[53] B. C. Stuart, M. D. Feit, S. Herman, A. M. Rubenchik, B. W. Shore, and M. D. Perry, "Nanosecond-to-femtosecond laser-induced breakdown in dielectrics," Phys. Rev. B **53**, 1749–1761 (1996).

[54] C. B. Schaffer, A. Brodeur, and E. Mazur, "Laser-induced breakdown and damage in bulk transparent materials induced by tightly focused femtosecond laser pulses," Meas. Sci. Technol. **12**, 1784–1794 (2001).

[55] A. P. Joglekar, H.-H. Liu, E. Meyhöfer, G. Mourou, and A. J. Hunt, "Optics at critical intensity: Applications to nanomorphing," Proc. Natl. Acad. Sci. USA **101**, 5856–5861 (2004).

[56] J. Chan, T. Huser, S. Risbud, and D. Krol, "Modification of the fused silica glass network associated with waveguide fabrication using femtosecond laser pulses," Appl. Phys. A **76**, 367–372 (2003).

[57] J. Chan, T. Huser, S. Risbud, J. Hayden, and D. Krol, "Waveguide fabrication in phosphate glasses using femtosecond laser pulses," Appl. Phys. Lett. **82**, 2371–2373 (2003).

[58] A. M. Streltsov and N. F. Borrelli, "Study of femtosecond-laser-written waveguides in glasses," J. Opt. Soc. Am. B **19**(10), 2496–2504 (2002).

[59] E. N. Glezer and E. Mazur, "Ultrafast-laser driven micro-explosions in transparent materials," Appl. Phys. Lett. **71**, 882–884 (1997).

[60] C. B. Schaffer, A. O. Jamison, and E. Mazur, "Morphology of femtosecond laser-induced structural changes in bulk transparent materials," Appl. Phys. Lett. **84**, 1441–1443 (2004).

[61] L. Sudrie, M. Franco, B. Prade, and A. Mysyrowicz, "Study of damage in fused silica induced by ultra-short IR laser pulses," Opt. Comm. **191**, 333–339 (2001).

[62] Y. Shimotsuma, P. G. Kazansky, J. Qiu, and K. Hirao, "Self-Organized Nanogratings in Glass Irradiated by Ultrashort Light Pulses," Phys. Rev. Lett. **91**, 2474,405 (2003).

[63] A. Martinez, M. Dubov, I. Khrushchev, and I. Bennion, "Direct writing of fibre Bragg gratings by femtosecond laser," Electron. Lett. **40**(19), 1170–1172 (2004).

[64] E. Wikszak, J. Burghoff, M. Will, S. Nolte, A. Tünnermann, and T. Gabler, "Recording of fiber Bragg gratings with femtosecond pulses using a "point by point" technique," in *Conference on Lasers and Electro-Optics/International Quantum Electronics Conference and Photonic Applications Systems Technologies*, CThM7 (Optical Society of America, 2004).

[65] G. Cerullo, R. Osellame, S. Taccheo, M. Marangoni, D. Polli, R. Ramponi, P. Laporta, and S. De Silvestri, "Femtosecond micromachining of symmetric waveguides at 1.5 µm by astigmatic beam focusing," Opt. Lett. **27**, 1938–1940 (2002).

[66] J. D. Mills, C. W. J. Hillman, B. H. Blott, and W. S. Brocklesby, "Imaging of free-space interference patterns used to manufacture fiber Bragg gratings," Appl. Opt. **39**, 6128–6135 (2000).

[67] C. W. Smelser, D. Grobnic, and S. J. Mihailov, "Generation of pure two-beam interference grating structures in an optical fiber with a femtosecond infrared source and a phase mask," Opt. Lett. **29**(15), 1730–1732 (2004).

[68] J. Thomas, E. Wikszak, T. Clausnitzer, U. Fuchs, U. Zeitner, S. Nolte, and A. Tünnermann, "Inscription of fiber Bragg gratings with femtosecond pulses using a phase mask scanning technique," Appl. Phys. A **86**(2), 153–157 (2007).

[69] B. Saleh and M. Teich, *Fundamentals of photonics* (Wiley, 1991). Sec.3.2.D, p.99-100.

[70] B. Saleh and M. Teich, *Fundamentals of photonics* (Wiley, 1991). Sec.1.4.B, p.29.

[71] G. D. Marshall, M. Ams, and M. J. Withford, "Direct laser written waveguide-Bragg gratings in bulk fused silica," Opt. Lett. **31**, 2690–2691 (2006).

[72] N. Jovanovic, A. Fuerbach, G. D. Marshall, M. J. Withford, and S. D. Jackson, "Stable high-power continuous-wave Yb^{3+}-doped silica fiber laser utilizing a point-by-point inscribed fiber Bragg grating," Opt. Lett. **32**, 1486–1488 (2007).

[73] D. Strickland and G. Mourou, "Compression of amplified chirped optical pulses," Opt. Comm. **56**, 219 (1985).

[74] F. Dürr, H. G. Limberger, R. P. Salathé, F. Hindle, M. Douay, E. Fertein, and C. Przygodzki, "Tomographic measurement of femtosecond-laser induced stress changes in optical fibers," Appl. Phys. Lett. **84**(24), 4983–4985 (2004).

[75] M. Ams, G. Marshall, P. Dekker, M. Dubov, V. Mezentsev, I. Bennion, and M. Withford, "Investigation of Ultrafast Laser–Photonic Material Interactions: Challenges for Directly Written Glass Photonics," Selected Topics in Quantum Electronics, IEEE Journal of **14**(5), 1370–1381 (2008).

[76] D. Grobnic, C. Smelser, S. Mihailov, R. Walker, and P. Lu, "Fiber Bragg gratings with suppressed cladding modes made in SMF-28 with a femtosecond IR laser and a phase mask," IEEE Photon. Technol. Lett. **16**(8), 1864–1866 (2004).

[77] L. Dong, G. Qi, M. Marro, V. Bhatia, L. Hepburn, M. Swan, A. Collier, and D. Weidman, "Suppression of cladding mode coupling loss in fiber Bragg gratings," J of Lightwave Technol. **18**(11), 1583–1590 (2000).

[78] J. Albert, S. Theriault, F. Bilodeau, D. Johnson, K. Hill, P. Sixt, and M. Rooks, "Minimization of phase errors in long fiber Bragg grating phase masks made using electron beam lithography," IEEE Photon. Technol. Lett. **8**(10), 1334–1336 (1996).

[79] C. W. Smelser, S. J. Mihailov, and D. Grobnic, "Impact of index change saturation on the growth behavior of higher-order type I ultrafast induced fiber Bragg gratings," J. Opt. Soc. Am. B **25**(5), 877–883 (2008).

[80] C. W. Smelser, S. J. Mihailov, and D. Grobnic, "Formation of Type I-IR and Type II-IR gratings with an ultrafast IR laser and a phase mask," Opt. Expr. **13**(14), 5377–5386 (2005).

[81] B. Malo, J. Albert, K. Hill, F. Bilodeau, D. Johnson, and S. Theriault, "Enhanced photosensitivity in lightly doped standard telecommunication fibre exposed to high fluence ArF excimer laser light," Electron. Lett. **31**(11), 879–880 (1995).

[82] D. Blömer, A. Szameit, F. Dreisow, T. Schreiber, S. Nolte, and A. Tünnermann, "Nonlinear refractive index of fs-laser-written waveguides in fused silica," Opt. Express **14**(6), 2151–2157 (2006).

[83] A. Martinez, I. Khrushchev, and I. Bennion, "Thermal properties of fibre Bragg gratings inscribed point-by-point by infrared femtosecond laser," Electron. Lett. **41**(4), 176–178 (2005).

[84] C. W. Smelser, D. Grobnic, P. Lu, and S. J. Mihailov, "High temperature stable Type I IR ultrafast induced FBGs," in *34th European Conference on Optical Communications*, We.3.B.2 (2008).

[85] Y. Li, C. R. Liao, D. N. Wang, T. Sun, and K. T. V. Grattan, "Study of spectral and annealing properties offiber Bragg gratings written in H_2-free and H_2-loaded fibers by use of femtosecond laser pulses," Opt. Express **16**(26), 21,239–21,247 (2008).

[86] O. V. Mazurin, M. V. Streltsina, and T. P. Shvaiko-Shvaikovskaya, *Handbook of Glass Data Part A* (Elsevier, 1983).

[87] H. Takahashi, H. Toba, and Y. Inoue, "Multiwavelength ring laser composed of EDFAs and an arrayed-waveguide wavelength multiplexer," Electron. Lett. **30**(1), 44–45 (1994).

[88] M. Young, U. Koren, B. Miller, M. Newkirk, M. Chien, M. Zirngibl, C. Dragone, B. Tell, H. Presby, and G. Raybon, "A 16×1 wavelength division multiplexer with integrated distributed Bragg reflector lasers and electroabsorption modulators," IEEE Photon. Technol. Lett. **5**(8), 908–910 (1993).

[89] J. Chow, G. Town, B. Eggleton, M. Ibsen, K. Sugden, and I. Bennion, "Multiwavelength generation in an erbium-doped fiber laser using in-fiber comb filters," IEEE Photon. Technol. Lett. **8**(1), 60–62 (1996).

[90] A. Bellemare, M. Karasek, M. Rochette, S. LRochelle, and M. Tetu, "Room temperature multifrequency erbium-doped fiber lasers anchored on the ITU frequency grid," J. of Lightwave Technol. **18**(6), 825–831 (2000).

[91] Z. Chun-Liu, Y. Xiufenga, L. Chaoa, N. J. Honga, G. Xina, P. R. Chaudhuria, and D. Xinyongb, "Switchable multi-wavelength erbium-doped fiber lasers by using cascaded fiber Bragg gratings written in high birefringence fiber," Opt. Comm. **230**, 313–317 (2004).

[92] J. Sousa and O. Okhotnikov, "Multiple wavelength Q-switched fiber laser," IEEE Photon. Technol. Lett. **11**(9), 1117–1119 (1999).

[93] N. Park and P. Wysocki, "24-line multiwavelength operation of erbium-doped fiber-ring laser," IEEE Photon. Technol. Lett. **8**(11), 1459–1461 (1996).

[94] X. Dong, S. Li, K. Chiang, M. Ng, and B. Chu, "Multiwavelength erbium-doped fibre laser based on a high-birefringence fibre loop mirror," Electron. Lett. **36**(19), 1609–1610 (2000).

[95] J. Zyskind, V. Mizrahi, D. DiGiovanni, and J. Sulhoff, "Short single frequency erbium-doped fibre laser," Electron. Lett. **28**(15), 1385–1387 (1992).

[96] M. Sejka, P. Varming, J. Hubner, and M. Kristensen, "Distributed feedback Er^{3+}-doped fibre laser," Electron. Lett. **31**(17), 1445–1446 (1995).

[97] W. Loh and R. Laming, "1.55 μm phase-shifted distributed feedback fibre laser," Electron. Lett. **31**(17), 1440–1442 (1995).

[98] L. Dong, W. H. Loh, J. E. Caplen, J. D. Minelly, K. Hsu, and L. Reekie, "Efficient single-frequency fiber lasers with novel photosensitive Er/Yb optical fibers," Opt. Lett. **22**(10), 694–696 (1997).

[99] J. Kringlebotn, J.-L. Archambault, L. Reekie, J. Townsend, G. Vienne, and D. Payne, "Highly-efficient, low-noise grating-feedback Er^{3+} : Yb^{3+} codoped fibre laser," Electron. Lett. **30**(12), 972–973 (1994).

[100] G. Bonfrate, F. Vaninetti, and F. Negrisolo, "Single-frequency MOPA Er^{3+} DBR fiber laser for WDM digital telecommunication systems," IEEE Photon. Technol. Lett. **10**(8), 1109–1111 (1998).

[101] E. Wikszak, J. Thomas, J. Burghoff, B. Ortaç, B. Limpert, S. Nolte, U. Fuchs, and A. Tünnermann, "Erbium Fiber Laser based on intracore femtosecond written Fiber Bragg Grating," Opt. Lett. **31**(16), 2390 (2006).

[102] J. Limpert, A. Liem, H. Zellmer, and A. Tunnermann, "500 W continuous-wave fibre laser with excellent beam quality," Electron. Lett. **39**(8), 645–647 (2003).

[103] N. G. R. Broderick, H. L. Offerhaus, D. J. Richardson, R. A. Sammut, J. Caplen, and L. Dong, "Large Mode Area Fibers for High Power Applications," Opt. Fiber Technol. **5**(2), 185 – 196 (1999).

[104] J. Knight, T. Birks, R. Cregan, P. Russell, and P. de Sandro, "Large mode area photonic crystal fibre," Electron. Lett. **34**(13), 1347–1348 (1998).

[105] J. Noda, K. Okamoto, and Y. Sasaki, "Polarization-maintaining fibers and their applications," J. Lightwave Technol. **4**(8), 1071–1089 (1986).

[106] Z. Liu, Y. Liu, Y. Du, S. Yuang, and X. Dong, "Switchable triple-wavelength erbium-doped fiber laser using a single fiber Bragg grating in polarization-maintaining fiber," Opt. Comm. **279**, 168–172 (2007).

[107] A. Shirakawa, M. Kamijo, J. Ota, K. I. Ueda, K. Mizuuchi, H. Furuya, and K. Yamamoto, "Linearly-polarized Yb-doped fiber laser in all-fiber configuration," in *Conference on Lasers and Electro-Optics/International Quantum Electronics Conference and Photonic Applications Systems Technologies*, CMC5 (Optical Society of America, 2007).

[108] A. Martinez, M. Dubov, I. Y. Khrushchev, and I. Bennion, "Photoinduced Modifications in Fiber Gratings Inscribed Directly by Infrared Femtosecond Irradiation," IEEE Photon. Technol. Lett. **18**(21), 2266–2268 (2006).

Zusammenfassung

Die Entdeckung des Faser-Bragg-Gitters (FBG) hat die Herstellung von faserintegrierten schmalbandigen Reflektoren und Transmissionsfiltern ermöglicht. Dadurch konnten z. B. kompakte Wellenlängenmultiplexer und schmalbandige Faserlaser mit geringen Verlusten hergestellt werden, die als Hauptkomponenten der *Dense Wavelength Division Multiplexing* (DWDM) Technik benutzt werden. Da die FBG auch die Eigenschaft haben, dass die Braggwellenlänge sich durch Änderungen der Temperatur und der Dehnung verschiebt, werden sie in kompakten Fasersensorensystemen benutzt.

Ein FBG besteht aus einer periodischen Brechzahlveränderung, die durch die Absorption eines UV-Interferenzmusters im Kern einer photoempfindlichen Faser erzeugt wird. Da die UV-Absorption in handelsüblichen Fasern sehr gering ist, werden im Faserkern Defekte erzeugt, die eine zusätzliche UV-Absorption hervorrufen. Dafür wird der Faserkern typischerweise mit Germanium, aber auch mit anderen Ionen dotiert. Eine andere Möglichkeit, neue Defekte in handelsüblichen Germanosilikatfasern zu erzeugen, ohne die chemische Zusammensetzung der Faser ändern zu müssen, besteht in einer Wasserstoffbeladung der Faser unter hohem Druck. Die Anwendung solcher Techniken ist jedoch schwierig auf eine mit seltenen Erden dotierte Faser übertragbar.

Aus diesen Gründen wurde die Herstellung von FBG in Fasern mit unterschiedlichen chemischen Zusammensetzungen ohne Vor- oder Nachbehandlung untersucht. Eine Lösungsmöglichkeit bietet die nichtlineare Absorption von ultrakurzen Pulsen, die eine permanente Brechzahlveränderung in einen transparenten Material hervorrufen kann. Dafür werden hohe Energiedichten benötigt und die Brechzahlmodifikation findet auschließlich im Laserfokus statt, was die einfache Herstellung von dreidimensionalen Wellenleiterstrukturen ermöglicht.

Die Untersuchungen wurden zunächst an handelsübligen Monomodefasern aber auch an Fasern, die mit seltenen Erden dotiert oder polarisationserhaltend sind, durchgeführt, was die Herstellung von kompakten, stabilen und robusten Faserlasern ermöglicht.

Mittels einer klassischen interferometrischen Methode ist es, aufgrund der kurzen Kohärenzlänge der Pulse, schwierig, die beiden Strahlen mit der benötigten Genauigkeit zu überlagern. Deswegen entsteht das Interferenzmuster aus der Überlagerung der Beugungsordnungen einer Phasenmaske. Durch die Benutzung von ultrakurzen Pulsen ist es jedoch möglich, ein reines Zweistrahl-Interferenzmuster zu erzeugen. Wenn der Abstand zwischen Phasenmaske

und Faser ausreichend ist, erreichen einige der Beugungsordnungen den Faserkern mit einem zeitlichen Abstand größer als die Kohärenzzeit und können daher nicht zur Interferenz beitragen. Der benötigte Laufzeitunterschied kann durch ein geometrisches Modell berechnet und der entsprechend notwendige Abstand zwischen Phasenmaske und Faser, bei dem eine reine Zweistrahl-Interferenz entsteht, bestimmt werden.

Da die Brechzahlmodifikationen im Fokus des Laserstrahles entstehen, beeinflussen die Fokussierungsbedingungen und die Faserkrümmung die Fokussierung des Laserstrahles in den Faserkern. Durch die Modellierung der gekrümmten Faseroberfläche wurde eine analytische Bedingung, die die Fokussierung des Laserstrahles in dem Faserkern ermöglicht, gefunden. Für eine bestimmte Rayleighlänge, die abhängig vom Fasermanteldurchmesser ist, können sogar die Anforderungen an die Positionierungsgenauigkeit erniedrigt werden. Die Positionierung der Modifikationen in den Faserkern kann mit Hilfe der Lumineszenz, die durch die nichtlineare Absorption der Defekte, die sich im Faserkern befinden, erreicht werden. Damit der Laserstrahl in den Kern fokussiert wird, wurde der Abstand zwischen Faser und Linse so gewählt, dass diese Lumineszenz maximal ist. Diese Methode ermöglicht auch die Herstellung von langen FBG mit guter Qualität. Durch eine Translation der Faser und der Phasenmaske bezüglich des Laserstrahls wurden zum ersten Mal 40 mm lange effiziente FBG geschrieben. Die Länge der eingeschriebenen Gitter wurde dabei nur durch die Länge der benutzten Phasenmaske limitiert.

Die Eigenschaften der eingeschriebenen FBG wurden zunächst in konventionellen Monomodefasern bei 1.55 µm ausgewertet. Es wurde durch die Vermessung der Temperaturbeständigkeit gezeigt, dass die Gitter eine Typ I Brechzahlveränderung aufweisen. Dennoch ist die Temperaturstabilität des Gitters höher als bei UV geschriebenen FBG und erlaubt deren Nutzung als Hochtemperatursensor.

Die direkte Einschreibung von FBG mit femtosekunden Pulsen in Fasern, die mit selten Erden dotiert sind, wurde auch erstmalig demonstriert, wodurch diese FBG als hochreflektierende Resonatorspiegel in einem Faserlaseraufbau ohne Spleißen integriert werden. Dadurch ist die Realisierung verschiedener kompakter und robuster Faserlaser möglich.

Die Einschreibung von FBG in polarisationserhaltende Fasern vom Panda-Typ wurde ebenfalls erstmalig mit Femtosekundenpulsen demonstriert. Da die Polarisation in der Faser erhalten bleibt, können sie in einem komplexeren Aufbau wie z.B in einem linear polarisierten Faserlaser, benutzt werden.

Wir haben die Untersuchungen auf den Fall von Fasern mit größeren Durchmessern erweitert und gezeigt, dass ein FBG mit einer Reflektivität von 90 % in eine Faser mit einem Kerndurchmesser von 20 µm geschrieben werden kann. Dadurch wird die Herstellung von monolithischen Faserlasern ermöglicht.

In dieser Arbeit wurde ebenfalls gezeigt, dass die Einschreibung von FBG in Fasern mit verschiedenen Zusammensetzungen und Geometrien (z.B Monomode oder LMA Fasern) möglich ist. Dadurch kann die kostenintensive Entwicklung von photoempfindlichen Fasern vermieden und die FBG mit einem universalen Verfahren hergestellt werden.

Die vorgelegte Arbeit bildet die Basis für die weitere Entwicklung von kompakteren und robusteren Faserlasern mit höheren Leistungen. Da die Brechzahlveränderung durch die Laserfokusposition frei gewählt werden kann, entstehen auch neue Anwendungen, wie z.B. die Filterung von bestimmten Moden durch den gezielten Überlapp zwischen Moden und Gitter. Dies würde die einfache und robuste Realisierung von monomodigen Faserlasern mit leicht multimodigen LMA-Fasern vereinfachen.

List of own publications

Peer Reviewed Journals

[Wik06]   E. Wikszak, J. Thomas, J. Burghoff, B. Ortaç, J. Limpert, S. Nolte, U. Fuchs, and A. Tünnermann, "Erbium fiber laser based on intracore femtosecond-written fiber Bragg grating," Opt. Lett. **31**(16), 2390–2392 (2006).

[Wik07]   E. Wikszak, J. Thomas, S. Klingebiel, B. Ortaç, J. Limpert, S. Nolte, and A. Tünnermann, "Linearly polarized ytterbium fiber laser based on intracore femtosecond-written fiber Bragg gratings," Opt. Lett. **32**(18), 2756–2758 (2007).

[Th07]   J. Thomas, E. Wikszak, T. Clausnitzer, U. Fuchs, U. Zeitner, S. Nolte, and A. Tünnermann, "Inscription of fiber Bragg gratings with femtosecond pulses using a phase mask scanning technique," Appl. Phys. A **2**(86), 153–157 (2007).

[Th08]   J. Thomas, C. Voigtländer, D. Schimpf, F. Stutzki, E. Wikszak, J. Limpert, S. Nolte, and A. Tünnermann, "Continuously chirped fiber Bragg gratings by femtosecond laser structuring," Opt. Lett. **33**(14), 1560–1562 (2008).

[Vo08]   C. Voigtländer, J. Thomas, E. Wikszak, P. Dannberg, S. Nolte, and A. Tünnermann, "Chirped fiber Bragg gratings written with ultrashort pulses and a tunable phase mask," Opt. Lett. (submitted).

Conference contributions

[Cleo04] E. Wikszak, J. Burghoff, M. Will, S. Nolte, A. Tünnermann, and T. Gabler, "Recording of fiber Bragg gratings with femtosecond pulses using a "point by point" technique," in *Conference on Lasers and Electro-Optics/International Quantum Electronics Conference and Photonic Applications Systems Technologies*, CThM7 (Optical Society of America, 2004).

[Domo04]   S. Nolte, M. Will, J. Burghoff, E. Wikszak, and A. Tünnermann, "3-D microstructuring using ultrafast lasers - a new approach for integrated optics," in *Diffractive Optics and Micro-Optics*, DWA2 (Optical Society of America, 2004).

[Isnog04]   S. Nolte, M. Will, J. Burghoff, E. Wikszak, and A. Tünnermann, "Direct writing of photonic devices inside glasses and crystals by femtosecond laser pulses,"in *Glass & Optical Materials Division Fall 2004 Meeting / XIVth International Symposium on Non-Oxide Glasses (ISNOG)* (American Ceramic Society, 2004).

[Cleo06]   E. Wikszak, J. Thomas, B. Ortaç, J. Limpert, S. Nolte, and A. Tünnermann, "Femtosecond Written Fiber Bragg Grating in Non-Photosensitive Rare-Earth-Doped Fiber," in *Conference on Lasers and Electro-Optics/Quantum Electronics and Laser Science Conference and Photonic Applications Systems Technologies*, CTuY3 (Optical Society of America, 2006).

[Dpg06]   J. Thomas, E. Wikszak, B. Ortaç, J. Limpert, S. Nolte, A. Tünnermann, and T. Gabler, "Femtosekundenlaser-geschriebene Faser-Bragg-Gitter in nicht-photoempfindlichen Fasern," in *DPG Frühjahrstagung*, Q54–5 (Deutsche Physikalische Gesellschaft, 2006).

[Spie06]   E. Wikszak, J. Thomas, S. Nolte, and A. Tünnermann, "Inscribing Fiber Bragg Gratings using IR-fs pulses and a phase-mask scanning technique : potential and applications," in *Proceedings of SPIE*, vol. 6460, pp. 64600Z.1–64600Z.8 (Society of Photo-Optical Instrumentation Engineers, 2006).

[Cleo07]   J. Thomas, E. Wikszak, C. Voigtländer, S. Nolte, and A. Tünnermann, "Femtosecond written fiber gratings in PM and LMA fibers," in *CLEO/Europe and IQEC 2007 Conference Digest*, CJ6–1 (Optical Society of America, 2007).

[Spie09]   C. Voigtländer, J. U. Thomas, E. Wikszak, S. Nolte, and A. Tünnermann, "Femtosecond laser written chirped fiber Bragg gratings," in *Proceedings of SPIE*, vol. 7203, 7203–18 (Society of Photo-Optical Instrumentation Engineers, 2009).

Acknowledgments

I would like to thank all the people that contributed, in one way or the other, to the success of this thesis and more particularly

Professor Andreas Tünnermann, director of the Institute of Applied Physics, who allowed me to make my PhD thesis in his institute and provided the exceptional research possibilities and opportunities,

Professor Stefan Nolte, head of the ultrafast optics group and supervisor, for his expertise and advice,

Dr. Alexander Szameit who was always of good advice and was able to cheer me up when I needed support. I would also like to thank Jens Thomas and Christian Voigtländer, my office "mates" for the interesting and emulating discussions as well as for their relaxed manner. Now that I have finished, the office will not have to be so quiet any more...

Felix Dreisow, Matthias Heinrich, Dr. Jonas Burghoff, Dr. Antonio Ancona from the University of Bari in Italy, Dr. Katja Rademaker and all the people from the ultrafast optics group who contributed to the excellent work climate as well as for their helpful discussions and patience,

Thomas Kämpfe and Holger Hartung for being good friends and collegues,

Dr Bülend Ortac, Marco Plötner, Dr Jens Limpert from the fiber laser group for their expertise and advice concerning the fiber laser experiments. Now you will not have to wonder where the splicing machine disappeared...

Dr. Tina Clausnitzer, Dr. Ernst-Bernhard Kley and all the persons from the microoptics group involved in the realization of the phase masks.

Ulrike Fuchs und Dr. Uwe Zeitner for the ZEEMAX simulations.

Nemanja Jovanovitch from the MacQuarie University in Sydney for his wise advice during the relecture and correction of my thesis

At this place I would also like to thank all the friends I had the pleasure to make during my stay in Jena (and more particularly the french "Stammtisch" and the "Festival de Colores" association members) and helped me feeling at home,

and last but not least, my parents who always believed in me and are always proud of me.

ehrenwörtliche Erklärung

Ich erkläre hiermit ehrenwörtlich, dass ich die vorliegende Arbeit selbstständig, ohne unzulässige Hilfe Dritter und ohne Benutzung anderer als der angegebenen Hilfsmittel und Literatur angefertigt habe. Die aus anderen Quellen direkt oder indirekt übernommenen Daten und Konzepte sind unter Angabe der Quellen gekennzeichnet.

Weitere Personen waren an der inhaltlich-materiellen Erstellung der vorliegenden Arbeit nicht beteiligt. Insbesondere habe ich hierfür nicht die entgeltliche Hilfe von Vermittlungs- bzw. Beratungsdiensten (Promotionsberater oder andere Personen) in Anspruch genommen. Niemand hat von mir unmittelbar oder mittelbar geldwerte Leistungen für Arbeiten erhalten, die im Zusammenhang mit dem Inhalt der vorgelegten Dissertation stehen.

Die Arbeit wurde bisher weder im In- noch im Ausland in gleicher oder ähnlicher Form einer anderen Prüfungsbehörde vorgelegt.

Teile dieser Arbeit wurden aus Prioritätsgründen bereits veröffentlicht (oder wurden zur Veröffentlichung eingereicht).

Die geltende Promotionsordnung der Physikalisch-Astronomischen Fakultät ist mir bekannt. Ich versichere ehrenwörtlich, dass ich nach bestem Wissen die reine Wahrheit gesagt und nichts verschwiegen habe.

Jena, den 23.06.09

Lebenslauf

Elodie WIKSZAK

geboren am 12.06.1980 in Roubaix (Frankreich)

1986 - 1998	Schulbesuch in Tourcoing (Frankreich)
Juni 1998	Abitur mit Physik-Chemie als Vertiefungsfach
1998 - 2000	Vorbereitungsklassen zur Eingangsprüfung zur Ingenieurstudium in eine „Grande Ecole" (entspricht Vordiplom)
Sept. 2000 - Sept. 2003	Studium der Physik an der Ecole Nationale Supérieure de Physique de Marseille (ENSPM, heute Centrale Marseille)
Juli 2002 - Nov. 2002	Praktikum bei Thales Research and Technology in Orsay, Frankreich
März 2003 - Sept. 2003	Diplomarbeit am Institut für Angewandte Physik der FSU Jena im Kooperation mit Jenoptik LOS GmbH, Jena
Sept. 2003	Abschluss mit dem „Diplôme d'ingénieur de l'ENSPM" (enspricht Master of Science)
Okt. 2003 -	Doktorandin am Institut für Angewandte Physik

Jena, den 23.06.2009